UNIVERSITÀ DEGLI STUDI DI PADOVA

Dipartimento di Fisica e Astronomia "Galileo Galilei"

Master Degree in Astrophysics and Cosmology

Final dissertation

Binaries among multiple populations in the globular cluster 47 Tucanae

Thesis supervisor:
Prof. Antonino Milone
Thesis co-supervisor:
Fabrizio Muratore

Candidate:
Mara Bernizzoni

Academic Year 2023/2024

To my family:
I am infinitely grateful for your love and support.

Abstract

Nearly all globular clusters (GCs) host multiple stellar populations composed of stars with different helium and light-element abundances. These comprise first-population stars, which share the same chemical composition as halo-field stars with similar [Fe/H], and the second populations, which are composed of stars with enhanced helium and nitrogen abundances and depleted content of oxygen and carbon. Each stellar population delineates distinct sequences in certain photometric diagrams, which can disentangle stars with different chemical compositions at different evolutionary stages. Nowadays, one of the most intriguing open questions regarding GCs pertains to the formation and evolution of their multiple populations.

Recent works based on N-body simulations of GCs show that the fractions and characteristics of binary stars can serve as dynamic indicators of the formation period of multiple-population GCs and their subsequent dynamical evolution. Nevertheless, the incidence of binaries among multiple populations is still poorly studied. Moreover, the few available observational studies are focused on bright stars of a few GCs alone.

In this master thesis, I used deep images of the GC 47 Tucanae collected with the Hubble Space Telescope (HST) to investigate, for the first time, the incidence of binaries among multiple populations of M-dwarfs. To reach this objective, I follow a new approach, which is based on observations of binaries in the F606W, F814W, F110W, and F160W filters of HST and grids of simulated binaries.

I find that in the analyzed field of view, where the first population comprises $\sim$40% of the total number of stars, the majority (87$\pm$13%) of the studied binaries are composed of first population stars. These findings are consistent with the scenarios where the second-population stars form in the cluster center, arranging in very-dense and compact stellar groups embedded in a more extended first-population system.

Contents

Chapter 1

Multiple stellar populations in Globular Clusters

Globular Clusters (GCs) are among the most puzzling and ancient stellar objects in the Universe. These are large spheroidal agglomerates of stars, largely used in the field of Galactic archaeology, playing a key role in the investigation of the history of the Primordial Universe. In fact, they are believed to have formed mostly at high redshift ($z \gtrsim 3$) (Dotter et al., 2010), corresponding to past epochs at which the Galaxy is supposed to have been not completely formed yet. According to this interpretation, GCs played presumably a fundamental role in the assembly of the Milky Way, in addition to their possible involvement in the re-ionization of the Universe. However, they exhibit peculiarities and complexities that, over the last decades, posed a major challenge for astronomers. Traditionally, they were considered as prototypes of a simple stellar population (SSP), namely a population of coeval stars formed in a single burst of star formation from the same molecular cloud, hence characterized by same metallicity, chemical composition and age (Renzini & Buzzoni, 1986).

Until the development of modern techniques of observation and detection such as space-based facilities and advanced computer facilities and codes, all the sequences of stars of GCs were thought to be consistent with a single isochrone, a track for an SSP produced thanks to our knowledge of stellar evolution. One appropriate example is NGC 6397, appearing as one of the closest GCs, whose Color Magnitude Diagram (CMD) is presented in Figure 1.1. However, this traditional view is now outdated. Indeed, using modern techniques, the majority of GCs show CMDs similar to Figure 1.2 (left panel), where there are distinct sequences of stars. This anomaly refers to the presence of multiple populations (MPs), exhibiting different chemical composition: the synergy between low-resolution spectroscopy and high-precision photometry confirmed the phenomenon. Therefore, it became clear that GCs are much more complex than expected. Nowadays, it is accepted that the chemical abundance spread spotted within most GCs is the manifestation of multiple stellar populations.

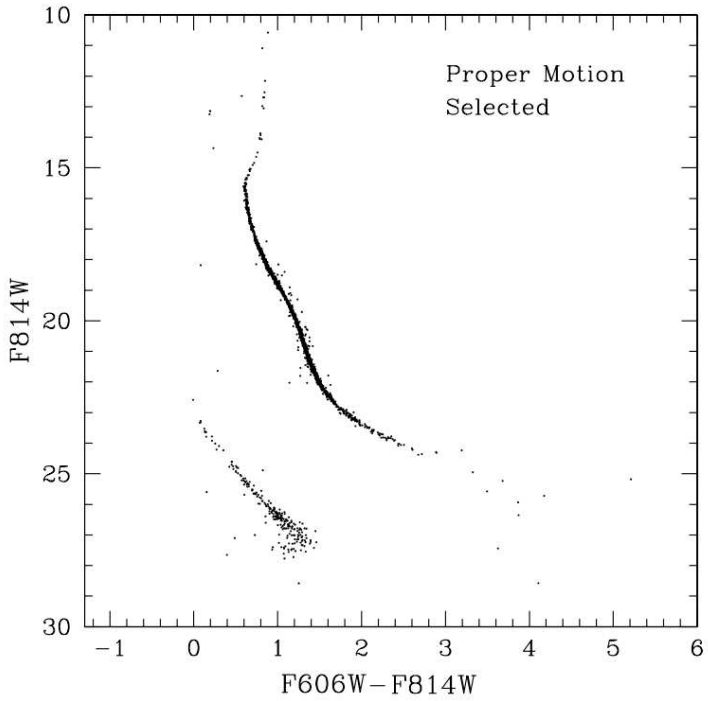

Figure 1.1: $m_{\rm F814W}$ vs $m_{\rm F606W} - m_{\rm F814W}$ CMD of NGC 6397, from Richer et al. (2008). This cluster exhibits a narrow main sequence which is compatible with the stellar track provided by one isochrone. The GC's main sequence and the white dwarf cooling sequence are shown, respectively, on the right and on the left.

1.1 Properties of multiple populations

The chemical composition of GCs' stars is not homogeneous regarding the amount of elements typically associated to the hot H-burning, as they reveal different light-element content (C, N, O, Al, as well as Mg, Si and even K) and traces of peculiar helium content. Such star-by-star fluctuations may be indicative of some additional process occurring inside some stars and driving their evolution. MPs are detected as distinct sequences in the CMDs, which can be traced through the whole stellar evolution, from the bottom of the main sequence (MS) (Milone et al., 2012d,e), up to the tip of the red giant branch (RGB), and along the horizontal branch (HB) (Dondoglio et al., 2021), the asymptotic giant branch (AGB) (Lagioia et al., 2021), together with the white dwarf cooling sequence (WDCS).

A crucial factor to establish the MPs phenomenon was the enhancement in the definition and use of CMDs: there are specific combinations of colors that are capable of underlying the sequences' splitting better than others. It is remarkable the impact that the Hubble Space Telescope (HST) is having on this field, offering unprecedented precision and accuracy for the exploration of the MPs. Mostly, the goal is to maximize the separation of distinct stellar populations, highlighting differences in their chemical composition. Spreads and splits among stellar populations of a cluster depend on the color and on the evolutionary phase addressed. In the following items are summarized the most exploited and powerful photometric tools.

⋆ **Wide-band UV photometry.** There is evidence for large color spreads among RGB stars, on CMDs including near-UV filters, for color combinations that are extremely sensitive to light elements abundances (e.g. C, Na, O). Below 4000 Å, the wavelength range allows to observe for example NH and CN absorptions, to which the U filter is sensitive. Multiple RGB sequences are detected in the U vs U-B CMD, spotting changes in the abundance pattern. Indeed, Marino et al. (2008) proved that wide-band ground-based photometry can be used to efficiently disentangle MPs, studying the nearby cluster M 4.

⋆ **Wide color baseline.** Theoretically speaking, stars with different He content are characterized by the same luminosity, but different effective temperatures. In fact, He-rich stars are expected to have bluer colors, compared to He-poor stars. The helium abundance variation allows to identify different stellar populations through wide color baselines. Among them, combining optical photometry with UV CMDs is a valuable strategy to see He-enhancement for different sub-populations, as in the case of the baseline $m_{\rm F275W} - m_{\rm F814W}$. This is employed to reach subtle He content differences of even less than $\Delta Y = 0.01$ (see e.g. Milone et al., 2012d).

⋆ **Near-IR photometry.** This tool gives the opportunity to study MPs among the stars belonging to the M-dwarf population, namely low-mass stars having $M < 0.4\ M_{\odot}$. The most frequently utilized filters are the F110W and F160W of the WFC3/NIR camera onboard HST. These are specifically suited for the purpose, because observations in F160W are affected by the absorption of molecules containing oxygen (e.g. H_2O), while photometry in F110W is not that sensitive to variations in the oxygen content. This is the main reason why the color combination F110W-F160W facilitates the study of these stars. Over the last few years, promising research in the NIR has been adopted to investigate the low-mass stars regime (e.g. Milone et al., 2012e; Dondoglio et al., 2022).

⋆ **Two-color diagrams and pseudo color-magnitude diagrams.** MPs among various evolutionary phases are also identified through diagrams where far-UV, UV and optical filters are included. The most commonly used is the ($m_{\rm F275W} - m_{\rm F336W}$ vs $m_{\rm F336W} - m_{\rm F438W}$) two-color diagram. These combinations are rather intriguing, because passbands such as F275W and F336W encompass OH and NH molecular bands, whereas for example F438W covers CN and CH bands. Another fundamental combination is provided by Milone et al. (2013), combining the filters to produce the following pseudo color: $C_{\rm F275W,F336W,F438W}$=($m_{\rm F275W} - m_{\rm F336W}$)-($m_{\rm F336W} - m_{\rm F438W}$). According to the authors, this quantity enables to disentangle populations exhibiting variations in C, N, and O.

⋆ **Chromosome map (ChM).** This type of diagram represents an innovative tool which consists in a pseudo color-color diagram, introduced by Milone and other researchers, to unveil chemical differences among subpopulations in the

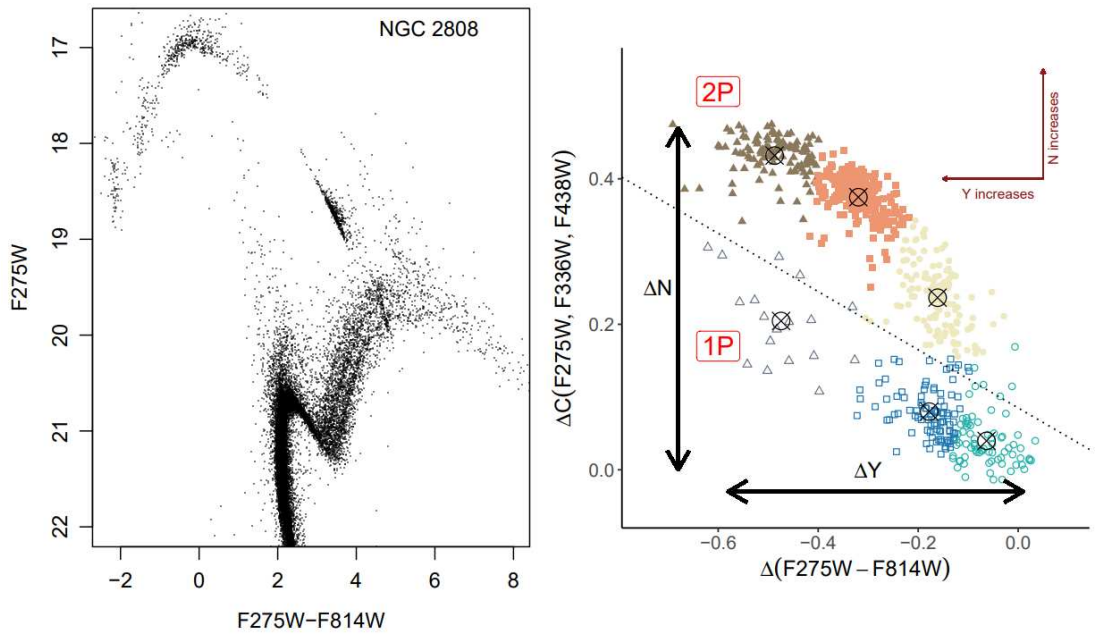

Figure 1.2: Two photometric diagrams for NGC 2808 are presented in the figure. On the left, an HST UV-optical CMD highlights the complex HB and RGB structures, associated to variations in the content of light elements (He, C, N and O). On the right is shown a chromosome map for NGC 2808 RGB stars. The content of He and that of N increase toward the left and toward the top, respectively. In this case, it is instrumental to define six distinct clumps of stars, for multiple 1P and 2P sequences. The figure is taken from Bastian & Lardo (2018).

UV photometry (see Milone et al., 2015). Such a diagram can address one evolutionary stage at a time, to disentangle different populations belonging to the MS, RGB, or AGB, separately. For these stars, a major difference with respect to the standard two-color diagram is that the sequences are verticalized in both dimensions. Therefore, each stellar population is observed as clustered in a confined region of the ChM, depending on its peculiar chemical composition. A ChM really enables to distinguish multiple stellar groups, based on the fact that it is built from colors sensitive to a specific composition. One illustrative example is the ChM of Figure 1.2 which exploits the $m_{\rm F275W} - m_{\rm F814W}$ color, sensitive to variations in the He content, and the $C_{F275W,F336W,F814W}$ pseudo-color, used as a proxy of N abundance. Another efficient ChM is devoted to the exploration of M-dwarfs: specifically developed to identify stellar populations based on the O content, it combines photometry in NIR ($m_{\rm F110W} - m_{\rm F160W}$) and optical bands ($m_{\rm F606W} - m_{\rm F814W}$) (refer to Milone et al., 2017b, for more comprehensive details).

The revolutionary tools of new CMDs and the impressive ChMs indicate, in most of the GCs, the existence of many distinct groups of stars. These multiple blobs are fundamentally grouped into two populations, namely the first population (1P) much more akin to galactic-halo-field-like-stars, and one or more 'second' populations (2Ps) enriched in helium (He), nitrogen (N), aluminum (Al) and sodium (Na), although depleted in carbon (C) and oxygen (O), with respect to field stars of the

same metallicity. It has been done an impressive work on the topic, during the past decade, both exploiting ground-based spectroscopic surveys of thousands of stars, focusing on abundance patterns, along with space-based photometry, giving unique views of the number and the species of different populations found in GCs. In fact, among the most exceptional cases it must be emphasized Omega Centauri (ω Cen), the analysis of which brought attention to the mindblowing amount of 15 subpopulations. Figure 1.3 shows a CMD which highlights the MPs found inside ω Cen (Bellini et al., 2017).

MPs retrieved in GCs exhibit somehow dramatic changes, from one cluster to another. Nevertheless, it is remarkable how certain common properties are revealed when the appropriate color combinations and ChMs are utilised. The main of them are the following:

- *Wide range and diversity.* Almost all the studied GCs show evidence of broad or split sequences, consistent with MPs. However, it gets challenging to explain the star formation history (SFH) of each GC, due to the wide spectrum of extensions and morphologies of ChMs (see Milone et al., 2017a, for more details).

- *Discreteness of stellar populations.* Stars belonging to 1P and 2P are quite easy to disentangle, as they tend to clump into distinct groups on ChMs, rather than forming a continuous distribution of stars, which would instead be more typical of the Galactic bulge. A clear pattern of discrete populations of stars is depicted in Figure 1.4, considering some ChMs to enhance the separation among them, for several GCs (Milone et al., 2017a).

- *Ubiquity.* The occurrence of MPs inside GCs seems to be a universal characteristic, observed in the Milky Way (MW) as well as in star clusters of the Small Magellanic Cloud (SMC) and the Large Magellanic Cloud (LMC) (Lagioia et al., 2019; Mucciarelli et al., 2009; Dalessandro et al., 2016), the Fornax galaxy (Larsen et al., 2014), and the Andromeda galaxy, M 31 (Nardiello et al., 2019). However, some exceptions do exist. For example, according to Villanova et al. (2013), Terzan 7 is a galactic GC that seems to be consistent with an SSP.

- *Two main GC classes.* GCs are identified as either Type I or Type II (anomalous GCs), based on the number and complexity of stellar sequences revealed in ChMs (Milone et al., 2017b; Marino et al., 2019). The majority of them are Type I GCs, harboring two main groups of stars: 1P, having low N and He abundance, and 2P, enhanced in these elements. Conversely, the category of anomalous GCs represents a smaller fraction (15–20% of GCs), and hosts 1P and 2P, together with at least a third group of stars. The latter are more complicated GCs, because the third ensemble of stars occupies a ChM region associated to high N but low He content. One example of this classification is provided in Figure 1.5, comparing a ChM of each of the two types. It was proposed to classify these clusters based on the chemical anomaly that they

exhibit, such as the spread in Fe or s-process elements (see Marino et al., 2018, for an extensive discussion).

- *Dependence on the cluster mass.* Another relevant feature concerns the relative number of 1P and 2P stars. The ramification of the MPs issue increases with the cluster mass. As a matter of fact, the more massive the GC, the more evident the predominance of strange-chemical-composition stars, even though it strongly depends on the examined GC. This is observed for example in the aforementioned ω Cen, which is likely to contain more than 90% of 2P stars and just a tiny fraction of stars with pristine chemical composition. Basically, the fraction of 2P stars represents the 40% up to the 90% of the total, moving toward the most massive GCs. Some relevant investigations were pursued, observing that the fraction of 1P stars sure anti-correlates with both the current and the original GC mass (see e.g. Milone et al., 2020a). On the contrary, it seems that the variations of internal He and N content correlate with the cluster mass.

- *Helium enrichment.* Detecting and measuring the He content from spectroscopy is a rather challenging task to perform. As a matter of fact, modern spectroscopy can reliably highlight such element in the spectra of HB stars, within the temperature range ∼8000–11,500 K: He lines in the optical regime are not sufficiently pronounced in colder stars, while hotter stars are interested by the process of He settling. He abundance variations among MPs are therefore studied through multi-band photometry, as clarified in the previous paragraph referred to the most widely used photometric tools. The method consists of comparing the colors of stellar populations observed in the photometric diagrams with the ones extracted from synthetic spectra characterized by a specific chemical pattern (Milone et al., 2012e). It is then possible to provide estimates of the relative He content of 1P and 2P in a GC. On average, the maximum intrinsic He fluctuations of GCs range from $\Delta Y_{max} < 0.01$ to $\Delta Y_{max} \sim 0.18$ (Milone et al., 2018b; Zennaro et al., 2019).

- *Elemental correlations and anti-correlations.* Along the entire stellar evolution path, 2P stars exhibit similar behaviour, as for example both RGB and unevolved MS stars share a different content of certain chemical species, compared to 1P stars. Various patterns have been well identified: this includes correlations and anti-correlations. A quite ubiquitous feature among GCs' MPs is represented by Na-O and C-N anti-correlations, coupled with Na-N and C-O positive correlations. On the contrary, only a limited number of massive GCs show internal variation of Mg, Al, Si, underlined by Mg-Al anti-correlation and Al-Si correlation (see e.g. Kraft, 1994; Gratton et al., 2004, 2019). One even more particular aspect refers to the Li content: in a subset of clusters, Li-O correlation (hence Li-Na anti-correlations) are detected; however, Li measurement are not widely accessible. The mentioned light elements are associated to different temperatures and phases of stellar nucleosynthesis, therefore, they provide access to sites where they were formed, to gather insightful information on the stellar evolution phenomenon. Several elemental

correlations are shown in Figure 1.6.

- *Depencence on GC orbit and on host galaxy.* Mostly, GCs with large perigalactic radius host larger fractions of 1P stars, compared with smaller-perigalactic-radius clusters (Milone et al., 2020a; Zennaro et al., 2019). What is even more remarkably fascinating is that GCs belonging to the LMC and to the SMC host more 1P stars than MW GCs. Observations suggest that the 1P/2P fraction within a GC could depend on the actual host galaxy.

- *No dependence on stellar mass.* Exploring MPs in NIR bands, with HST photometry, allowed to obtain a fundamental result: it is likely that the chemical composition of different stellar populations is independent on the addressed stellar mass range (Milone et al., 2014). This was established also for the mass range between $\sim$0.25 and 0.80 $M_{\odot}$, by Dondoglio et al. (2022).

- *Spatial distribution.* What differentiates several GCs is that 2P stars appear more centrally concentrated than 1P, which is the case of, for example, 47 Tucanae (47 Tuc), ω Cen, and NGC 2808 (Sollima et al., 2007b; Bellini et al., 2009; Milone et al., 2012e; Cordero et al., 2014; Lee, 2019). Despite that, MPs in other clusters (e.g. NGC 6362 and M 5) exhibit comparable radial distribution among each others (Nardiello et al., 2015; Dalessandro et al., 2018; Milone et al., 2019).

- *Internal kinematics.* Certain massive GCs, such as 47 Tuc or ω Cen, reveal more radially anisotropic velocity distribution of 2P, in contrast to the primordial population 1P, validating the scenario in which 2P stars are initially more centrally concentrated (Bellini et al., 2018; Richer et al., 2013). In any case, 1P and 2P indicate aligned behaviour, for other less massive clusters, as M 4, possibly because their initial anisotropies have been smoothed out by dynamical relaxation processes (Cordoni et al., 2020).

For the assorted set of GCs, the properties listed here are the most common and those about which astronomers question themselves the most, trying to identify plausible formation scenarios.

1.2 The possible formation scenarios

Since the identification of the phenomenon involving multiple stellar populations, several potential scenarios were formulated in an attempt to unveil their origin. More specifically, the purpose is to clarify the obscurity behind all these properties, in order to properly respond to questions concerning topics such as stellar evolution, stellar nucleosynthesis and star formation, even at high redshift. The current classification includes two possibilities: MPs may be the outcome of either a *Multiple Generations* scenario or a *Single Generation* scenario.

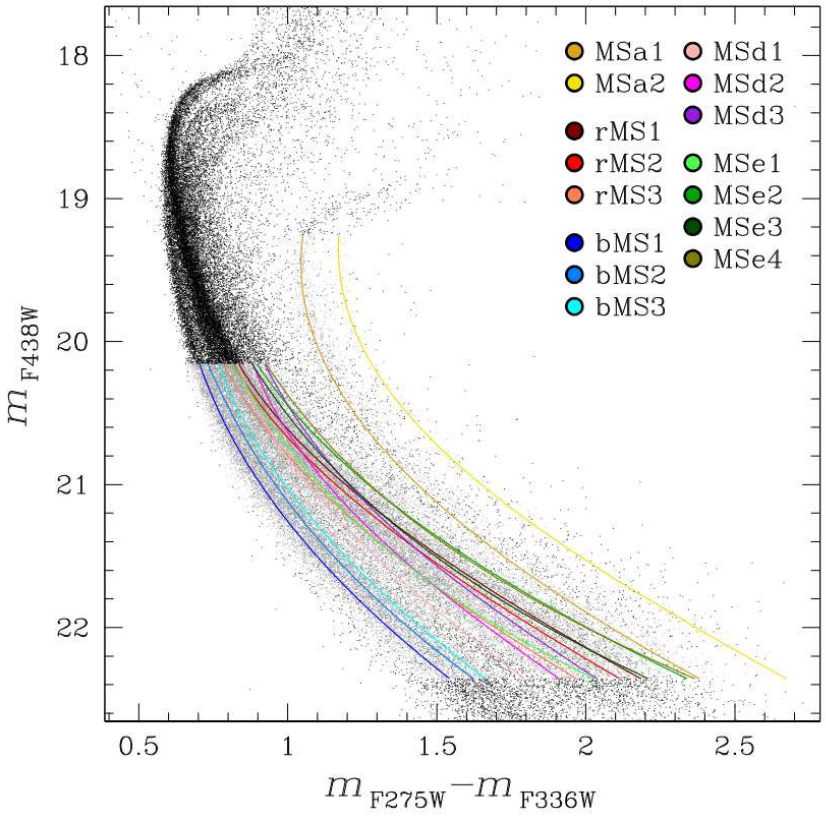

Figure 1.3: m_{F438W} vs $m_{\mathrm{F275W}} - m_{\mathrm{F336W}}$ CMD of ω Cen. In the diagram, 15 subpopulations have been identified among the cluster's MS stars. The image is taken from Bellini et al. (2017).

1.2.1 Multiple Generations scenarios

Based on Multiple Generations scenarios, GCs could have experienced multiple events of star formation with multiple star-formation bursts, each responsible for one individual sequence observed in the photometric diagrams. Hence, the different stellar populations could be explained in terms of distinct stellar generations. According to this, the reason why 1P stars exhibit their galactic-halo-field-like chemical composition, is that they formed during a first star formation episode, within a homogeneous pristine cloud. Then, the most massive 1P stars evolved and ejected the processed material, polluting the environment inside which further generations (2P stars) formed. Various interpretations and hypotheses have been formulated to corroborate this scenario.

The most appealing and popular possibility is the *Asymptotic Giant Branch scenario* (AGB scenario) as suggested by several researchers (e.g. Cottrell & Da Costa, 1981; D'Antona et al., 1983; Ventura et al., 2001). One version of the model was proposed by D'Ercole et al. (2010) and it validates the formation of a GC first generation of stars (1P) with a full initial mass function (IMF): among them, the most massive stars reach temperatures high enough to undergo advanced nuclear burning phases, and to synthesize heavier elements. Within the first Myrs, stellar feedback from high-mass stars combined with core collapse supernovae (SNe) explosions wipes the intra-cluster medium (ICM), removing and pushing outward the pristine

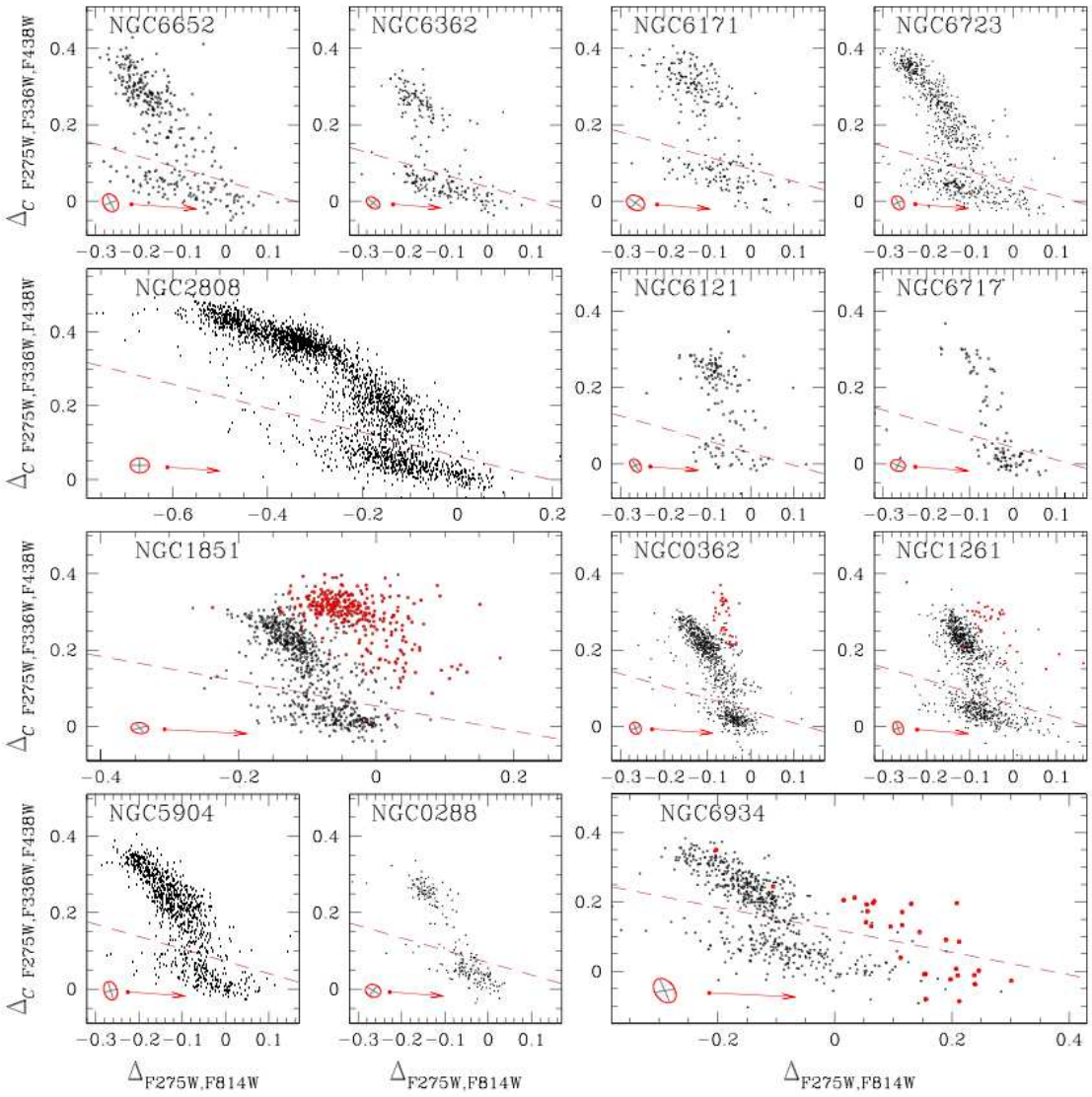

Figure 1.4: Collection of ($\Delta_{C\ \mathrm{F275W,F336W,F438W}}$ vs $\Delta_{\mathrm{F275W,F814W}}$) chromosome maps. Each panel depicts the distribution of MPs among RGB stars identified for one among the 13 GCs considered. To disentangle 1P from 2P stars is utilized a dashed line in each diagram. This atlas of clusters is illustrative of the variety and complexity typical of the phenomenon of MPs. The figure is proposed by Milone et al. (2017a).

material, as well as the newly-released metals. After ∼30 Myr, SN events are not expected anymore, whereas intermediate-mass stars (within the mass interval ∼3–8 $M_{\odot}$) become AGB: it is a relevant step, setting the start of the hot bottom burning (HBB) process. What happens now is that the outermost convective envelope of AGBs reaches a substantial depth, corresponding to temperatures of ∼30–40 MK, hot enough to trigger the more advanced p-capture process (Ventura et al., 2013). Furthermore, as AGB, a star experiences the *Dredge Up*, a similar mechanism to HBB, which allows the convective envelope to access internal layers that have been interested by the CNO-cycle. Such regions undergo convective chemical mixing, where the products of the CNO-cycle are brought up to the surface. Stellar winds

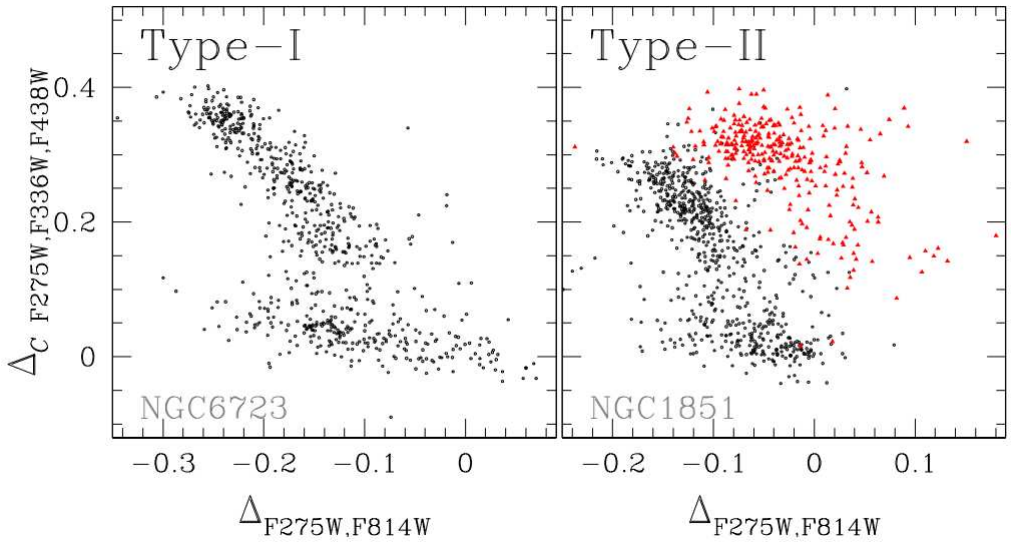

Figure 1.5: Comparison of the ChMs of NGC 6723 (on the left) and NGC 1851 (on the right). These GCs can be considered prototypes of Type I and Type II GCs, respectively. The abundances of He increases toward the left, whereas the N content increases toward the top. In red are highlighted also red-RGB stars of NGC 1851, on the right panel. Taken from Milone & Marino (2022). Photometry from Milone et al. (2017a).

from AGB stars eject part of their enriched envelope, which then diffuses in the cluster environment. If the ejecta velocities are lower than the cluster's escape velocity, the cluster could retain the matter. It is exactly from this chemically-enriched material that a new second generation or even multiple generations of stars can form, once a critical density is reached. The model suggests that forthcoming episodes of star birth arise in the cluster center, where the cooling-flow occurrence grant the buildup of AGB-processed material, together with the primordial one. Dilution of the original gas in this fashion could represent a decisive factor for the AGB scenario, as it would allow the reproduction of the observed Na-O anti-correlation. Moreover, according to this hypothesis, a great amount of GC 1P stars are lost during the initial stages of the GC development, through the external-regions-expansion, due to SNe events. On the contrary, the typically observed 2P central accumulation, is likely the outcome of the retainment experienced by the proto-cluster (D'Ercole et al., 2008, 2010; D'Antona et al., 2016).

Another theoretical model is the *Fast Rotating Massive Stars scenario* (FRMS scenario), developed by Decressin et al. (2007a,b). Almost similarly to the AGB scenario, according to the FRMS hypothesis, the polluters candidates are massive stars, responsible for the formation of chemically anomalous new stars that may follow the first stellar burst. In this case, massive stars (∼25–150 $M_{\odot}$) undergo fast rotation which induces the internal blending of freshly-synthesized chemical species. Hence, in a GC which is much younger (<10–20 Myr) than predicted by the AGB scenario, these high-mass stars get nearly fully mixed. Later, the enriched material ascends to the surface and is released into the ICM. The scenario is refined by Krause et al. (2013) considering that after 1P stars form, the young GC may

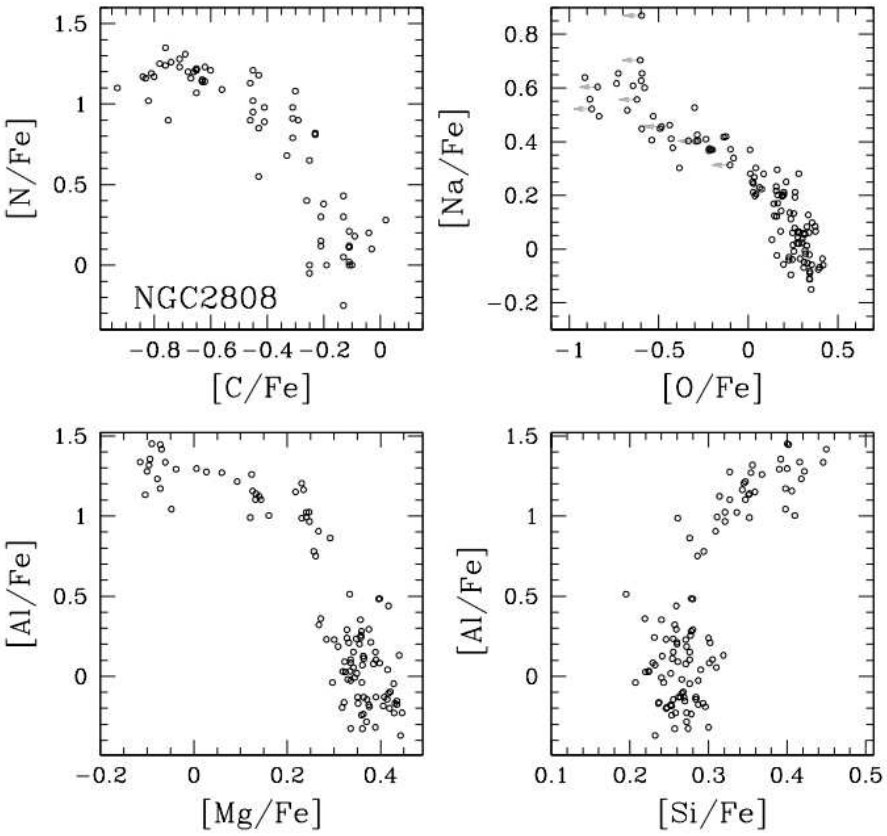

Figure 1.6: In the figure are observed the aforementioned C-N, Na-O, and Mg-Al anti-correlations, as well as the Al-Si correlation for MPs of NGC 2808. As regards C and N abundances, they refer to Carlos et al. (2023), while the others are taken from Carretta (2015) and Carretta et al. (2018).

be still incorporated within the natal cloud. In principle, the authors suggest the development of an equatorial stellar disk around the FRMS, due to the accumulation of matter thrown away as it rotates close to the break-up limit. Subsequently, new stellar populations are formed from gravitationally unstable disks made up by FRMSs' ejecta diluted with the retained gas, which is the left over of the original GC cloud. One difficulty of this interpretation arises from the observational constraint of 2P location. In fact, in agreement with the FRMS scenario, 2P stars would be found not only in GCs, but also in the galactic halo field, surely in contrast with observations.

In alternative to the previous ideas, De Mink et al. (2009) proposed the *Massive Interacting Binaries scenario* (MIBs scenario), namely the possibility that one or more populations of chemically-anomalous stars form from the material polluted by massive binaries. The authors modelled the evolution of a binary system composed by a 20 $M_{\odot}$ star interacting with a 15 $M_{\odot}$ companion: the system expels the majority of the primary star envelope, for the amount of 10 $M_{\odot}$ of stellar yields. According to the hypothesis, such an ejecta would be retained by the proto-GC potential well. Then, second generations of stars would form there, where the chemical composition resembles that of 2P stars, allowing to reproduce, for one, their typical Na-enhancement and O-depletion. A relevant aspect regarding the MIBs scenario

is that it may explain the variety of GCs.

From the observations, the discreteness property represents a major challenge for these models. In fact, based on the theoretical subsequent distinct stellar bursts, it is reasonable to have many different chemical compositions, associated with discrete stellar populations, confirming the AGB scenario. Opposite is the close analysis of discrete MPs in the context of the FRMS scenario. Following this model, the stars are not expected to distribute among discrete clumps associated with different chemical abundances, but rather in a continuous fashion.

All these three multi-generations scenarios share a common issue, namely the so-called *Mass-budget problem*. This is probably the main challenge and opportunity to understand the connection between MPs within a GC, and also GCs' contribution to the re-ionization of the universe. In fact, in present-day GCs there is a widespread predominance of 2P stars compared to 1P: this is not compatible with the hypothesis stating that 2P stars are the outcome of the pollution generated by 1P. A possibility could be that the population of progenitors was much more massive at formation, by a factor of ∼5-20 (e.g. Renzini, 2013). It is plausible that, through the cluster evolution, most of the primordial 1P were lost into the field. Therefore, it seems reasonable that they provided for the assembly of the Galactic halo, as well as the Bulge (see as a reference Renzini et al., 2015; Renzini, 2017).

1.2.2 Single Generation scenarios

Several are the challenges and perplexities given by *Multiple Generations* scenarios, like the *Mass-budget problem*, chemical anomalies resulting in large spreads (e.g. Carretta et al., 2013b), and also the range of abundance trends observed in GCs. Alternative models have been proposed, without invoking multiple epochs of star-formation. All the variants of the so-called *Single Generation* scenario propose that all GC stars are coeval, and the observed composition of multiple sequences is the result of some exotic event of accretion of polluted material. 2P stars would not form from the combination of pristine and enriched material ejected by previous generations, but they rather form concurrently with 1P, and then accrete polluted material released by other stars of the same generation.

One hypothesis, presented by Bastian et al. (2013) explores the possibility that low-mass pre-main-sequence (PMS) stars accrete polluted material released by co-eval high-mass interacting binaries and by FRMSs on their protoplanetary discs and eventually on to the young host stars. The model is known as the *Early disc accretion scenario*. The authors assume that massive stars are concentrated in the cluster center, due to a possible early mass-segregation. They suggest that 2P may form after low-mass stars ($<2\ M_{\odot}$) sweep up the chemically enriched material from their circumstellar disc, which should occur at the very beginning of PMS phase. Theoretically, such contracting PMS stars are still entirely convective and therefore, assuming the model to efficiently work, we expect the hot gas accretion to take place on time-scales shorter than ∼1-3 Myr (Salaris & Cassisi, 2014; D'Antona et al., 2014). Disc accretion has some limitations, as it does not fully explain the observed amount of pollution.

Another solution could be the *Super-Massive Stars* (SMS) scenario. As illustrated by Gieles et al. (2018), who developed an idea proposed by Denissenkov &

Hartwick (2014), one interpretation for the MPs could be the following. Super Massive Stars (SMSs) form concurrently with the host GC from massive stars that sink in the cluster center and coalesce there, as a result of adiabatic contraction and a dramatically high star-collision rate. These stars experience runaway collisions and soon start to eject the processed material, which gets diluted in the pristine gas. Strong SMS-winds interact with the inflowing cold gas, and this could trigger the enrichment of low-mass coeval protostars, without needing multiple starbursts in the cluster. Runaway collisions are expected for densities greater than $\sim 10^6$ stars. Moreover, the accretion rate for the gas should exceed $\sim 10^5\ M_\odot\ Myr^{-1}$. These conditions are likely reached at the formation of GCs, in a high-density environment.

The SMS model would allow a continuous rejuvenation. In fact, the authors predict that via stellar collisions, SMSs eject processed material and fresh hydrogen is therefore acquired by SMS-winds (Gieles et al., 2018). As a consequence, this produces an amount of ejecta which exceeds the maximum mass of SMSs, by one order of magnitude. The corresponding yields of SMSs show excellent agreement with the required mass budget and with the anomalous chemical composition of some GCs' stars, once the dilution with primordial material is accounted for.

So far, one problem has come up with this hypothesis, since these types of stars have only been simulated and not observed yet. However, the SMS scenario could explain and support the origin and existence of Intermediate-Mass Black Holes (IMBHs), compact objects covering the mass range $10^2 - 10^5\ M_\odot$, falling between stellar mass black holes (from few up to tens of $M_\odot$) and Super Massive Black Holes (SMBHs, showing masses of $\sim 10^5 - 10^9\ M_\odot$). Kızıltan et al. (2017) showed indirect evidence of an IMBH having the mass $\sim 2.2 \cdot 10^3\ M_\odot$ in 47 Tuc. This is already a remarkable result. However, we should further investigate, considering the analysis of gravitational waves using the promising VIRGO and LIGO interferometers.

1.3 The phenomenon of binaries

In the understanding of GCs, binary stars play an essential role. In fact, through the study of the binaries frequency it is possible to shed light on the clusters' dynamics and on their evolution, because those are definitely affected by stellar interactions occurring in dense environments represented by clusters (see, e.g. Heggie & Hut, 2003). A great ensemble of exotic objects detected in GCs may be the outcome of stellar evolution in a binary system. Examples of late evolutionary stages of tight binaries are Blue Stragglers (BSSs), milli-second pulsars, cataclysmic variables and X-ray binaries. Binaries are fascinating and extremely important, also for the interpretation of the phenomenon of MPs in GCs. Various scenarios propose that second-generation stars form within a high-density environment located in the center of a cluster (e.g. D'Ercole et al., 2008). The concept is that through the determination of the incidence of binaries among the MPs of a GC, we can set constraints on binaries' formation environment and evolution, due to the strong dependence on stellar density for the binary disruption rates and the surviving binaries parameters (see e.g. Vesperini et al., 2011; Hong et al., 2015). Some authors, like Vesperini, performed numerical studies, which show that it is expected a fraction of binaries in 2P lower than in 1P. Second-generation stars, 2Ps, are found more centrally concentrated (as explained in Section 1.1), and they are therefore more affected by

dynamical processes, responsible for further evolution, as well as events of binaries disruption. In addition, the effect of spatial mixing has a different efficiency, depending on the cluster's dynamical evolution, at any given time.

In literature are mentioned three main techniques, to estimate the fraction of binaries in GCs.

1. The first one is based on spectroscopy and indeed it relies on the individual binary systems detection, which is feasible only for the brightest GC stars. Binaries populations can be characterized through radial-velocity monitoring. However, the method depends on the availability of spectrographs with high capabilities (e.g. FLAMES@VLT), given that the statistics is still limited to smaller samples compared to photometric studies. The approach is biased toward short orbital periods and large inclination of the orbit. It is a promising method, already providing information on binaries' orbital parameters and their composition. Several results of recent works revealed a larger incidence of 1P binaries compared to that of 2P binaries, generally consistent with the theoretical predictions (e.g. D'Orazi et al., 2010; Dalessandro et al., 2018).

2. The second technique refers to photometric detection of eclipsing binaries (e.g. Yan & Reid, 1996). It is exclusively applicable to systems with large orbital inclination and short period. Through this procedure, we access periods information, and it is suitable at all evolutionary stages.

   Both the depicted methods are not notably efficient; furthermore, they necessitate multiple measurements to be conducted at different epochs, resulting in increased expenses, especially in terms of telescope time.

3. As stated by Milone et al. (2012b) a different methodology can be employed (a third procedure), analyzing the distribution of stars, with respect to the MS fiducial line. It represents a more efficient approach to derive the number of binaries, for at least three reasons:

   - it is a sufficiently statistically-robust analysis, because of the thousands of available stars;
   - a detection only requires two filters, with no necessity of repeated observations;
   - there is no bias toward a certain orbital period and inclination.

   Many published works employ the method just presented, for the investigation of binaries within a cluster (e.g. Sollima et al., 2007a, 2009; Bedin et al., 2008; Milone et al., 2009, 2010).

1.3.1 Observational evidences in GCs

Globally, it is observed a binary fraction among GC stars that confirmed a higher presence of binary systems in the field, rather than in GCs' center (Mayor et al.,

1992). Based on a sample of 21 binaries observed through radial velocity, Lucatello et al. (2015) derived a fraction of binaries among 1P stars larger than the value within 2P, by 4.1±1.7 times. Analogously, Dalessandro et al. (2018) pointed out that for the cluster NGC 6362, just 1 spectroscopic binary out of 12 is of 2P.

The finding is consistent with the expectation of a more effective binaries disruption in a concentrated environment, which is characteristic of a cluster. In addition, many authors extended the research to some open clusters and young star clusters, highlighting a larger fraction of binaries compared with that of GCs. It could be indicative of the fact that binary systems' evolution strongly depends on the star formation condition and on the environment.

Within a cluster, the essential process that influences the binary population is the interaction with cluster's stars. However, there are other non-negligible mechanisms: tidal-capture can lead to the formation of a binary system (e.g. Kroupa, 1995b); binaries can be destroyed due to tidal dissipation or through coalescence of the two companions (see e.g. Kroupa, 1995a); in a couple of tight binaries the interaction can efficiently result in the phenomena of collisions and mergers (e.g. Fregeau et al., 2003).

Several extensive tests have been done, to simulate the evolution of binaries, and estimate the fraction of expected binaries, to finally compare it to the observed binaries incidence. Some investigations include Monte-Carlo simulations (e.g. Ivanova et al., 2005), N-body (e.g. Fregeau et al., 2009; Marks et al., 2011) and fully analytical computations (Sollima, 2008).

As concerning the evolution of a binary system, the basic idea is that a cluster is a rather dense environment, characterized by high velocity dispersion, typically responsible for large relative velocities. Therefore, it is more likely for those systems to experience close encounters with other stellar objects, within the high-density innermost cluster regions, rather than in the field. Depending on the energy involved in the process, the encounters can either result in a more bound system (binding energy of the couple of stars exceeds the kinetic energy of the third object), or in a loose system of binaries, possibly even a disruption event (it is the opposite case, in which the kinetic energy is higher than the binaries' binding energy). These opposite outcomes are deeply explained through the Heggie's Law (Heggie, 1975), stating that within a GC or a similarly-dense environment, three body encounters can lead either to the softening of soft binaries or to the hardening of hard binaries (see the review by Heggie & Hut, 2003).

In general, the observational findings are in good agreement with the predictions. The study by Vesperini et al. (2011) follows the evolution of binaries in the context of MPs, through a hybrid procedure that consists of analytical-numerical analysis. The authors highlight that 2P stars are likely to form in a more centrally concentrated region, compared to 1P. Undeniably, this phenomenon leads to a higher rate of stellar encounters, increased disruption of binary systems, and to the subsequent lower fraction of 2P, rather than 1P binaries. In this case, N-body simulations by Hong et al. (2015, 2016) validate the hypothesis, concluding that the observational result could also depend on the separation between the binaries: we do not expect tight binary systems to be affected.

The majority of the mentioned studies are usually limited to the GCs' innermost region, where dynamical processes are likely to erase the initial configuration and

distribution of 1P and 2P stars. It is therefore unquestionable that a more extensive, homogeneous and accurate inspection, focused on the proper motion, radial velocity, and spatial distribution of the binaries among different generations of stars, is required.

The future analysis of observations coming from more modern space-based facilities, the combination of multi-wavelength data in addition to joined spectro-photometric efforts, are expected to help understanding which is the most favourable scenario for the formation of MPs within a GC. Furthermore, through the comparison with simulations provided by advanced codes, it could be addressed and investigated the prospected evolution that each population (and the included binaries) could have.

1.3.2 Binaries and multiple populations

The environment provided by a GC, as defined in the previous paragraph, is characterized by high stellar density, accountable for the survival of tight binary systems mostly. As a consequence, it is not possible to resolve individual components in HST images: binaries are observed and treated as a single point source. Assuming that the stellar pair is a non-interacting one, the position on a CMD depends on the combined light of the two companions. The analysis is performed with the following assumptions: the components have the fluxes F_1 and F_2, and the magnitudes $m_1 = -2.5 log F_1 + constant$ and the corresponding m_2. The resulting binary system appears as a single star, exhibiting the magnitude:

$$m_{bin} = m_1 - 2.5 log\left(1 + \frac{F_2}{F_1}\right). \tag{1.1}$$

Theoretically, for an SSP, two stars of the same luminosity and mass (M_1 and M_2) form a sequence running parallel to the fiducial line of the GC, associated though to a magnitude value brighter by the amount of $\sim$0.75 mag. In case of different luminosities and masses, the binary stars are expected to populate the CMD region between the single-stars fiducial line and that of equal-mass binaries. The point on the CMD associated to the star corresponds to that of a redder star, brighter than the primary companion. Fundamental in this analysis is the parameter of the mass ratio $q = \frac{M_2}{M_1} \leq 1$. An explicative image is presented in Figure 1.7, taken from Milone et al. (2012b).

The next Figure 1.8 by Milone et al. (2020b) illustrates the fiducial lines associated to binaries of a certain population, defining the method employed to estimate, among MPs, the binaries frequency. Panels (*a1*) and (*a2*) represent the ideal situation of stars belonging to 1P only: on the ($m_{\rm F814W}$ vs $m_{\rm F606W} - m_{\rm F814W}$) CMD and on the ($m_{\rm F814W}$ vs $C_{\rm F275W,F336W,F438W}$) pseudo-CMD are illustrated 1P stars, with red lines. The continuous and dashed line are associated, respectively, to single stars and to binaries of the same population having the same luminosity. The large red star symbol corresponds to the predicted observation of a binary system with the companions of magnitude $m_{\rm F814W}$=16.7 and $m_{\rm F814W}$=18.2, indicated with two smaller stars on the continuous red line. Some similar approach is applied to single 2P stars and 2P-2P binary systems sharing the same luminosity, with the blue continuous and dashed lines, in panel (*b1*) and (*b2*). These fiducial lines are traced on top of

the 1P red lines. The blue big star's position on the diagrams corresponds to that of a 2P-2P binary system composed by the small blue stars. Relevant is the difference in the location of this 2P-2P theoretical binary with respect to the 1P-1P binary, in panel (*b2*), rather than in (*b1*), where they exhibit similar $m_{\rm F606W} - m_{\rm F814W}$ colors. Instead, the bottom panels in figure depict the case of mixed binaries, where the gray lines indicate a population of 1P-2P equal-luminosity binaries. As this goes beyond the purpose of this thesis, the case is not analyzed deeper.

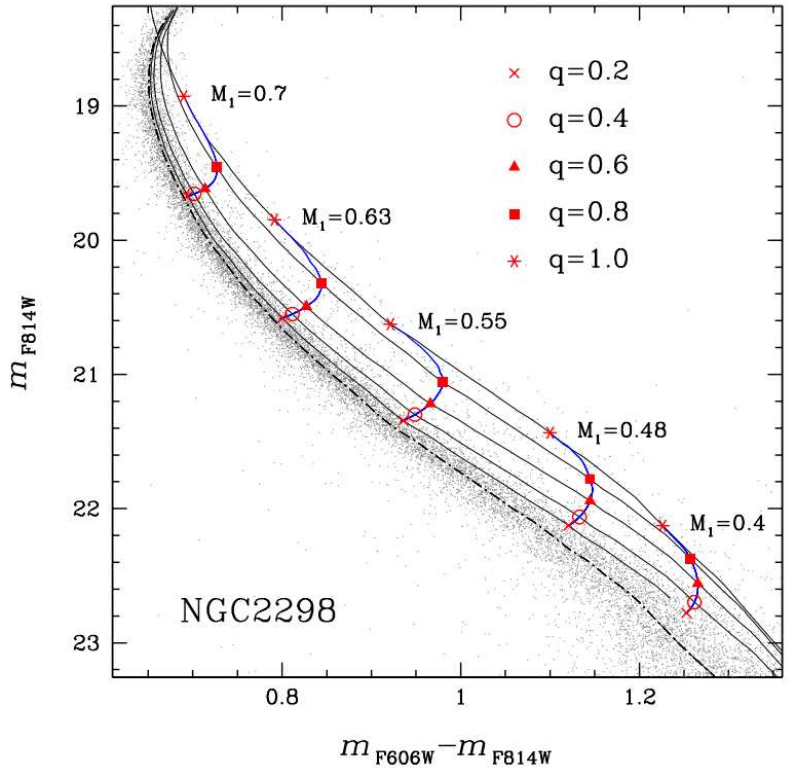

Figure 1.7: $m_{\rm F814W}$ vs $m_{\rm F606W} - m_{\rm F814W}$ CMD for the GC NGC 2298. On the plot, the continuous lines indicate the theoretical lines associated to MS binaries of different mass ratios $q = \frac{M_2}{M_1}$. These are proposed in comparison with the black dash-dotted line, a fiducial line which traces MS single stars. Taken from Milone et al. (2012b).

1.4 Very Low-Mass stars

The stellar domain of Very Low-Mass (VLM) stars is obtaining burgeoning attention, particularly in the context of studying MPs inside GCs. Indeed, the most studied spectral range covers wavelengths from the UV to the NIR region (λ∼2000–8000 Å), where multiple sequences can be detected for stars which are more massive than ∼0.6 $M_\odot$, while the exploration of lower masses gets challenging. The reason is that the VLM stars, corresponding to masses between ∼0.5 and ∼0.1 $M_\odot$, having low effective temperature, typically exhibit their spectral peak in the NIR (λ>8000 Å),

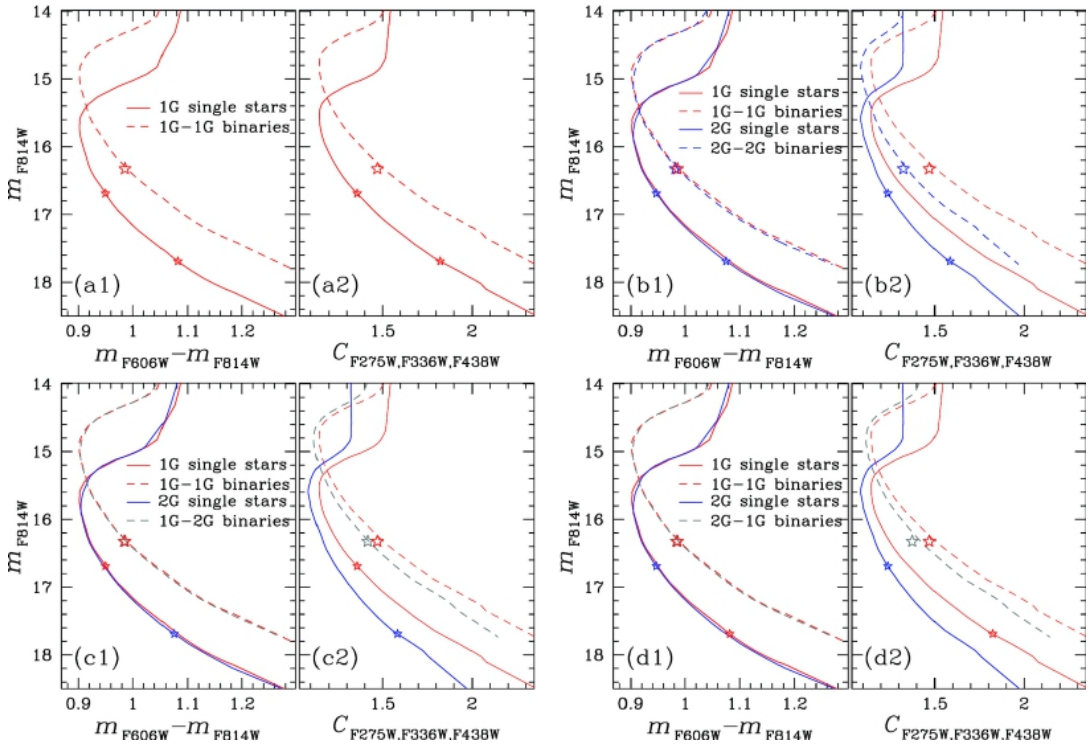

Figure 1.8: The eight panels present the ($m_{\rm F814W}$ vs $m_{\rm F606W} - m_{\rm F814W}$) CMDs and ($m_{\rm F814W}$ vs $C_{\rm F275W,F336W,F438W}$) pseudo-CMDs. The figure illustrates a useful comparison of the location expected for single stars and binaries, belonging to 1P and 2P. More details are provided in the text. The image is taken from Milone et al. (2020b).

too faint to be accurately revealed by optical and UV photometry. This almost-unexplored stellar mass regime is attractive, especially because it could offer pivotal insights to distinguish between various formation scenarios.

The two main scenarios (*Multiple Generations*, Section 1.2.1, and *Single Generation* scenarios, Section 1.2.2) correspond to different expectations, as regarding the pattern of the populations across stellar masses. According to the *Multiple Generations* scenarios, 2P stars result from a later burst of star formation, occurring within a homogeneous gas cloud where pristine material has been mixed with the processed one ejected by 1P stars. This suggests that both high and low-mass stars born during each star-formation episode should display comparable chemical composition. On the other hand, based on scenarios accounting for an accretion-like mechanism, 2P stars are likely protostars that accrete polluted material ejected by more-massive 1P stars of the same generation. A similar framework is described through models, which, depending on the specific case, indicate that the accretion rate depends on the mass of the accreting object. The Bondi-like accretion (Bondi & Hoyle, 1944), for example, expresses a direct proportionality with the square of the stellar mass, $\dot{M} \propto M_{\star}^{2}$. Such a model suggests that the accretion would be systematically less efficient among the less-massive M-dwarfs, producing smaller internal variations of He, C, N, and O, compared to those measured for massive stars, like the RGBs.

The concept is to compare the MPs' properties over a broad mass range, testing

the formation scenarios, starting from the analysis of chemical differences.

1.4.1 Literature studies on VLM regime

Currently, among the available HST filters, the most suitable ones to study MPs among VLM stars are F110W and F160W onboard WFC3/NIR (see Section 2.1 for the description of the instrument). As mentioned in Section 1.1, the F160W band is strongly affected by absorption of several molecules which contain O (e.g. CO, H_2O, OH, TiO). Among them, water represents the most effective source of opacity. The other filter, F110W, instead, is poorly affected by such molecules. The major difference between 1P and 2P stars, as clarified in the previous paragraph 1.1, concerns the different chemical abundances: 2P exhibits lower O content with respect to 1P. This is particularly noticeable in diagrams like the ($m_{\rm F160W}$ vs $m_{\rm F110W} - m_{\rm F160W}$) CMD, where stars below the MS knee are distinguished in a redder and brighter population, associated to 2P stars, and a bluer population, 1P.

The first observation and analysis of multiple stellar sequences among VLM stars has been conducted by Milone et al. (2012e), studying NGC 2808. Through their project, the authors focused on the lower part of the MS, called the MS knee, exploiting data gathered exactly with the HST filters F110W and F160W. For the first time, through the NIR diagram, they could examine the behaviour of the cluster MS stars in the low mass regime. At bright magnitudes ($m_{\rm F160W} < 20.5$) they notice three sequences which merge together at the level of the MS knee. Moving toward fainter magnitudes, disentangling the distinct populations gets more enigmatic, because of a combination of stellar structure and atmospheric effects. In fact, according to their analysis, on one hand the colors are shifted to the red, due to increasing radiative opacity connected to decreasing effective temperature. On the other hand, the stellar flux also reaches bluer colors accordingly to the increase of collisional-induced absorption (CIA) of H_2 in the IR. These effects balance each others, producing an almost vertical distribution of MS stars. However, decreasing the stellar mass, the second effect gets predominant, forming sequences that are particularly shifted to bluer colors. Two sequences are identified among VLM stars in NGC 2808. Their properties are better characterized through isochrones, in order to compare the observations with evolutionary models. The researchers could distinguish a halo-field-like population of stars exhibiting primordial He content, O-C enrichment and low N abundance, which encompasses ∼65% of the MS stars, and another population, representative of a second generation of stars enriched in He and N, though depleted in C and O.

More recently, the research by Dondoglio et al. (2022) aimed to compare the variations in light elements content for VLM stars with those of high-mass stars, in the attempt of testing different formation scenarios. They analyzed a sample of nine GCs and one open cluster employing high-precision photometry in the filters F110W and F160W. One result is that, below the MS knee, five GCs, namely 47 Tuc, NGC 288, NGC 2808, NGC 5139, and NGC 6121 (M 4) show a bimodal color distribution, while for NGC 6752 they distinguish a triple MS in the VLM regime. The intrinsic broadening in the color $m_{\rm F110W} - m_{\rm F160W}$, an effect of different oxygen abundances, is attributed to the presence of MPs among M-dwarfs. Another suggestive finding of the research is the comparison of the color spread width ($W_{\rm F110W,F160W}$)

measured below the knee, with the difference in the amount of O (Δ[O/Fe]) of 1P and 2P studied by Marino et al. (2019) through spectroscopy of RGB stars. They find an anti-correlation between the two quantities of $W_{\mathrm{F110W,F160W}}$ and Δ[O/Fe]. This trend is illustrative of larger oxygen content variations with increasing color spread associated to VLM stars. It is also confirmed that the open cluster NGC 6791 does not exhibit O variations, as it shows a color spread compatible with observational errors alone (see Bragaglia et al., 2014). Additional effort is dedicated to the study of the Mass-Function (MF) of two chemically-different populations of M-dwarfs within M 4 and NGC 2808. The MF slope is not characterized by a variation considering the regions above and below the MS knee. According to this result, we should rule out the Bondi-like accretion scenario as the one responsible for 2P formation. In fact, we would expect a strong difference between the Initial MF (IMF) of 1P and 2P, plausibly owing to the formation of 2P in a much denser environment. Therefore, the conclusion by Dondoglio and collaborators favors a scenario where the different populations originated with similar IMFs, at least in the low-mass regime. Moreover, they suggest that the formation of M-dwarfs may not be significantly affected by the formation environment density.

Even more fascinating is the exploitation of data collected with James Webb Space Telescope (JWST) that is now becoming available. The detection of MPs in the VLM regime has been reinforced by the analysis conducted on 47 Tuc (Milone et al., 2023a), M 92 (Ziliotto et al., 2023) and NGC 6440 (Cadelano et al., 2023). In addition, Marino et al. (2024) explored 47 Tuc below the MS knee, going beyond the hydrogen-burning limit, reaching the brown dwarfs. The work demonstrates the capability and the potential of JWST investigating VLM stars. Among the results of this latter research, photometric diagrams constructed using the filter F322W2 of NIRCam corroborate the evidence of MPs among M-dwarfs, for masses larger than $\sim$0.1 $M_{\odot}$ (previous studies among VLM stars are conducted by Dondoglio et al., 2022; Milone & Marino, 2022; Milone et al., 2023a). This JWST project also indicates the consistency of the M-dwarfs' MS color broadening with different oxygen contents, not to mention that it enables to find a distribution in the difference of O abundance, comparable with that observed through spectroscopic studies of RGB stars. Moreover, for the first time, the paper presents the spectroscopic determination of the chemical composition of M-dwarfs belonging to a GC. Comparing the spectrum of a 1P-star and a 2P-star, with synthetic spectra, it is revealed a strong flux difference among the two populations. The strong O absorption feature of 1P, in contrast with the O-depletion of 2P, validates and extends the already-known property of O-difference of MPs to the category of M-dwarfs. The deep CMDs obtained give the opportunity to analyze the F322W2 luminosity function: the authors highlight a gap and they provisionally associate it with the hydrogen-burning limit.

1.5 Thesis layout

This Chapter was dedicated to a comprehensive presentation of the MP phenomenon among GCs: I provided details on their properties and on some reasonable formation scenarios proposed in literature. Then, I focused on binary systems found inside GCs' MPs, distributed accordingly to the population to which they belong. Among the greatest and most puzzling features of MPs, I drew attention to the mass regime

concerning VLM stars.

In this work, in the next Chapters, I obtain multi-band photometric data from the HST images, to explore the faintest MS stars of the globular cluster 47 Tucanae. First of all, in the context of the phenomenon of MPs, the thesis aims to analyze the stars observed below the MS knee, for the first time in the blue filter F475W. The concept is to investigate the features exhibited by 47 Tuc on a photometric diagram which includes such a filter. Second of all, it is conducted the analysis of several photometric catalogs, combining F475W data with already-available IR and optical data, to characterize the distribution of binary systems along the MS, below the MS knee. The stars are distinguished for the first time into four generations, to constrain the frequency of binaries among multiple populations. A prevalence of binaries belonging to the first generation would confirm the hypothesis of a higher disruption and ejection of second generation binaries, compared to the first generation.

The thesis is organized as follows. Chapter 2 describes the photometric dataset for 47 Tuc and the procedure employed to reduce it. Chapter 3 presents the examined target in details and a few diagrams produced. In Chapter 4 are illustrated the data analysis and the discussion of the results. The conclusions of the thesis are then summarized in Chapter 5.

Chapter 2

Data reduction

In this Chapter are presented the methods used to perform data reduction. More specifically, it is organized in the following sections. Section 2.1 presents a brief description of the instrumentation on board HST used to collect the images investigated in the thesis. The precise data set on which I worked is illustrated in more details in Section 2.2. The next Section 2.3, 2.4, 2.5 and 2.6 are dedicated to the comprehensive explanation of how data are reduced from the manipulation of raw images, to the final set of calibrated and corrected images. Some impressive CMDs resulting from data reduction are presented in the next Chapter 3.

2.1 Instrumentation

The intense work and the extensive photometric data gathered by the HST through over 30 years have played an essential role in the characterization of MPs within GCs. Launched in 1990, HST is nowadays still one of the most powerful space-based telescope, provided with different instruments, allowing to produce large wavelength-band data and high-resolution images. HST orbits around Earth at the altitude of $\sim$540 km and therefore it has the advantage of avoiding atmospheric distortion, which allows to produce diffraction limited images. Another crucial aspect of HST is that it can observe at wavelengths that on ground we are prevented to access. Indeed, being a space telescope, HST gets clearer and deeper observations of crowded sky regions, which is typically the case with GCs. In fact, the comprehension of the phenomenon of MPs is gradually increasing, also thanks to the fundamental exploration of GCs through HST, in the UV spectral region. It allows, among other scientific goals, to identify stars with different He and light elements content.

HST has a primary mirror of 2.4 m and it performs observations covering a very wide wavelength range, from the UV regime at $\sim$100 nm to the NIR region at $\sim$1700 nm. It is equipped with a great number of cameras, each of them operating on a certain Field of View (FoV) and sensitive to a specific wavelength range. In particular, in this study, the images were gathered with two instruments: the Advanced Camera for Surveys (ACS) and the Wide Field Camera 3 (WFC3).

The thesis purpose of investigating binaries among MPs is achieved analyzing a huge dataset, which includes images gathered with ACS and with WFC3. First of all, my original contribution consists in the reduction of images of 47 Tuc acquired using ACS only. The specific dataset is presented in the following Section 2.2. Then,

in the next Chapter 4, HST archival data is explored together with the outcome of my data reduction.

- ACS. Installed in 2002, it is a third-generation imager, with the wavelength coverage ∼200-1100 nm. ACS hosts three independent channels: the High-Resolution Channel (HRC), the Solar Blind Channel (SBC), and the Wide Field Channel (WFC). Among them, the data reduction is performed on images collected by ACS/WFC.

  - **ACS/WFC.** It has a FoV of 202×202 $arcsec^2$ and a great resolution, with a pixel scale of $\sim 0.05 \times 0.05$ $arcsec^2/pixel$. It consists of two CCDs, manufactured by SITe, for a total size of 4096×4096 $pixels$. The range of sensitivity corresponds to wavelengths between ∼350 nm and ∼1100 nm.

    Among the available filters, in this Chapter 2 and in the following Chapter 3, respectively, I reduced the data obtained in the B filter **F475W** (λ_{min}∼380 nm, λ_{max}∼550 nm) and I presented some resulting photometric diagrams.

    Then, in Chapter 4, I analyzed images collected using the broad V filter **F606W** (λ_{min}∼462 nm, λ_{max}∼718 nm) and the broad I filter **F814W** (λ_{min}∼687 nm, λ_{max}∼963 nm), with also the additional contribution of data in the filter F475W just reduced.

- WFC3. The instrument was installed in 2009, and it is a fourth-generation imager, which covers the broad range of wavelengths ∼200-1700 nm. It encorporates two channels, enabling WFC3 to observe in the optical-UV range (WFC3/UVIS) and in the NIR regime (WFC3/NIR). Through the thesis some IR images acquired by WFC3/NIR are been analyzed.

  - **WFC3/NIR.** It has a smaller FoV, 136×123 $arcsec^2$, and lower resolution compared to ACS/WFC, with a pixel scale of 0.13×0.13 $arcsec^2/pixel$. The CCD is made of HgCdTe and consists of 1024×1024 $pixels$, even though only 1014×1014 $pixels$ are active. It has an excellent sensitivity to photons in the range ∼800-1700 nm.

    Among the available filters, the examined images were acquired through the three wide filters **F110W** (λ_{min}∼883 nm, λ_{max}∼1412 nm), **F140W** (λ_{min}∼1180 nm, λ_{max}∼1600 nm), and **F160W** (λ_{min}∼1385 nm, λ_{max}∼1700 nm).

2.2 Data set

In this Chapter of the thesis, the derived 47 Tuc photometric catalog results from archival images obtained in the F475W filter from the ACS/WFC instrument on board HST. The most relevant properties of the examined exposures (fits files) are illustrated in Table 2.1. These data sets are sampling the region within ∼2

arcmin from the coordinates RA$\sim 00^h22^m25.7^s$ and DEC$\sim -72^h04^m26.27^s$ observed by HST. The field studied by the indicated programs is positioned approximately 7 arcmin westward from the cluster center, as depicted in Figure 2.1, corresponding to $\sim$2 half-light radii. To determine stellar fluxes and positions, I utilized the flat-field calibrated images that had been corrected for the sup-optimal charge-transfer efficiency (CTE) of ACS/WFC as in Anderson & Bedin (2010) (flc images). The photometric calibration is conducted by employing the drizzle CTE-corrected (drc) images.

Image ID	Date	Exp. Time (s)	Instrument	Program	PI
jbva01n2q	02/12/11	339	ACS/WFC	12734	N.Grogin
jbva02ktq	20/03/12	339	ACS/WFC	12734	N.Grogin
jbva03jeq	17/07/12	339	ACS/WFC	12734	N.Grogin
jc5001sfq	01/11/12	339	ACS/WFC	13159	N.Grogin
jc5002onq	13/03/13	339	ACS/WFC	13159	N.Grogin
jc5003frq	29/06/13	339	ACS/WFC	13159	N.Grogin
jce501efq	22/11/13	339	ACS/WFC	13596	D.Coe
jce502hqq	04/03/14	339	ACS/WFC	13596	D.Coe
jce503bmq	07/07/14	339	ACS/WFC	13596	D.Coe
jcr513hmq	30/11/14	339	ACS/WFC	13959	D.Coe
jcr514lfq	31/03/15	339	ACS/WFC	13959	D.Coe
jcr515d5q	20/07/15	339	ACS/WFC	13959	D.Coe
jd0q13l1q	03/11/15	339	ACS/WFC	14402	D.Coe
jd0q14cyq	04/03/16	339	ACS/WFC	14402	D.Coe
jd0q15i1q	02/08/16	339	ACS/WFC	14402	D.Coe
jd5701siq	09/11/16	339	ACS/WFC	14511	D.Coe
jd5702kgq	07/03/17	339	ACS/WFC	14511	D.Coe
jd5703jfq	11/07/17	339	ACS/WFC	14511	D.Coe
jdfw01bwq	24/11/17	339	ACS/WFC	14953	D.Coe
jdfw02msq	17/03/18	339	ACS/WFC	14953	D.Coe
jdfw03buq	16/07/18	339	ACS/WFC	14953	D.Coe
jduo01peq	01/11/18	339	ACS/WFC	15526	A.Bellini
jduo04lrq	13/08/19	339	ACS/WFC	15526	A.Bellini
je6401qdq	06/11/19	339	ACS/WFC	15764	N.Hathi
je6403e4q	20/04/20	339	ACS/WFC	15764	N.Hathi
jee301amq	23/11/20	337	ACS/WFC	16384	Y.Cohen
jee303p4q	05/05/21	339	ACS/WFC	16384	Y.Cohen
jelq01t0q	06/02/22	337	ACS/WFC	16520	N.Hathi
jelq03teq	02/06/22	339	ACS/WFC	16520	N.Hathi
jezz01l8q	11/11/22	337	ACS/WFC	16968	N.Hathi
jezz03zgq	30/04/23	339	ACS/WFC	16968	N.Hathi

Table 2.1: Description of the HST images of 47 Tuc on which I employed data reduction in this Chapter of the thesis.

Figure 2.1: Footprint of the HST images in the filter F475W reduced in the work on 47 Tuc. North is up and east is left. The region indicated in orange corresponds to the coordinates given in Section 2.2, associated to the external cluster region studied by ACS/WFC.

2.3 Data reduction

This Section is dedicated to the procedure employed to create the stellar photometric catalog for the GC 47 Tuc. In practice, data reduction is performed applying to the images in the filter F475W several FORTRAN programs, all developed by J. Anderson.

First of all, a preliminary operation was considered. The archival images collected by ACS/WFC for HST are obtained from two separated rectangular CCDs. Therefore, it was necessary to align the images taken by the two chips: the task is achieved applying the FORTRAN program `flt2wj2`.

2.3.1 Deriving the effective PSF for 47 Tuc

Considering that I wanted to study the phenomenon of MPs below the MS knee (where the stars become fainter and fainter), it was necessary to produce accurate measurements of the fluxes and the positions of the stars in the cluster. The purpose is achieved deriving a precise Point Spread Function (PSF) model, to fit the pixels array that compose each image. Indeed, processed by the telescope, the distribution of the light from a star on the CCD can be reproduced by a PSF model. The procedure of finding the proper model presents important challenges inside crowded environments such as a cluster or even the Galactic bulge. Anderson and collaborators developed computer programs which employ distinct methods to measure stars. Method I, optimal for bright stars, derives stellar magnitudes and positions

by finding and then fitting the best available effective PSF model (see e.g. Anderson & King, 2000). Working with a 5×5 pixel matrix, the method represents a reasonable technique for crowded regions, in order to get precise photometry on each single star. The quantities are computed in each image, separately; then, it is derived their average, to improve the determination of both magnitudes and positions. A II and III method are instead used to obtain astrometry and photometry of faint sources, and they consist in the procedure of aperture photometry.

To achieve the task, I followed the same methodology described by Milone and collaborators (e.g. Milone et al., 2023a,b). The essential issue refers to the selection of the most appropriate and precise PSF model to best fit stellar profiles, which requires the knowledge of the star's position. At the same time, without information about the PSF, we can not measure positions and fluxes. In order to overcome the presented degeneracy, several steps are performed through an iterative procedure, applying the FORTRAN program `img2psf` to the exposures taken by ACS/WFC in the filter F475W. The routine is specifically developed for processing images from the selected detector. The program consists in the following steps:

1. It is first considered an archival PSF model, which is based on the CCD and filter properties, rather than constructing it on the actual image. By means of this library model is obtained a first guess on which PSF better fits stellar profiles.

2. Then, the library PSF is utilized to derive a more accurate PSF model. This second model is based on the actual image.

3. The program converges to the definitive good model: fitting the derived PSF model to the stellar profiles provides the measurement of position and flux of the detected sources.

The approach is a reliable one, as it iterates the fitting procedure improving the measurements and the fitting itself, as it proceeds. More specifically, the stars on which the process is performed are bright, not-saturated and quite isolated, in order to avoid crowded regions and to obtain a quite robust signal for characterizing the PSF.

To properly derive the PSF model, the routine requests several conditions, specified by 7 parameters:

- **HMIN.** It consists in the separation index, giving (in pixels) the minimum distance between two sources in order to be considered. The value used is 13.

- **FMIN.** It defines the minimum flux set for stars to be considered. It is a compromise choice, because it is required a huge number of stars for the PSF sampling, but the fainter they are and the higher the associated noise. In this case, it is used the value 5000.

- **PMAX.** It defines the maximum count value of flux for a source to be considered. The purpose is to exclude saturated stars. It is chosen the value 54,000, which is below the saturation limit.

- **QMAX.** It defines the maximum value of the Q parameter, indicative of the quality of the fit. A high value could indicate that the fitted source is probably not a star. The procedure required the optimized value of 0.25.

- **NSIDEs.** It indicates the grid sampling for the PSF, and it ranges from 1 to 5. Again, it is a compromise choice: selecting many regions, could allow to map the faint spatial variations of the PSF, however, it decreases the number of stars used to create the PSF. It strongly depends on the temperature of the telescope, and it should be accounted for, locally. The value used it 3, to produce a 3×3 grid, for all the analyzed images.

- **PSFFILE.** It is selected the archival PSF model to build the first-guess PSF model.

- **IMG.fits.** It defines the image on which the program determines the PSF model.

The PSF shape across the CCD could be affected by position-dependent effects, like charge diffusion and optical aberrations, leading to a substantial change. For this reason, in order to derive the catalog, the software computes the output *_PSF.fits* which includes a grid of 9×10 PSFs, rather than a single PSF model, built upon the actual image. This is done for each image that is reduced through data reduction. Through the grid of PSF models, it is improved the measurement of both position and flux of each source in every image. An example is shown in Figure 2.2.

The next step consists in applying the obtained PSF models to each image in the filter F475W, in order to measure the position and magnitude of every detected source. The procedure is carried out by another FORTRAN routine, `img2xym` (Anderson & King, 2006). The program operates after having set some conditions, similarly to the previous step. However, this time the parameters are less restrictive than before, especially since the PSF models are employed for all the stars, from the bright and saturated to the fainest ones. The input values are: HMIN = 5 (non-isolated stars are included), FMIN = 50 (too faint stars are not required), PMAX = 10^9, (saturated stars are taken into account). In addition, it is specified the PSF file and the image for which the measurements are needed. Unlike in the `img2psf` step, where all the images were treated with the same PSF model, here each image is provided with its proper PSF model computed by `img2psf`.

The main output of `img2xym` routine is a file with .xym extension, which contains, for each detected source, the coordinates, the instrumental magnitude, and the Q fit parameter. The latter value expresses the quality of the performed PSF fit: Q fit exhibits a clearly defined correlation with the magnitude, and it is crucial to differentiate between authentic stars and other sources. The Q fit ranges from zero, for precision photometry, to 1.

Figure 2.2: An example of the 9×10 grid of PSF models obtained through `img2psf` for one image taken by ACS/WFC in the filter F475W.

To identify sources associated with poor photometry, based on the Q fit, I used a technique illustrated in Figure 2.3. Given that the Q fit inferred from F475W photometry of the cluster depends on the F475W instrumental magnitude, I selected by eye the red curve in the figure. This line allows to disentangle between well-measured stars (lying below the line) and the clear outliers (above it). Mostly, the latter points are found around $m_{\rm F475W}\sim$ -8.5. The procedure described here is applied to each image in the F475W filter.

2.4 Photometric catalog

At this point of data reduction, it is derived a single photometric catalog containing the information from all the filters studied for 47 Tuc. This is carried out through several steps, which briefly consist in finding the proper coordinate transformation to apply to all the images, in order to refer each of them to a common reference frame. The following three routines by Jay Anderson implement this transformation and build the final reference catalog.

1. `xym2mat`. The first FORTRAN routine is required to align the images and bring them into the same reference frame. It computes the linear transformations for the position, to bring each image to the reference image, called the master frame. In principle, it identifies common stars, searching for similar triangles between the stars identified in two images. Through rotation and translation of the triangles, the images eventually coincide. This is known as the *Cross Identification* procedure.
   For the images to be processed, the `xym2mat` program requires to create a file. In such a file I specified which image to use as the master frame, the images

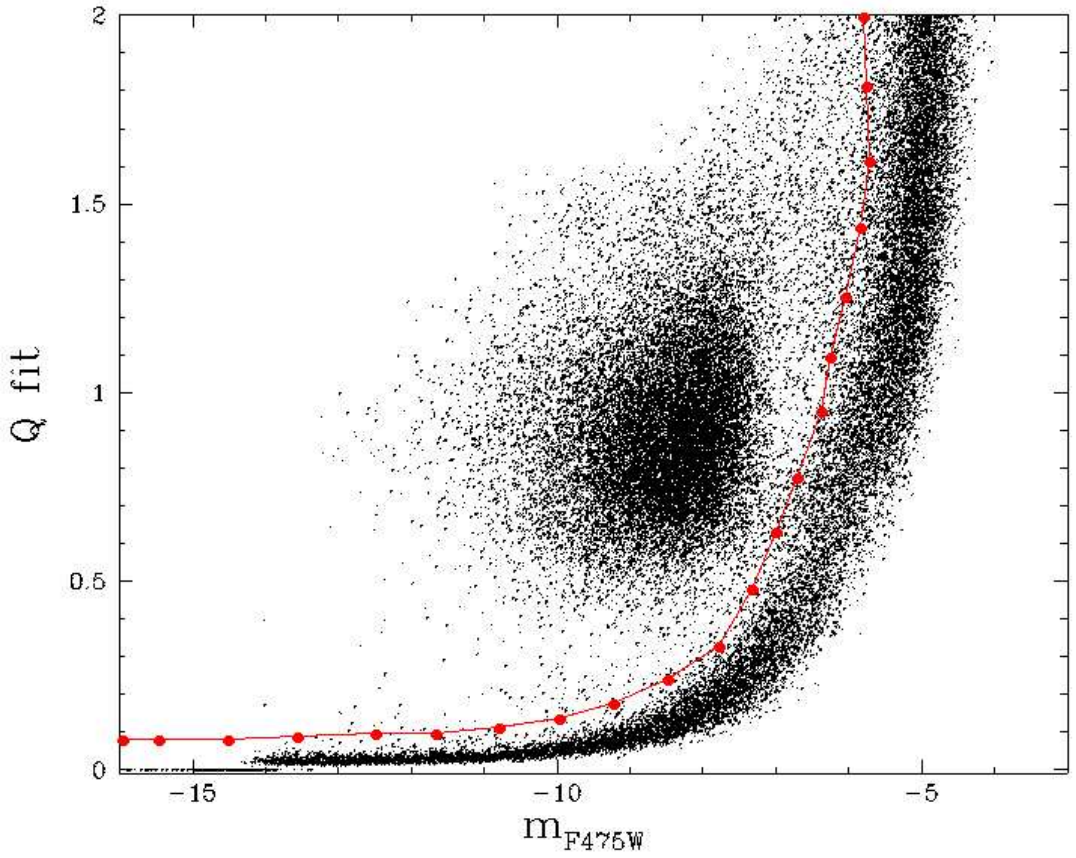

Figure 2.3: It is shown the dependence of Q fit parameter on the magnitude. The image illustrates the selection of high-quality photometric measurements in one frame taken in F475W. The red line with dots enables to disentangle the poorly-measured sources (above it) from the well-measured ones (below the line).

to be brought in the selected frame, as well as three other parameters. Two of them indicate which CCD and filter have been employed for the observation, in order to correct for the effect of geometric distortions associated to the filter, a step to accomplish before the cross-identification. The last value gives information about the magnitude interval used for the research of similar triangles, which is between -13.5 and -11.0 magnitude. After having created the file, it is requested an input parameter, expressing the distance (in pixels) for two stars to be considered as distinct sources. I selected the value 0.45 pixels.
The output is collected in one file for each image, containing the computed transformations: pairs of coordinates and magnitude for similar stars. To confirm whether the procedure was successful or not, one test is to plot the residuals in position, given as output of the transformation. In Figure 2.4 is shown what is obtained for one image. It is observed the distribution of the difference in position between a star in one image and the same star in the reference frame, after the procedure. We should expect a small scatter of the residuals around zero (due to observational errors), which would indicate that a successful work has been done. Clearly, this is the case for the image shown in figure. Otherwise, the residuals for the position would be randomly distributed, without being clustered around zero or just being clustered somewhere distant from the center. The test is executed for each image, to properly ensure that the transformations were successful.

2. `xym2bar`. This second step is employed to generate a single stellar catalog for the filter F475W. Starting from the output files of `xym2mat`, the FORTRAN program `xym2bar` computes the magnitude of each detected star, as a sigma-clipping mean value of the magnitudes of distinct images. Analogously, it is calculated the average of the distortion-corrected coordinates found in different images for each source. It is requested a file similar to that required by the previous routine. However, this time I do not select non-saturated stars alone, but I rather extend the magnitude range, in order to include and measure all the stars. It is taken into account the magnitude interval between -99 and -5. There is an input parameter to be given to the program: it is NIMMIN, indicating which is the minimum number of images where a star should be found by the routine, to consider it in the final catalog. It is used the value of 5.
The program creates an output file that contains information on the position, magnitude, together with the relative errors, for each of the selected stars encompassed in the preceding steps.

3. `xym1mat`. This third FORTRAN program is fundamental, in order to build a photometric catalog with information from all the different filters available. More specifically, adopting a reference catalog, used as the master, the program identifies the stars in common with other catalogs, assigning to them the values of magnitudes in different filters.
It is established an association bewteen the HST photometry and the astrometry and photometry of Gaia DR3. The Gaia catalog referred to the magnitudes

in F606W and F814W, containing a higher number of stars, is selected as the reference catalog. More details on this reference frame are provided in the next Section 2.5. Similarly to `xym2mat`, by using six-parameter linear transformations, the software searches for similar triangles, bringing the information for a certain star found in the matching catalog, to the corresponding line of the output file. The task is achieved by setting 7 arguments:

- the first star list: the reference catalog, Gaia, used as the master.
- the second star list: the HST file to match, which is the output file from the previous routine.
- A first output file: it is a file with .mat extension, where the program stores the coordinates of similar stars, aligning them.
- A second output file: it has .xym1 extension, and it is not exactly relevant for the following analysis.
- A third output file: it represents the link-up file, which has the same dimension as the masterframe (Gaia). This file stores the information extracted, for every star, from the matching file (HST), after having created the link between the stars.
- NITREJ: the number of rejection iterations to perform, before getting a consistent determination. Considering that, reasonably, the system converges after a high number of iterations, it is selected the value 21.
- DMINU: the value (in pixels) of coordinate difference to select, between a star in the masterframe and the same star in the other catalog, in order to consider the star. This is referred to the pixel distance computed after having linked the catalogs. It is used the value of 10 pixels.

The program generates a file where the stars in the two catalogs are associated, which has identical dimension as the Gaia original catalog. Mostly, the procedure aims to properly orient the final catalog. In fact, the obtained orientation is unambiguous, and it corresponds to the projection of the tangential plane of right ascension (RA) and declination (DEC). The catalog in output includes positions and magnitudes in F606W and F814W measured by Gaia, and the magnitude values in the filter F475W obtained by HST.

The methodology described above allowed to produce the final masterframe. In practice, the output of the `xym1mat` routine, being a distortion-free catalog obtained from the distortion-free coordinates by Gaia, is set as the new reference frame to perform again `xym2mat` and `xym2bar`. Ultimately, it is extracted the new final catalog, oriented as the previous Gaia catalog.

Then, to extend the dataset, the last software presented in the paragraph (`xym1mat`) is applied to the IR filters F110W, F140W and F160W. Through this procedure, the catalogs are aligned to each others, taking in to account the final master as the reference frame.

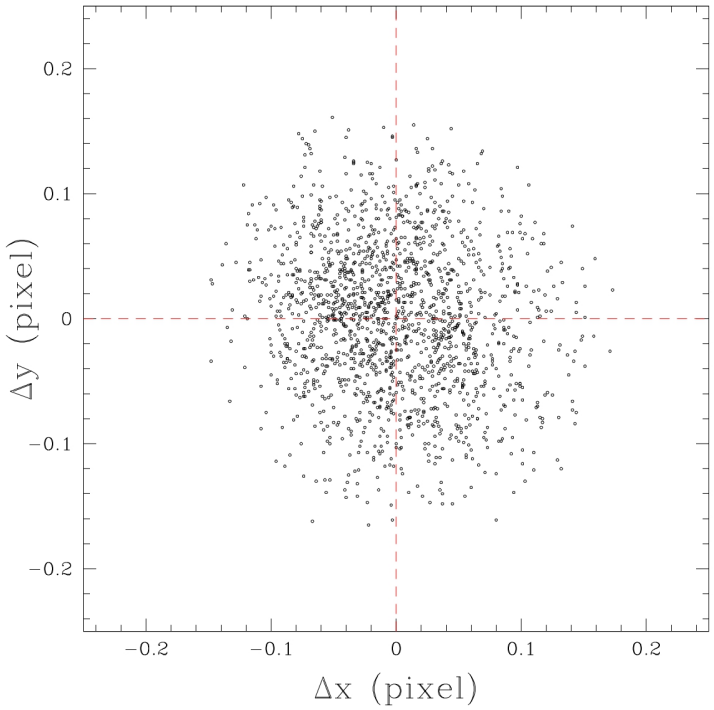

Figure 2.4: It is shown the difference in position, after `xym2mat`, between stars in the master frame and in one of the exposures obtained in the filter F475W, which I brought into the master reference frame. This is an example of a successful transformation, as the residuals are distributed around the center.

2.5 Gaia reference frame

The starting HST photometric catalogs, for the previous Section, are referred to an arbitrary reference frame, provided by one image collected by HST in the filter F475W. As the stellar positions are those of the CCD, I moved to the Gaia reference frame. First and foremost, I downloaded the catalog for 47 Tuc from GAIA Data Release 3 (DR3, Gaia Collaboration et al., 2022)[1]. The coordinates of DR3 data are given in RA and DEC; consequently, they need to be converted into linear coordinates, which are the coordinates of the CCD frame. Through the procedure declared in the last part of the previous Section, it is derived the final match.

Now, it has been obtained a stellar catalog provided with Gaia coordinates and HST instrumental magnitudes in the filter F475W.

2.6 Calibration

The last step is needed to calibrate the instrumental magnitudes m_{inst} into the Vega reference system. The outcome is expressed as calibrated magnitudes m_{cal}, through the formula

$$m_{cal} = m_{inst} + \Delta mag + ZP_{filter} + C, \tag{2.1}$$

[1]The data are available on the website `https://gea.esac.esa.int/archive/`.

where Δmag is the difference between the PSF magnitude (i.e. the magnitude obtained in Section 2.3) and that one derived through aperture photometry (which I will discuss in this section), ZP_{filter} is the zero-point correction for a given filter, while C is the aperture correction. The zero-point value for the F475W filter of ACS/WFC is retrieved from an online utility[2], setting the proper date of observation and the filter and instrument selected. A different online catalog[3] is used to obtain the aperture correction value, after having selected the aperture of 0.5 arcsec.

First, to calculate Δmag, I performed aperture photometry on the drizzled images (files in drc format), through the FORTRAN program `drz_phot_gfortran`. The software works on exposures taken with an unitary exposure time, implying that the counts per pixel corresponds to the number of counts per unit second. Several arguments are requested by the program: the minimum distance between two sources to include them in the analysis (HMIN=10), minimum and maximum flux (FMIN=0.1 and PMAX=9999), in addition to the image to be taken into account. Other parameters concerning the aperture radius, as well as the inner and outer radius of a ring, destined to measure the sky level, are also specified. For the latter three arguments I selected 10.1 pixels (associated to an aperture of about 0.5 arcsec), 14 pixels for the inner radius (0.7 arcsec) and 20 pixels for the outer radius (1 arcsec) of the sky annulus. The studied aperture results from a compromise choice, as I would like to collect as much stellar flux as possible, but at the same time it is crucial to minimize the contamination from nearby stars. In output are obtained files with .xym extension, containing positions and magnitudes for the stars.

The second step aims to link these files to the corresponding stellar catalog (derived with PSF photometry), through `xym1mat`. Through the procedure already described, I search for the six-parameter linear transformations required to pass to the final reference system, analyzing first the brightest stars, and then all of them.

Eventually, Δmag is computed using a suitable algorithm, which calculates the difference between stellar magnitudes obtained via PSF photometry and aperture photometry, and then determines the median of these differences. The program iterates, considering only the brightest and better-measured stars, converging to the final result. The procedure is applied to the magnitude range which comprises stars between -13.75 (non-saturated stars) and -12.75 (bright enough to be considered).

Last, I could calibrate the instrumental magnitude, adding the Δmag for the filter F475W, thus deriving the physical quantity of m_{cal}. It is on the final calibrated magnitude that I focused to produce the scientific results that are presented in the next chapters.

[2]https://acszeropoints.stsci.edu/

[3]https://www.stsci.edu/hst/instrumentation/acs/data-analysis/aperture-corrections

Chapter 3

The target: 47 Tucanae

The Chapter introduces the research target, namely 47 Tucanae. Some results are presented in Section 3.4, after having performed data reduction in the filter F475W, as described in details in the previous Chapter 2.

3.1 Literature studies on 47 Tuc

47 Tucanae (47 Tuc, NGC 104) is the second-brightest GC in the MW, appearing near the SMC in the sky. It is an old cluster, with the estimated age ranging from ∼10 to ∼13 Gyrs (Forbes & Bridges, 2010), a mass of $\sim(7.79\pm0.05)\times10^5\ M_\odot$ (Baumgardt & Hilker, 2018) and a very low extinction of $E(B-V)$=0.04±0.02 (Salaris et al., 2007). For a general presentation of the main structure parameters of the cluster, refer to Table 3.1.

In the context of MPs, this GC is one of the most-studied, through spectroscopy, photometry and kinematics (e.g. Anderson et al., 2009; Di Criscienzo et al., 2010; Carretta et al., 2013a; Richer et al., 2013; Cordero et al., 2014; Milone et al., 2018a; Cordoni et al., 2020; Milone & Marino, 2022). Indeed, since the seventies, it has been strongly investigated, addressing the issue of chemical inhomogeneities responsible for producing multiple sequences detected on RGB stars (e.g. Dickens et al., 1979; Bell et al., 1983; Brown et al., 1990; Briley et al., 1991). The present-day picture confirms that 47 Tuc harbors discrete stellar populations belonging to 1P and 2P, as derived from ChMs along many distinct evolutionary phases, like MS, SGB, RGB, HB, and AGB (e.g. Milone et al., 2012a; Lagioia et al., 2021; Jang et al., 2022; Tailo et al., 2020; Lee, 2022). In particular, the exploration of the ChM reveals at least three groups of 2P stars, corresponding to variations in the content of light-elements (Milone et al., 2017a, 2023a; Marino et al., 2019). Especially, a further characterization of 2P is available, and indicates abundances intervals of ∼0.4 dex in [C/Fe], ∼1.0 dex in [N/Fe], ∼0.5 dex in [O/Fe] (the values are referred to Carretta et al., 2009; Marino et al., 2016; Dobrovolskas et al., 2014), whereas He spans an interval of δY=0.05 in mass fraction (Milone et al., 2018b). Conversely, 1P stars cover a broad portion of the ChM, associated to Fe content fluctuation given by [Fe/H]∼0.09 dex (Milone et al., 2018b; Legnardi et al., 2022; Jang et al., 2022). Basically, the classification of the populations provided so far in the paragraph is the one used in the next Chapter 4, for data analysis. Further details are found in the chapter.

Exploring the target GC is fundamental to investigate MPs and extend the search of the already-known properties of similar MW clusters. Moreover, the selected HST field represents an ideal one (details are provided in Section 2.2). In fact, 47 Tuc is a dynamically young GC, implying that the initial condition of its stars has been preserved, mostly. The GC stars are not mixed yet, especially toward the outskirts. An external region, like the HST field analyzed in this research, keeps this information and allows to observe and deepen the comprehension of MPs' features. I would have encountered a quite different configuration looking at any internal cluster region, where instead it is expected to find a relaxed stellar configuration.

RA (J2000)	00h24m05.36	`https://ned.ipac.caltech.edu/`
DEC (J2000)	-72d04m53.20s	`https://ned.ipac.caltech.edu/`
Age [Gyr]	10-13	Forbes & Bridges (2010)
Mass [$M_\odot$]	$(7.79\pm0.05)\times10^5$	Baumgardt & Hilker (2018)
Distance [kpc]	4.41	Baumgardt & Hilker (2018)
r_h [kpc]	3.57	Baumgardt & Hilker (2018)
r_c [kpc]	0.49	Baumgardt & Hilker (2018)
E(B-V)	0.04±0.02	Salaris et al. (2007)

Table 3.1: Main characteristics of 47 Tuc, based on literature papers. The reported distance measurements are, following this order, the heliocentric distance, the half-light radius and the core radius (all three taken from Baumgardt & Hilker, 2018).

3.2 Photometry of 47 Tuc

Broad sequences of 47 Tuc stars have been found throughout various successive stages of stellar evolution. Using the ($m_{\rm F275W} - m_{\rm F336W}$ vs $m_{\rm F336W} - m_{\rm F435W}$) two-color diagram, different distributions of stars can be clearly separated along the MS, SGB, RGB, and HB, which is visible in Figure 3.1, on the right (Milone et al., 2012c). This bimodal distribution of the populations is accompanied by a clustering of about ∼80% of the stars of each phase in the upper-right part of the diagram (referred to 2P stars), while ∼20% populates the lower-left region (1P distribution), which applies not in general but individually for the central field explored by Milone et al. (2012c). There are also indications of a decreasing radial trend for the 80/20 ratio for the populations. All the details on the split of each evolutionary stage into multiple sequences is captured by photometric diagrams like the ones presented in Figure 3.2. There, it is exploited the essential role of two filters, F275W and F336W, in simplifying a complex phenomenon.

I present the cluster also through the following Figure 3.3 and 3.4, taken from Milone et al. (2023a). The panels in Figure 3.3 show on the left the visual ($m_{\rm F814W}$ vs $m_{\rm F606W} - m_{\rm F814W}$) and on the right the NIR ($m_{\rm F814W}$ vs $m_{\rm F110W} - m_{\rm F160W}$) CMDs. In panel ($a$) are observed three stellar sequences: clearly, the reddest is populated by MS stars, and, increasing the magnitude, it can be followed continuously on the SGB, RGB, and RHB. The bluest sequence identifies the WDCS, whereas the stars on the middle sequence belong to the SMC. The broadening of the most populated sequence

is highlighted through the IR diagram presented in panel (b). Then, in panels (c) and (d) in Figure 3.4, both the previous CMDs are zoomed on the region of low-mass stars. Only cluster's stars are selected, based on their proper motions. These CMDs allow to reveal the MPs, as they exhibit the unique feature of a broadened MS, incompatible with the spread associated to the observational error. The sequences are seen partially superimposed (certainly parallel), on the optical diagram of panel (c). As regards the IR CMD of panel (d), it is worth mentioning that above the knee at $m_{\rm F814W}\sim$20.0 mag the spread of the stellar color is quite narrow, while below this level the sequence becomes larger.

As concerning the regime of low-mass stars, we are still lacking an extensive and thorough description of 47 Tuc M-dwarfs and brown-dwarfs. Constraining the properties of MPs among them represents a major challenge in stellar astrophysics, as already mentioned. Only one pivotal work, combining HST and JWST data, has been devoted to them: early results have been published by Marino et al. (2024), as described before. The authors present photometric diagrams that allow to validate the evidence of MPs among M-dwarfs indicated by the studies discussed in the former Chapter 1. Illustrative are the ($m_{\rm F322W2}$ vs $m_{\rm F150W2} - m_{\rm F322W2}$) and ($m_{\rm F322W2}$ vs $m_{\rm F115W} - m_{\rm F322W2}$) CMDs of Figure 3.5.

3.3 Population ratio

This section is devoted to the report of a result from Marino et al. (2024) which is of great relevance for the further analysis. Increasing the radial distance from the center of a cluster, the 2P/1P ratio varies. In particular, it is expected to decrease moving toward the cluster outskirts, where we are likely to observe a more populous 1P. The two populations are not equally represented in the sample analyzed through the thesis. Therefore, in order to achieve the research task, it is fundamental to consider the parameter of $R_{MS} = \frac{N_{MS,2P}}{N_{MS,1P}}$, expressing the ratio of MS 2P over 1P stars. To obtain the ratio for 47 Tuc, it is employed the procedure outlined by Zennaro et al. (2019). We define distinct regions on the ChM. Due to photometric errors, each one may encompass stars from all populations. The exact diagram to which I refer and the selected populations are presented in the next Chapter 4, Section 4.2. The counts in a certain region of the ChM are obtained taking the numbers of stars within each population, each one weighted by the fraction of stars of that population which are precisely grouped in that region, and summing up these values. To summarize the result, Marino and collaborators find that 1P comprises only 38.1±1.2% of the total of the stars within the ChM, within that field. The remaining percentage of ∼61.9% incorporates stars belonging to the 2P. As a consequence, it is estimated the value of $R_{MS} \backsimeq \frac{61.9}{38.1} = 1.62$.

The presented case surely should not be accounted for as a universal one, because the fraction of 2P stars (and consequently also the population ratio) is a function of the radial distance. Its value covers a broad interval, ranging from 80% near the cluster's innermost region to less than 60% at distances larger than ∼5 arcmin (Milone et al., 2012e, 2017a; Cordero et al., 2014; Dondoglio et al., 2021; Lee, 2022). There is agreement between the 2P fractions provided by Dondoglio et al. (2021) from HB stars at different radial distances, and those ones obtained from M-dwarfs

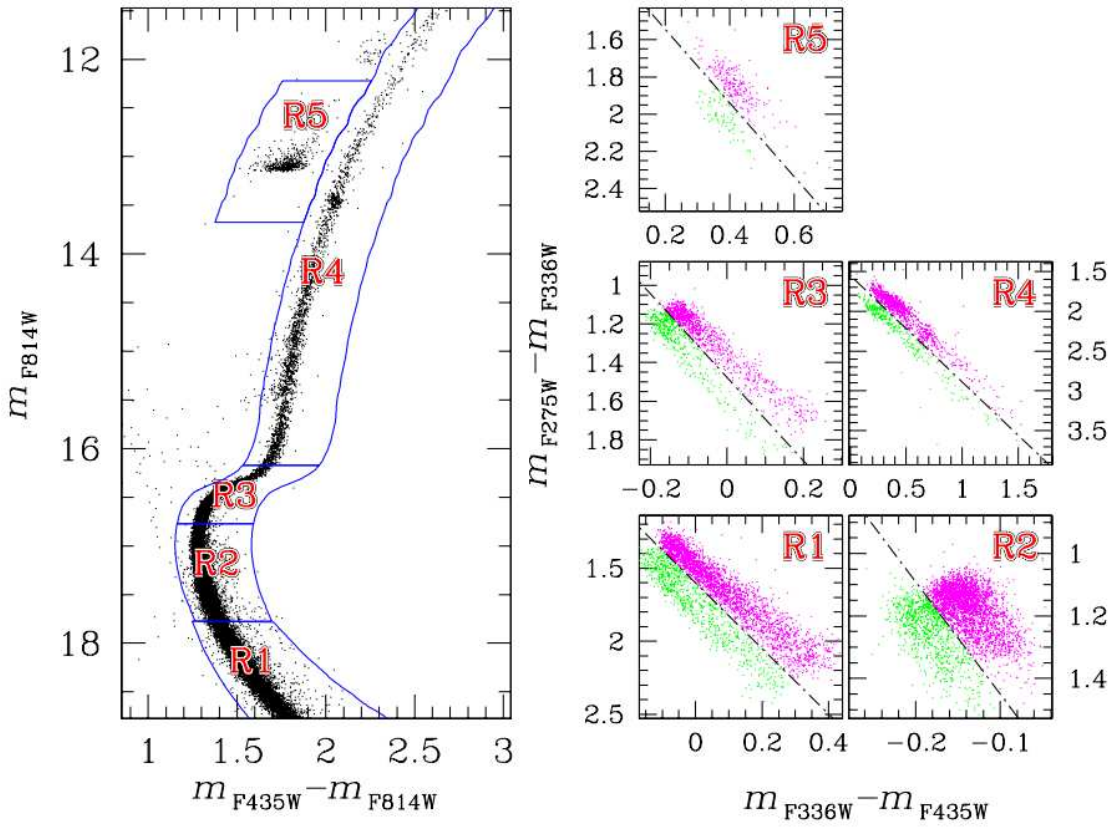

Figure 3.1: Some diagrams obtained from HST photometry of 47 Tuc: m_{F814W} vs $m_{F435W} - m_{F814W}$ CMD (on the left) and $m_{F275W} - m_{F336W}$ vs $m_{F336W} - m_{F435W}$ two-color diagram (on the right). The five selected regions R1, R2, R3, R4, and R5, respectively mark the MS, the turn-off region, the SGB, the RGB, and the HB. The dash-dotted lines indicate how the green stars, associated to 1P, are separated from the ones in magenta, representative of the chemically-anomalous 2P. Figure taken from Milone et al. (2012c).

by Marino et al. (2024), indicating that the value is independent on the evolutionary phase considered to make the inference. The outcome of these different samples are compared in Figure 3.6.

3.4 Results of data reduction in F475W

The method discussed in Chapter 2 enabled me to access the photometry of 47 Tuc in the blue filter F475W, that I combined with available data in order to produce photometric diagrams. Among them, I present hereafter the (m_{F475W} vs $m_{F475W} - m_{F606W}$) and the (m_{F475W} vs $m_{F475W} - m_{F814W}$) CMDs. On them I exploit possible combinations of optical filters with F475W.
First of all, in Figure 3.7, I show two raw diagrams, not corrected for proper motions, hosting all the stars within the observed FoV. Before the cleanup, the cluster members are not separated from foreground and background stars, which belong also to the SMC. The diagrams resemble the optical (m_{F814W} vs $m_{F606W} - m_{F814W}$) CMD presented in Figure 3.3, showcasing the three remarked sequences. More specifically,

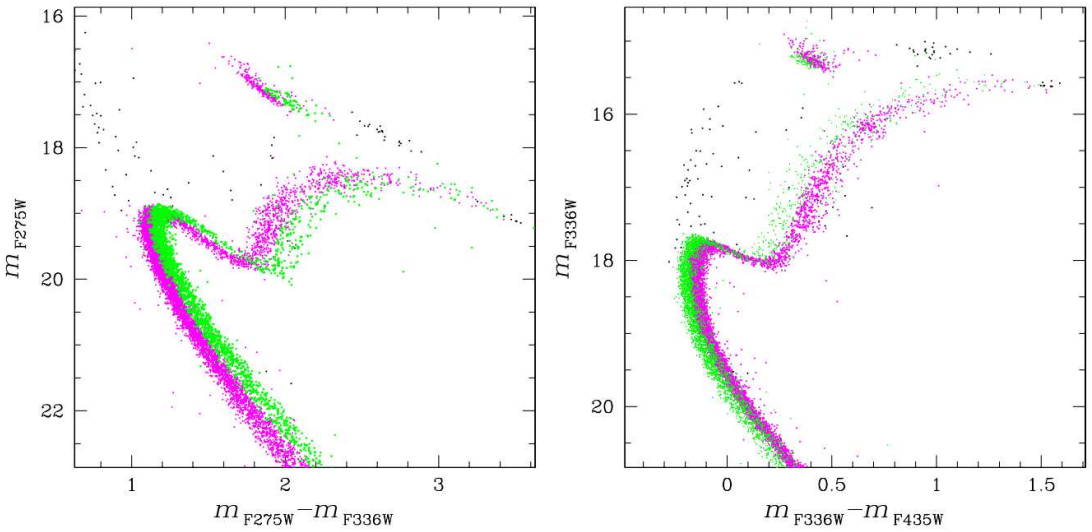

Figure 3.2: CMDs with $m_{\rm F275W}$ vs $m_{\rm F275W} - m_{\rm F336W}$ (left panel) and $m_{\rm F336W}$ vs $m_{\rm F336W} - m_{\rm F435W}$ (right panel). As in Figure 3.1, the two groups of stars are marked in green and magenta. From the MS to the HB, the two stellar populations can be followed in this striking representation of MPs. Taken from Milone et al. (2012c).

on top of the stellar sequences, the SMC is highlighted in red. Proper motions are inferred as in Milone et al. (2023a), averaging the positions from all the exposures taken at different epochs, to derive the displacements relative to the bulk of cluster stars. After this selection, my final sample is pure and includes only stars within the cluster.

As observable in Figure 3.8, the most highly populated sequence in the diagram can be followed continuously from the bottom, along the MS, through the SBG, up to the brightest extreme of the RGB. The sequence reaches the so-called MS knee at $m_{\rm F475W}\sim$23 mag, where the phenomenon of MPs among low mass stars becomes visible. In fact, toward fainter magnitudes, the sequence gets broader. A second sequence, to the left, at $(m_{\rm F475W} - m_{\rm F606W})<0.5$ mag, represents the WDCS.

Similarly, the CMD in Figure 3.9 shows two main stellar sequences: the more highly populated MS, on the right, and the fainter WDCS, on the left. In this case, the MS knee is approximately at $m_{\rm F475W}\sim$22 mag. From the comparison with the previous CMD, it is noticeable how the slope of the more populous sequence is affected by the colors choice: in fact, in Figure 3.8, the sequence is more vertical, whereas on this diagram it proceeds obliquely towards redder stars.

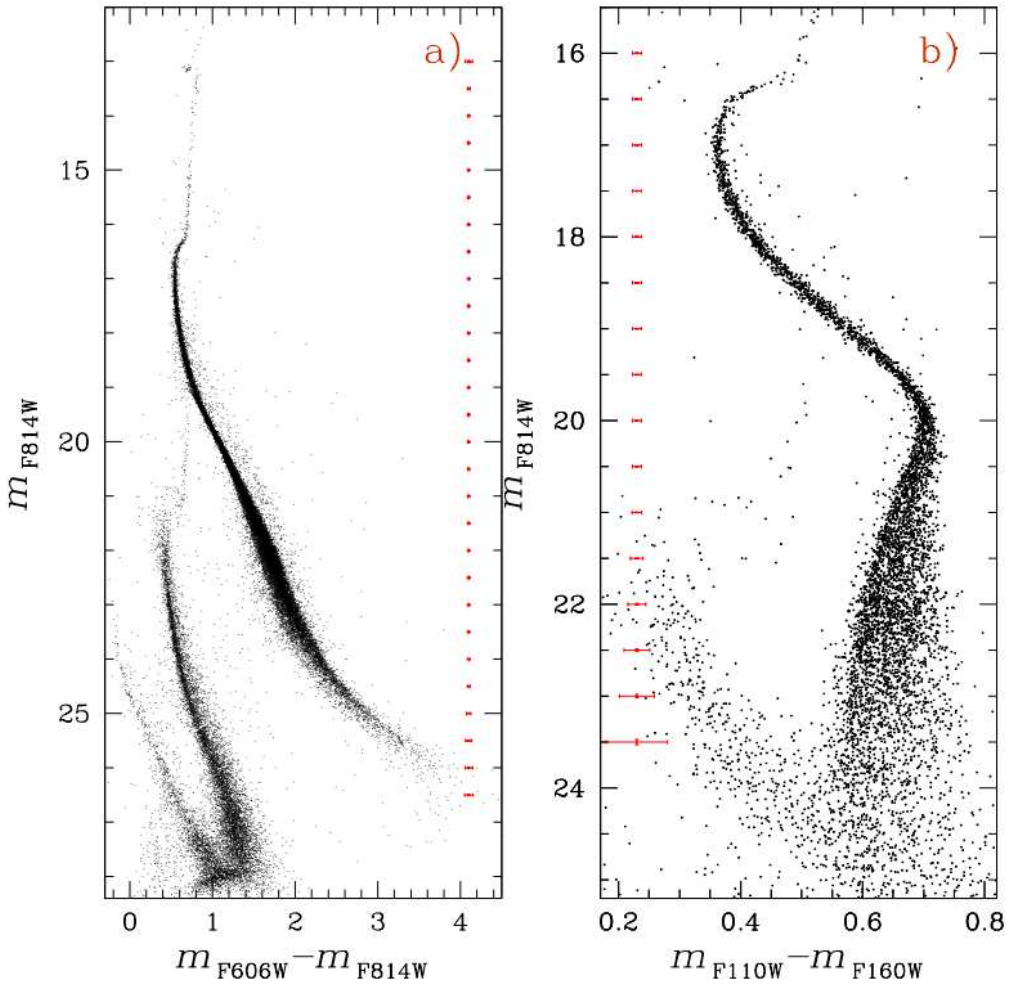

Figure 3.3: Optical $m_{\rm F814W}$ vs $m_{\rm F606W} - m_{\rm F814W}$ CMD on panel (a) and NIR $m_{\rm F814W}$ vs $m_{\rm F110W} - m_{\rm F160W}$ CMD on panel (b), from HST photometry. These two diagrams are useful for different purposes: the first one produces narrower sequences, the latter outlines a broadened distribution of stars below the MS knee (the region at $m_{\rm F814W} > 20.0$). The figure is taken from Milone et al. (2023a).

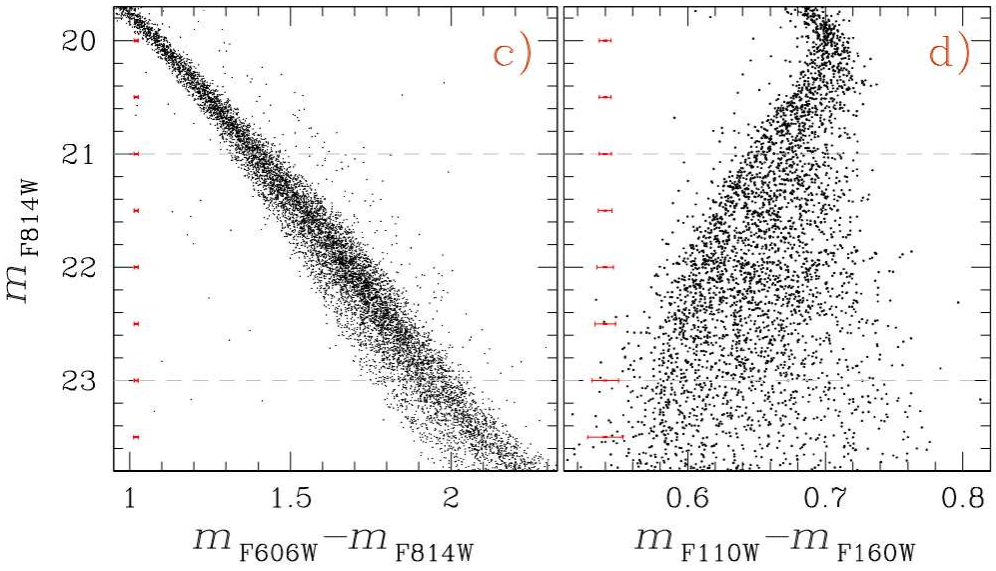

Figure 3.4: Same CMDs as in Figure 3.3, zoomed on the portion of the diagram where the cluster's MS members are being selected below the knee. These zoomed-in panels allow to appreciate the phenomenon of MPs, because both the diagrams are not consistent with a single population of stars. Details on the results of the analysis of such diagrams are provided in Section 3.2. The figure is taken from Milone et al. (2023a).

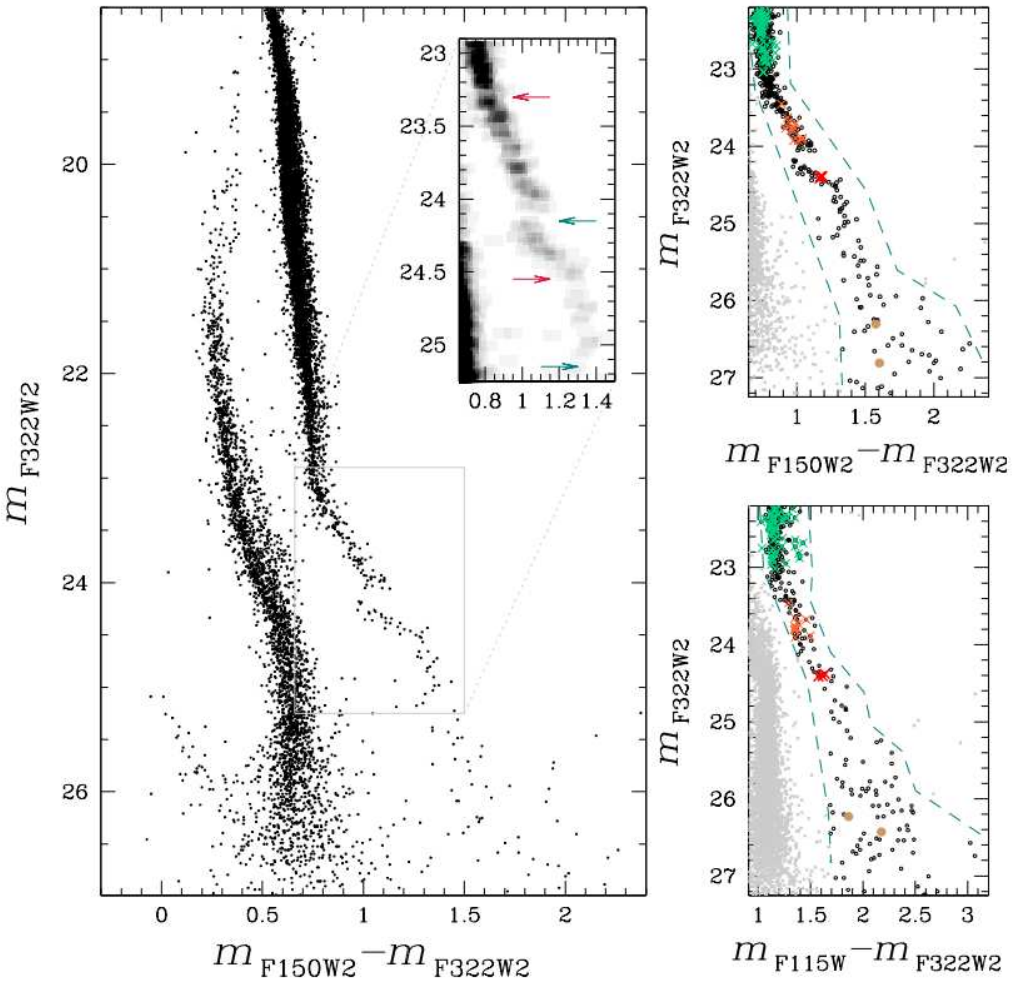

Figure 3.5: Diagrams investigating the low MS of 47 Tuc, from photometric data gathered with JWST. On the left: ($m_{\rm F322W2}$ vs $m_{\rm F150W2} - m_{\rm F322W2}$) CMD and the Hess diagram inset specifically show the low-mass stars. Gaps and discontinuities indicate, with the colored arrows, either a minimum in luminosity or a change in the distribution slope. On the right: $m_{\rm F322W2}$ vs $m_{\rm F150W2} - m_{\rm F322W2}$ (on the top) and $m_{\rm F322W2}$ vs $m_{\rm F115W} - m_{\rm F322W2}$ CMDs (on the bottom), for faint MS stars and brown-dwarfs. Image from Marino et al. (2024).

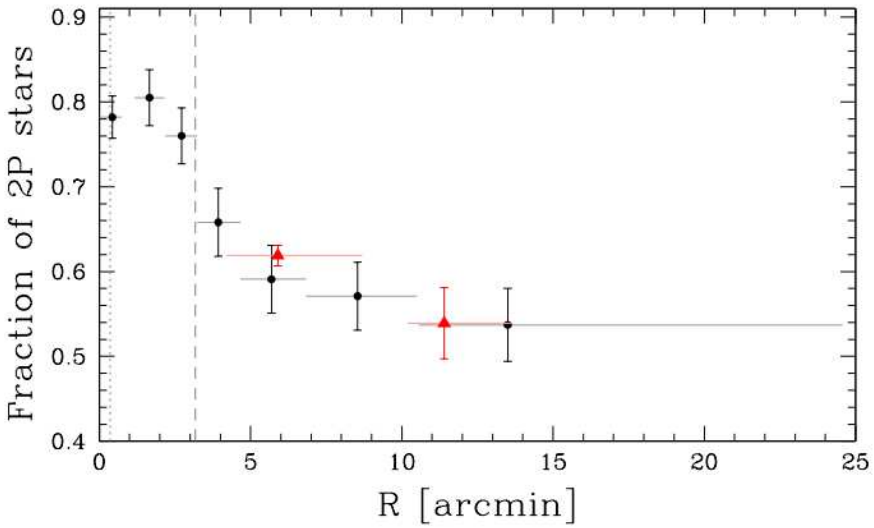

Figure 3.6: Fraction of 2P stars as function of the radial distance from the cluster center. Data obtained by Dondoglio et al. (2021) from HB stars (black dots) are compared with those derived by Marino et al. (2024) from M-dwarfs (red triangles). Taken from Marino et al. (2024).

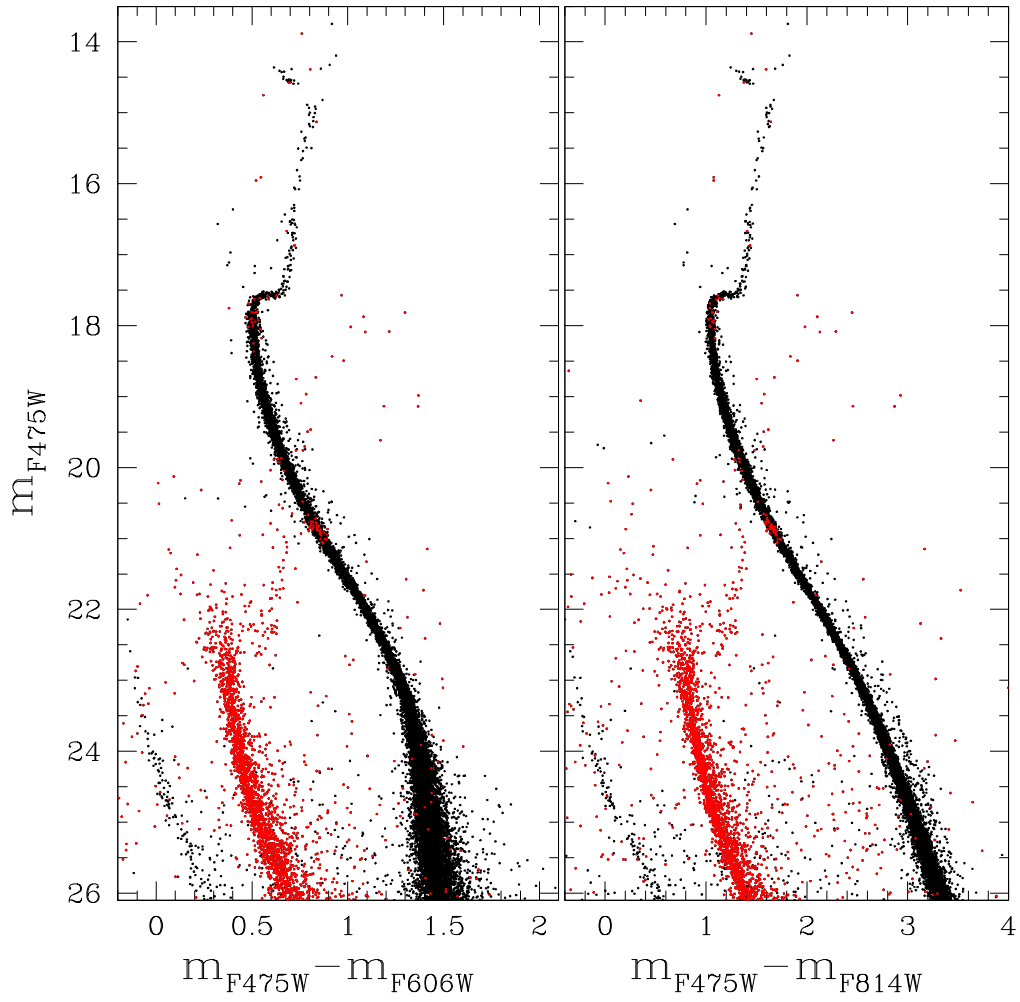

Figure 3.7: m_{F475W} vs $m_{\mathrm{F475W}} - m_{\mathrm{F606W}}$ and m_{F475W} vs $m_{\mathrm{F475W}} - m_{\mathrm{F814W}}$ CMDs of 47 Tuc and all the stars within the FoV. Background stars belonging to the SMC are marked in red, spatially far but encompassed by the same sky region.

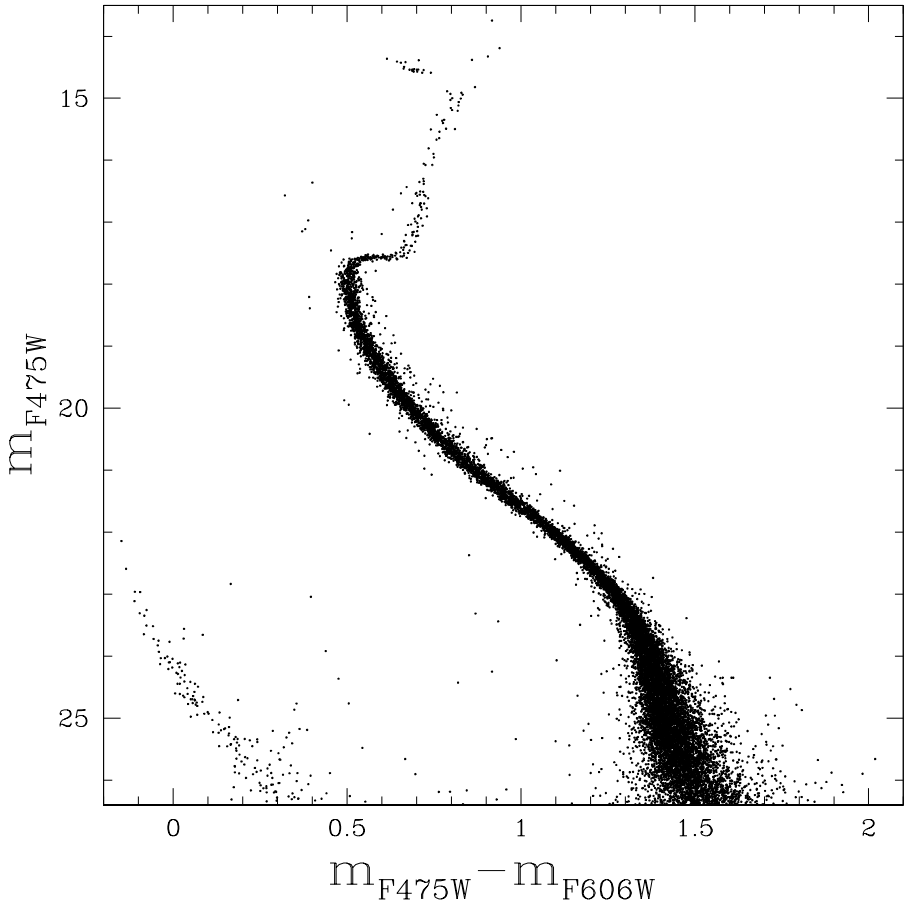

Figure 3.8: m_{F475W} vs $m_{\mathrm{F475W}} - m_{\mathrm{F606W}}$ clean CMD of 47 Tuc, obtained with a combination of filters that includes data reduced in the filter F475W. It contains only the cluster's stars, based on the proper motions.

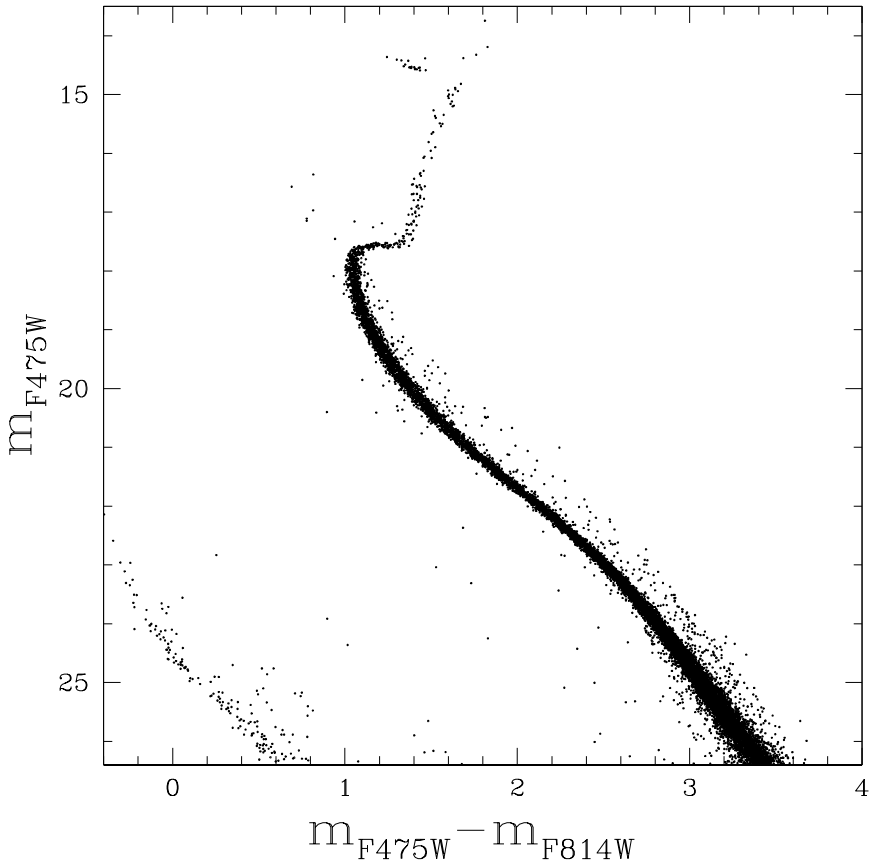

Figure 3.9: Similar to Figure 3.8, but referred to the $m_{\rm F475W}$ vs $m_{\rm F475W} - m_{\rm F814W}$ clean CMD of 47 Tuc.

Chapter 4

Data analysis and results

This Chapter is dedicated to the analysis of the photometric catalogs. The purpose is the identification and characterization of the MPs along the MS of 47 Tuc. In particular, I exploit multi-band photometry to estimate the fraction of binaries among first- and second-population stars fainter than the MS knee.

The data utilized here are archival observations, reduced through the procedure described in Chapter 2, developed by Milone et al. (2023a) and Marino et al. (2024).

This Chapter is organized as follows. Section 4.1 summarizes the photometric dataset, while the procedure to select the cluster's populations is illustrated in Section 4.2. The photometric binaries with large mass ratios are identified in Section 4.3, where we investigate their color and magnitude distributions. Finally, Section 4.4 illustrates the procedure to derive the incidence of binaries among the stellar populations of 47 Tucanae.

4.1 Data set

To investigate the incidence of binaries among the MPs of 47 Tucanae I combined the IR and optical photometry available from literature works, with those in the filter F475W explored in the previous chapters. Specifically, the literature dataset comprises photometry in the F110W, F140W and F160W bands of the WFC3/NIR channel on board HST and the F606W and F814W filters of ACS/WFC. Details on this dataset are provided by Milone et al. (2023a).

4.2 Selection of the populations

To identify the main stellar populations of 47 Tucanae, I use the pseudo-two color diagram dubbed chromosome map, which is a photometric tool designed to identify stellar populations with different chemical compositions. Specifically, I used the ($m_{\rm F814W}$ vs $m_{\rm F606W} - m_{\rm F814W}$) and the ($m_{\rm F814W}$ vs $m_{\rm F110W} - m_{\rm F160W}$) CMDs to derive the ChM illustrated in Figure 4.1 for M-dwarfs. This ChM reveals four main stellar populations that I identified through the approach described by Milone et al. (2023a). The 1P stars are clustered around the ChM origin and define the sequence of stars with $\Delta_{\rm F110W,F160W} \leq 0.03$ mag that I highlighted in red. 2P stars define an extended sequence that approaches extreme $\Delta_{\rm F110W,F160W}$ values and is composed of

stars that are depleted in oxygen with respect to 1P stars, which have [O/Fe]∼0.3. I identified three main sub-groups of 2P stars that I named 2Pa, 2Pb, and 2Pc and colored green, blue, and magenta, respectively. These stellar subpopulations exhibit different oxygen abundances with 2Pc stars having the most-extreme abundances of [O/Fe]∼ −0.1 dex (Marino et al., 2024).

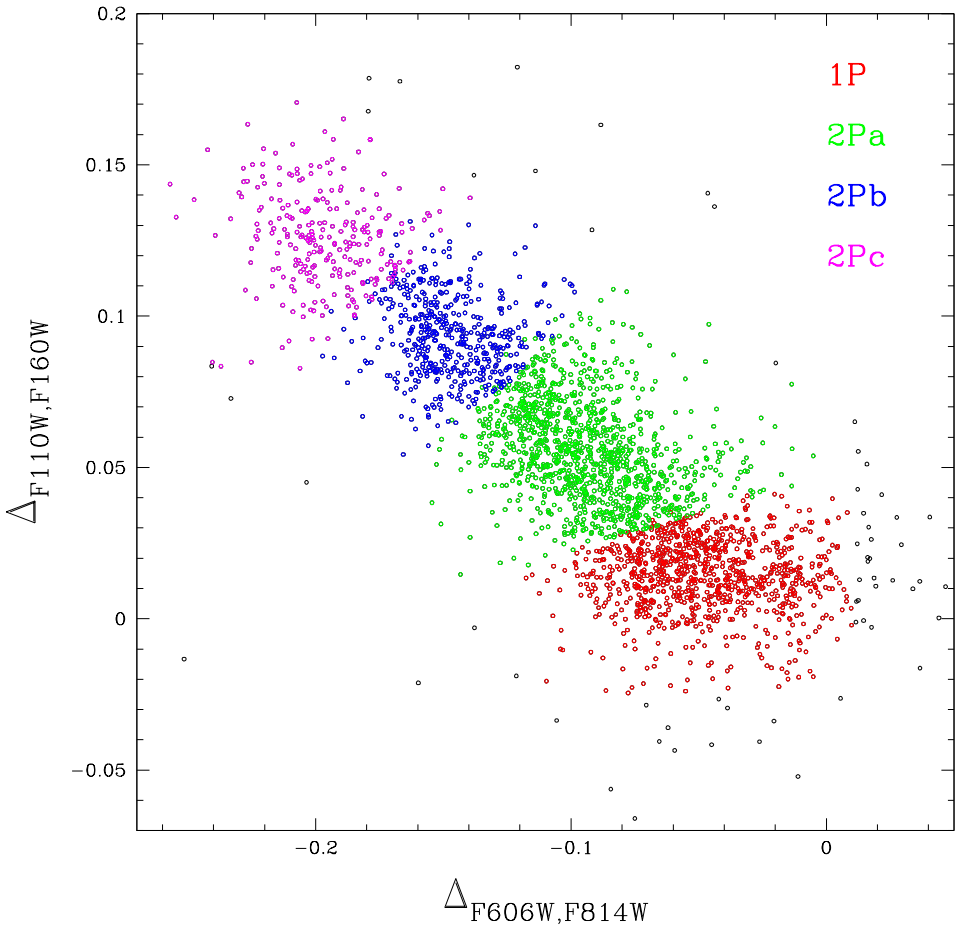

Figure 4.1: $\Delta_{F110W,F160W}$ vs $\Delta_{F606W,F814W}$ ChM, derived for the sample of 47 Tuc stars below the MS knee studied through the thesis. Four groups of stars are selected and colored: 1P, 2Pa, 2Pb and 2Pc, respectively marked in red, green, blue and magenta. It is adopted the technique by Milone et al. (2023a).

4.3 Data analysis

The four groups of stars identified in the ChM are distributed in CMDs in a unique way, depending on the color choice, as already mentioned for Figure 3.3 and 3.4 in the previous Chapter 3. In the succeeding paragraphs I employed a rather sophisticated and new method. The concept is to combine all the available filters and select the filters' combinations that produce two critical diagrams, to which are dedicated the next subsections. Both diagrams are analyzed and further discussed through the

investigation of binary stars among MPs, each for a different purpose that will be specified.

4.3.1 IR diagram: broad sequences

Among CMDs, the choice of IR diagrams enables the observation of broad sequences (as discussed in Section 3.2 for some literature results on 47 Tuc). It's worth indicating that, as presented in Section 1.1, photometric diagrams sensitive to NIR light can accentuate O-abundance variations among MPs, for very low-mass stars. A CMD such as ($m_{\rm F606W}$ vs $m_{\rm F110W} - m_{\rm F160W}$) diagram in Figure 4.2 maximizes the separation of the stellar populations, highlighting, below the MS knee, at least the four already mentioned families: 1P stars, bluer, and 2Pa-b-c, oxygen-depleted and redder. This has been confirmed by many published works, including Milone et al. (2012e) and Dondoglio et al. (2022). However, it could be a simplification of a much more complex configuration of stellar populations among M-dwarf stars, because other authors claim the presence of even more subgroups of 2P stars. To provide an example, Marino et al. (2024) categorize 2P into four groups.

Henceforth, the CMD presented in this section is chosen as it enhances the separation among the observed distinct stellar sequences, and it prevents their superposition. The final task would be to collocate the observed binaries on top of these sequences.

4.3.2 An original color combination: overlapping sequences

Inside traditional CMDs in the optical-NIR regime, the MPs' sequences are seen partially superimposed, even though the effect is not exactly boosted. One example is the visual-NIR $m_{\rm F606W}$ vs $m_{\rm F606W} - m_{\rm F160W}$ CMD in Figure 4.3: in contrast to the previous IR diagram, this one portraits, also below the MS knee, an extremely narrow MS. The concept is to focus on this region of the CMD, and explore a color combination such that a clear distinction between MS and MS binaries could be brought up, in order to identify and properly select the binaries among MPs. In practice, the distribution of the four populations in this exact diagram does not allow the binaries selection. Therefore, it becomes necessary the construction of a pioneering CMD with a different color combination, to enhance the effect of superposition of the sequences.

Rather than the previous optical diagram, it is preferred the color combination shown in Figure 4.4, for the $m_{\rm F606W}$ vs $[({\rm F606W}-{\rm F160W})-0.25({\rm F606W}-{\rm F814W})]$ pseudo-CMD. This is an unconventional photometric diagram which exhibits overlapping sequences of MPs in 47 Tuc, therefore, it represents a convenient choice. The quantity in abscissa is defined as $[({\rm F606W}-{\rm F160W})-0.25({\rm F606W}-{\rm F814W})] = [(m_{\rm F606W}-m_{\rm F160W})-0.25(m_{\rm F606W}-m_{\rm F814W})]$. I decided to conduct the analysis on this CMD, because it allows a better visualization of the sequences' overlap, fundamental to perform a selection of stars which excludes the binaries, and at the same time a selection which allows to disentangle them and the MS stars.

After having chosen the proper CMD, focusing on the appropriate magnitude

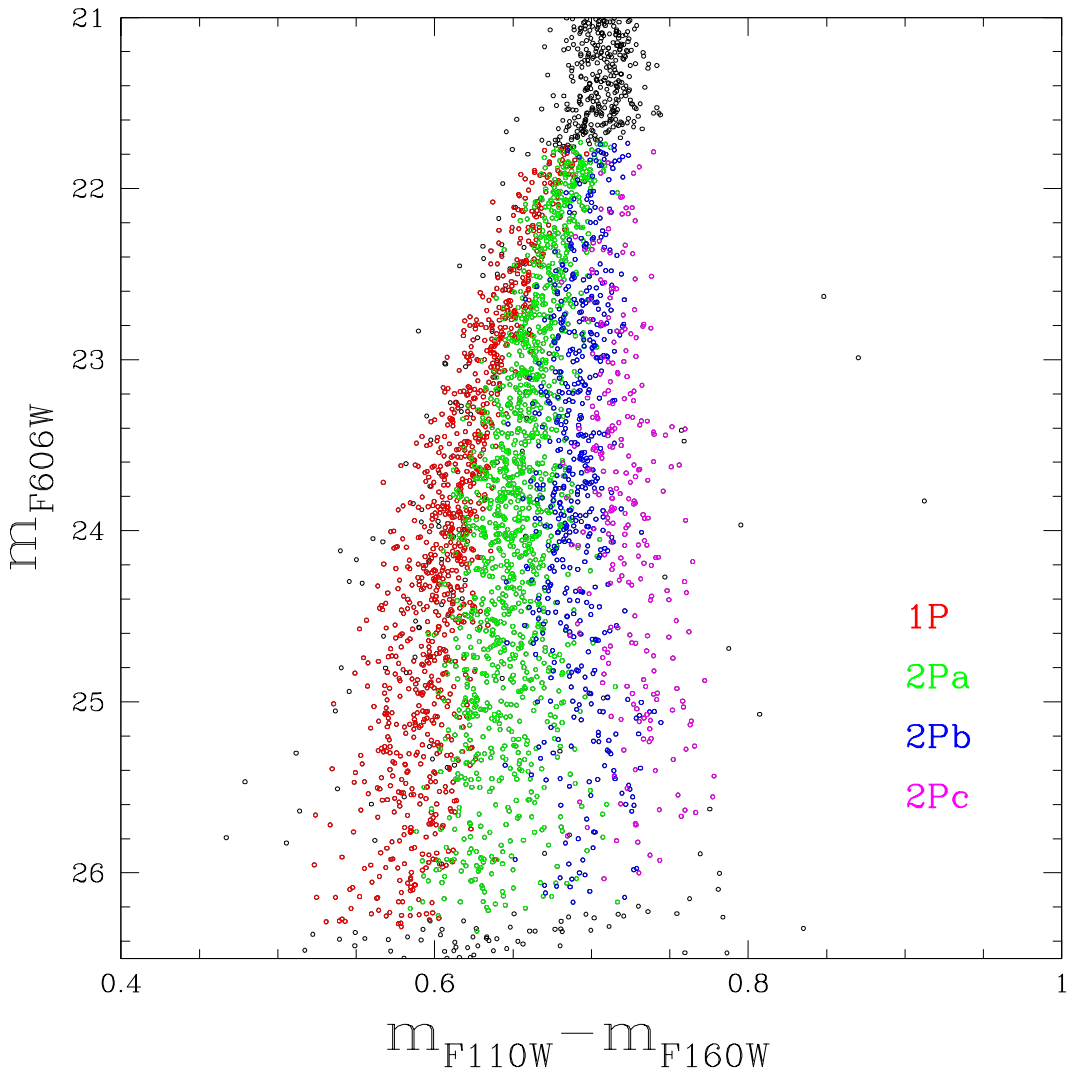

Figure 4.2: $m_{\rm F606W}$ vs $m_{\rm F110W} - m_{\rm F160W}$ CMD of 47 Tuc zoomed in the zone of the MS knee. Here, the broadening of the stellar distributions corresponds to the presence of MPs. I highlight with colors stars associated to the four detected populations.

range (stars below the MS knee), a fiducial line is derived for each population, aimed to reveal subtle differences among the MPs. This is obtained by dividing the selected MS stars into bins of 0.75 mag each, measuring their median value in color as well as in magnitude, and then fitting these points. The fiducial lines associated to population 1P, 2Pa, 2Pb and 2Pc, are highlighted in Figure 4.5.

Exploring the CMDs in all the considered filters, the ones provided with color combinations of F475W, which I personally reduced, do not highlight the most favourable distribution of the MPs (maximization of broad sequences or evident overlap of sequences). For this reason, that specific dataset offers sub-optimal strategy to achieve the thesis goal. In fact, the photometry in F475W which I am using is not properly optimized for the study of faint stars: other filters reach deeper than F475W, e.g. F606W. Presumably, the analysis of diagrams in the filter F475W

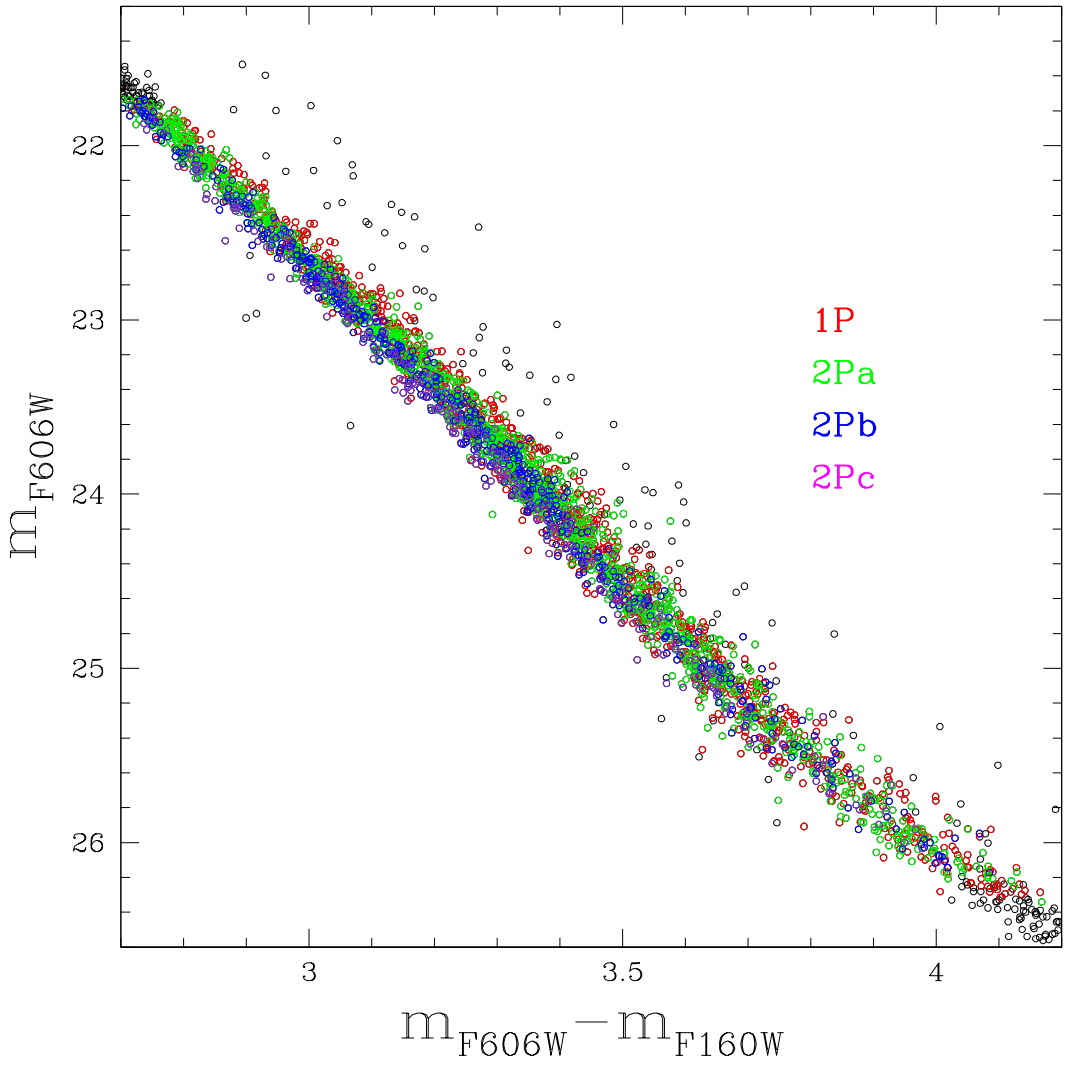

Figure 4.3: $m_{\rm F606W}$ vs $m_{\rm F606W} - m_{\rm F160W}$ CMD of 47 Tuc using optical-NIR filters. Such a color combination enables a partial superposition of different sequences, below the MS knee. I highlight stars of different populations as in Figure 4.2.

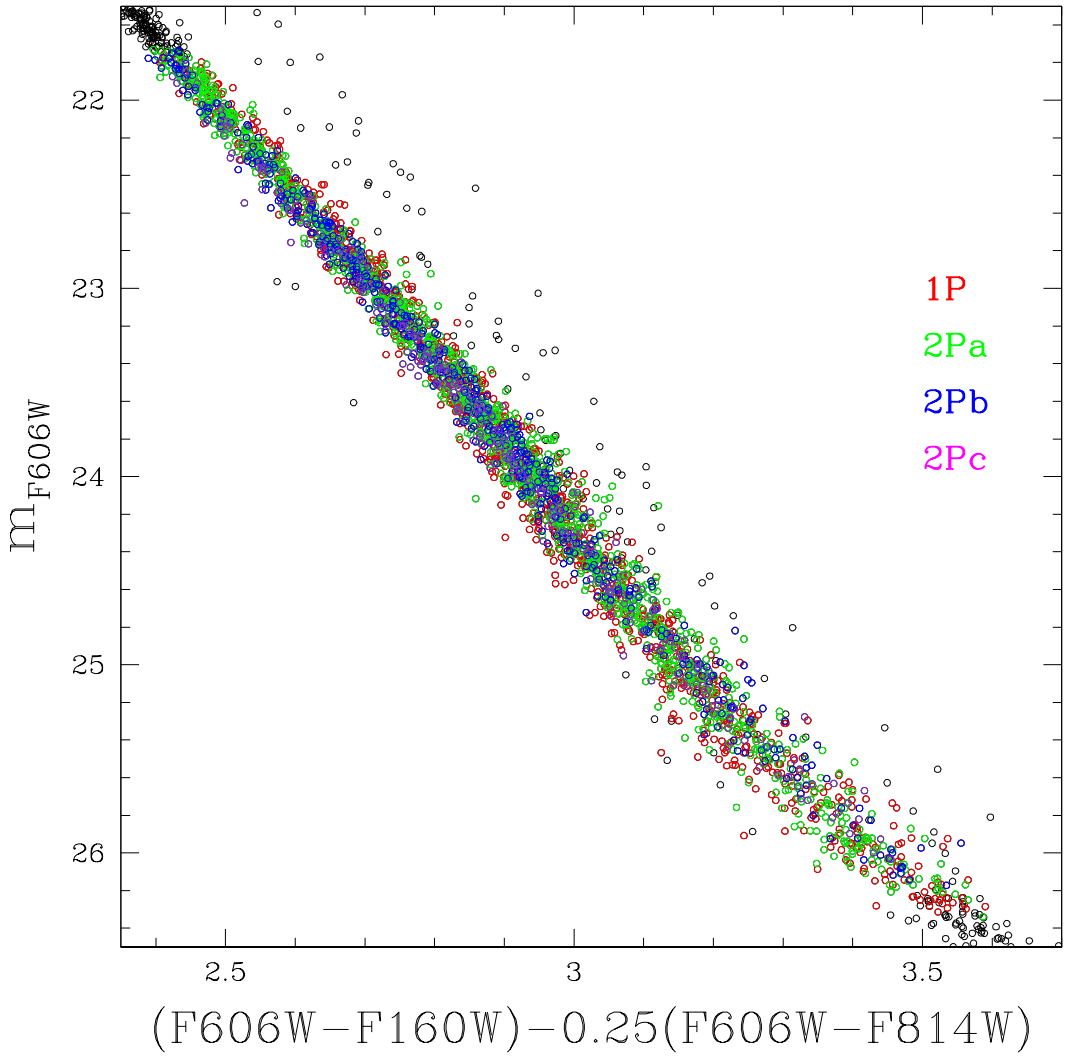

Figure 4.4: m_{F606W} vs [(F606W−F160W)−0.25(F606W−F814W)] CMD, zoomed on the magnitude interval ∼21.7–26.3 mag, below the MS knee of 47 Tuc. This color combination maximizes the superposition of the MPs' sequences. Binary stars are visible on the top-right of the distribution of MS single stars (see further details in Section 1.3). The four selected populations are marked with the appropriate colors.

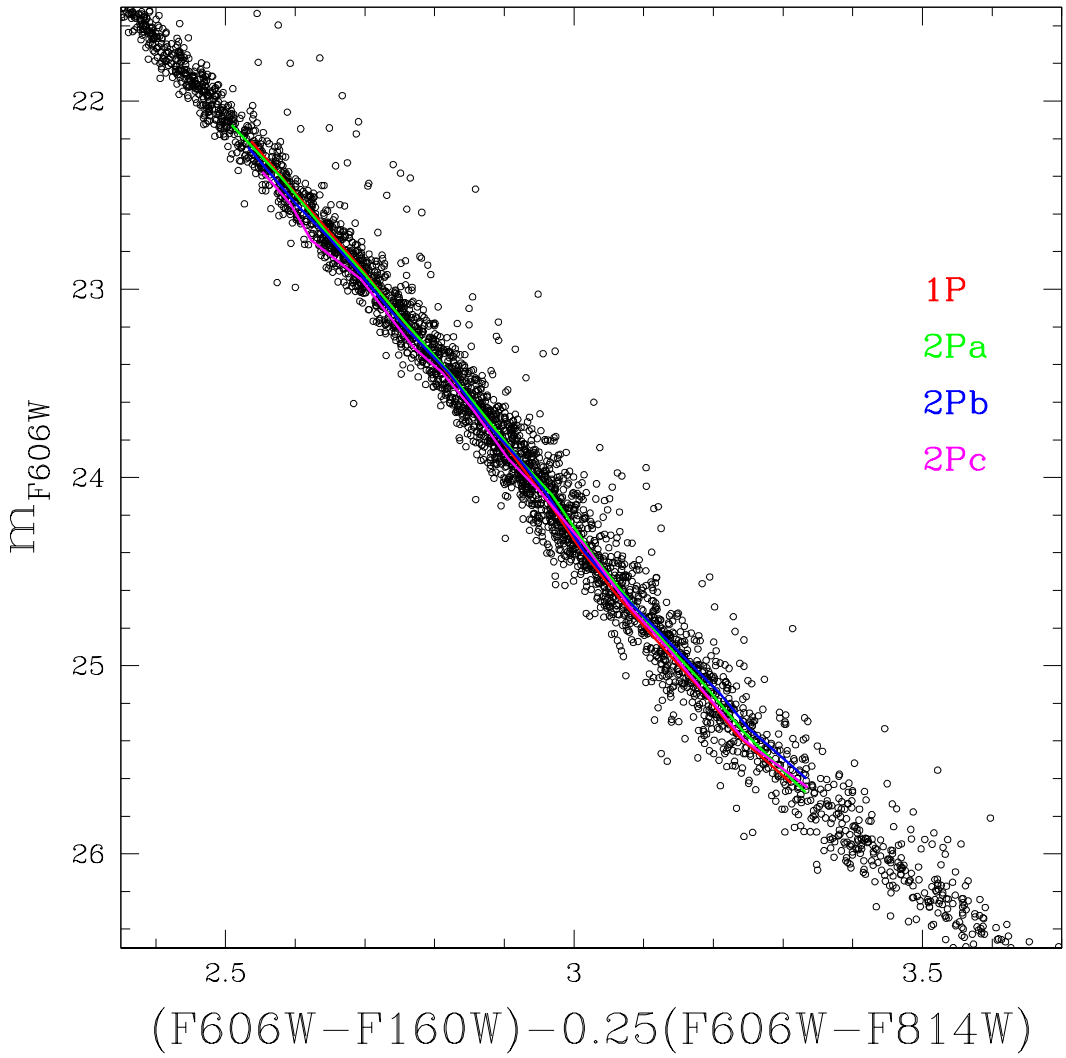

Figure 4.5: m_{F606W} vs [(F606W−F160W)−0.25(F606W−F814W)] CMD of 47 Tuc zoomed on the region of interest for data analysis. The colored lines correspond to the fiducial lines for the four populations.

would have lead to the loss of the faintest stars, allowing instead a selection of the brightest binaries alone.

4.3.3 Binaries selection

Statistically, it is more likely that a generic system of binary stars includes companions of different mass. However, to model the binaries distribution on a CMD, it is first assumed that they share the same mass value, giving the already clarified mass ratio $q = 1$. If this is the case, we expect equal-mass binary systems to form a sequence which runs parallel to the cluster fiducial line, but brighter in magnitude for the amount of $\sim$0.75 mag (see details on binaries and on the mass ratio q parameter, in the dedicated Section 1.3.2). All the binary systems composed instead of stars of different mass occupy the CMD region confined within the fiducial line of single stars and that of equal-mass binaries.

The Figure 4.6 illustrates the selection of the sample of binaries to study, performed on the CMD where the MPs overlap. It is shown the magnitude range $\sim$17-28 mag, where the upper limit corresponds approximately to the MS turn-off point, namely the bluest point of the sequence, above which the SGB starts. In black is traced the continuous fiducial line of the MS of 47 Tuc, assuming that the cluster is consistent with an SSP. A dashed black line is set on the right of the MS, separated by the amount of 4 times the error on the median values associated to the fiducial line. Then, I set as the left and right boundaries for the sample selection, respectively, the red and the blue line in Figure 4.6: these ones are fiducial lines associated to binary systems. I identify equal-mass binaries with the blue line, whereas the red one is chosen for practical reasons and traced by hand. In fact, on the left I would have encountered the sequence of single stars. The principle is to minimize the contamination of the sample from MS single stars and from field stars. The orange triangles mark all the binaries belonging to the MS.

The more advanced step consists in narrowing the sample of candidate binaries. It is further investigated a subsample of 41 binaries, covering the magnitude range $\sim$21.7-25.5 mag, as visible in Figure 4.7. The selected magnitude range is exactly the one that I am allowed to study, because it corresponds to the one where the four populations are disentangled through the ChM of Figure 4.1. The upper and lower horizontal green lines, respectively at $\sim$21.7 mag and $\sim$25.5 mag, are effective for delimiting the studied binaries. The sample of binaries is overimposed on top of the cluster's MS, which is in gray in the Figure.

The CMD of Figure 4.8 is the m_{F606W} vs $m_{\mathrm{F110W}} - m_{\mathrm{F160W}}$ diagram previously selected: as discussed, it represents a valid choice to discriminate among the binaries belonging to each of the stellar populations. For all the four populations is highlighted the fiducial line of the MS single stars, with the appropriate color. The sequences are almost vertical, indicating that the stellar colors tend to be constant.

The same CMD is shown in Figure 4.9, adding four dashed lines. These ones are the fiducial lines of equal-mass binaries identified within a certain population. As mentioned in the previous paragraph, the sequence of equal-mass binaries is expected to be $\sim$0.75 mag brighter than the cluster fiducial line: this is clear from the comparison of dashed and solid line of one population at a time. In fact, in Figure 4.9, this behaviour can be observed. Particularly for 1P stars, the solid and

dashed red lines run parallel to each others, almost reaching the MS knee. A similar feature applies to the other three populations' distributions, though appearing less evident.

Finally, a third version of the same diagram is proposed, combining the information enlocked in the previous two CMDs with the position of the examined sample, in Figure 4.10. The image illustrates the 41 sampled binaries, marked with orange triangles, overimposed on top of the gray dots, which represent all the stars observed below the MS knee. Clearly, looking at the binaries distribution, one may be already tempted to infer that they belong to 1P mostly.

4.3.4 Verticalization of the CMD

The CMD which maximizes the color separation between MP binaries, is used to derive the verticalized diagram. The verticalization is a two-step procedure, which is applied to Figure 4.10. Briefly, exploiting the color associated to the two external populations (1P and 2Pc), first I operated along the right and then I proceeded along the left line. I associated a red line to 1P and a blue line to 2Pc. In Figure 4.11 is shown the final m_{F606W} vs $\Delta_{\mathrm{F110W,F160W}}$ verticalized diagram, having defined the quantity $\Delta_{\mathrm{F110W,F160W}}$ in abscissa as a pseudo-color, which is set to 0 and 1, respectively, for 1P and 2Pc single stars.

As a summary of the observational result, Figure 4.12 presents three panels, displaying the verticalized diagram (top), together with the corresponding kernel-density, ϕ (middle), and the cumulative distributions, ρ (bottom), for the quantity $\Delta_{\mathrm{F110W,F160W}}$. For the kernel-density distribution is adopted a Gaussian kernel of a fixed width factor of 0.2 (see Silverman, 1986, for the insight on this statistical tool for data analysis). It is useful for visualization purposes, as it reproduces the kernel, superimposed over an histogram having bins of the width of 0.2 $\Delta_{\mathrm{F110W,F160W}}$.

These diagrams showcase the observational finding obtained so far: through their analysis is possible to notice the imbalance of the observational data toward 1P stars, rather than detecting for example a smooth identical distribution over the four populations. Anyway, it is already clear that the $\Delta_{\mathrm{F110W,F160W}}$ distribution is not consistent with a single population.

4.4 Evaluating the binary frequency within the distinct populations

To measure the fraction of binary stars belonging to the first and second population, is required a comparison of the observed binaries distribution for 47 Tuc, with simulations. Simulated diagrams are constructed starting from artificial stars.

4.4.1 Artificial stars

Artificial-stars (AS) are generated through the methodology developed by Anderson et al. (2008) in order to derive synthetic CMDs. The whole reduction of ASs

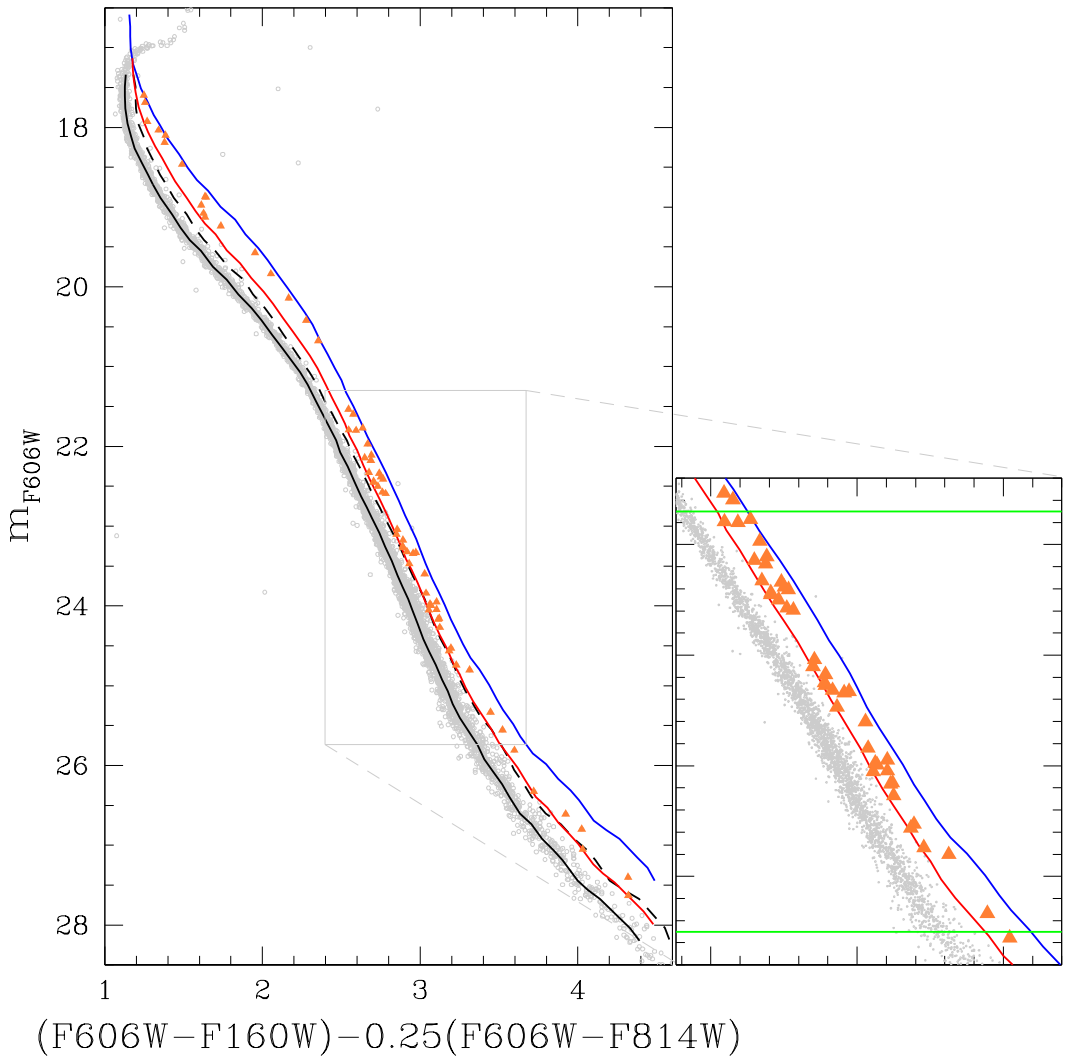

Figure 4.6: m_{F606W} vs [(F606W − F160W) − 0.25(F606W − F814W)] CMD for the whole MS. It is visible also a rather short portion of SGB (m_{F606W}< 17 mag). The color boundaries (blue and red line) are chosen on this CMD, to perform the selection of binaries to inspect. The zoom-in panel on the right focuses on the 41 studied binaries, and it is repeated in the next Figure 4.7.

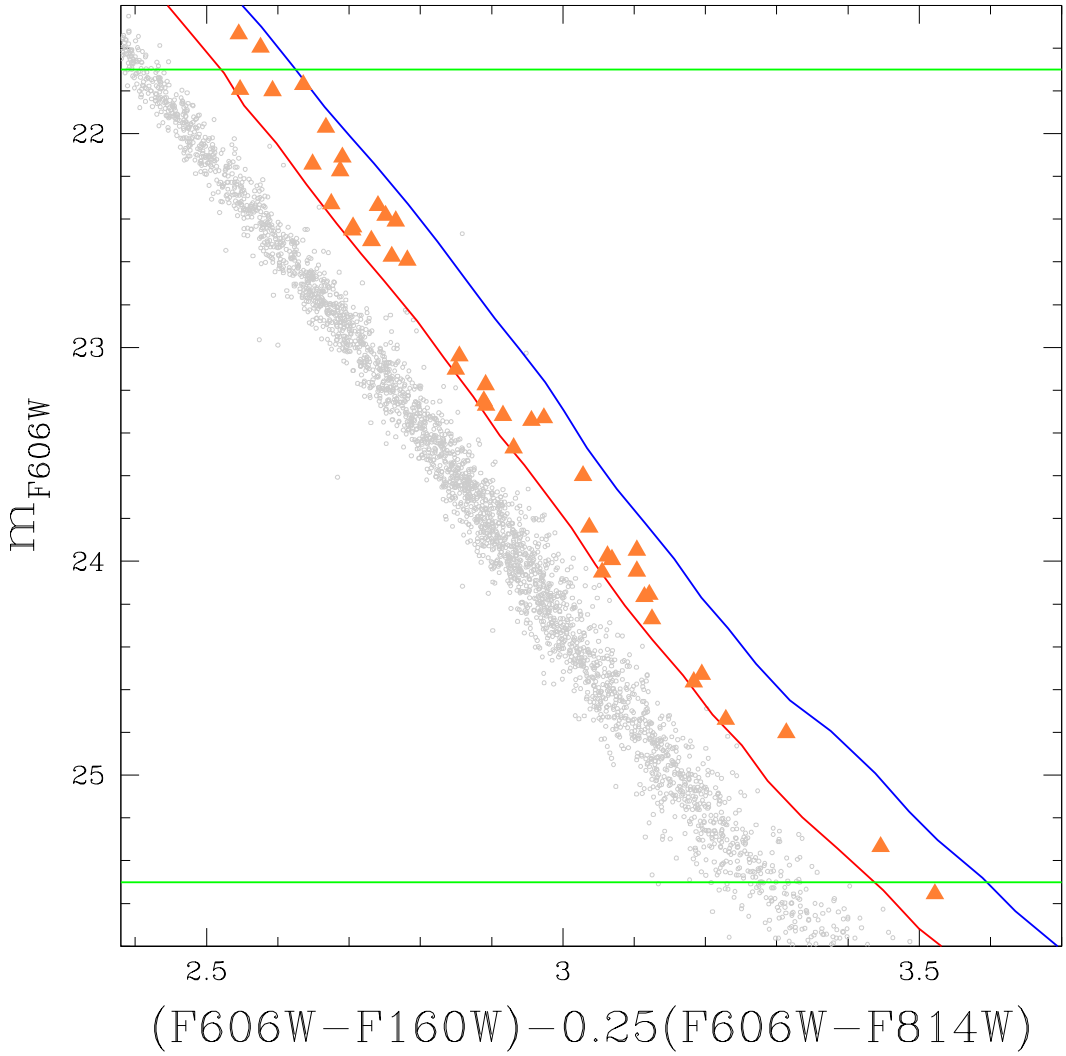

Figure 4.7: Selection of the binaries sample to be analyzed in 47 Tuc from $m_{\rm F606W}$ vs [(F606W − F160W) − 0.25(F606W − F814W)] CMD. The green horizontal lines at $m_{\rm F606W}$∼21.7 mag and $m_{\rm F606W}$∼25.5 mag indicate the magnitude boundaries applied to perform the sample selection. The blue and red lines are the same as in the previous Figure 4.6.

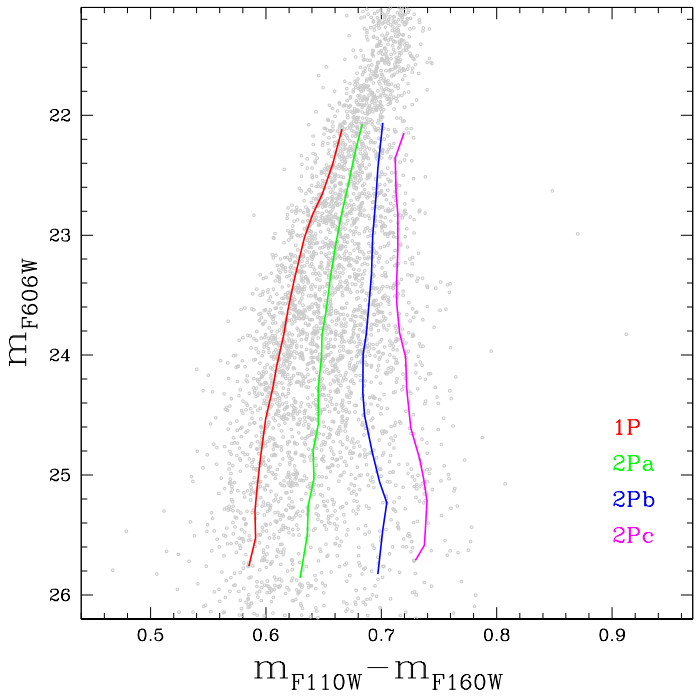

Figure 4.8: $m_{\rm F606W}$ vs $m_{\rm F110W} - m_{\rm F160W}$ CMD for VLM stars of 47 Tuc. The four colored lines are fiducial lines for MS single stars from the four populations.

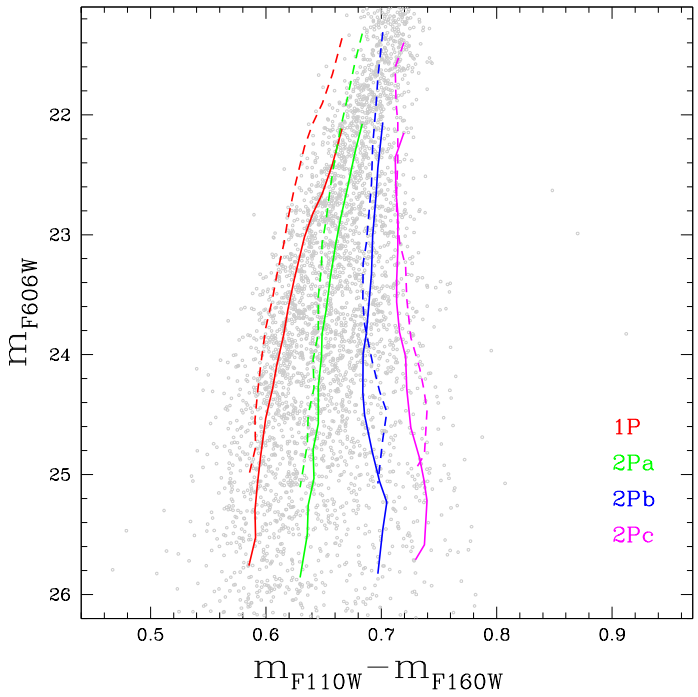

Figure 4.9: Same as Figure 4.8. The colored dashed lines are the fiducial lines associated to MS equal-mass binaries.

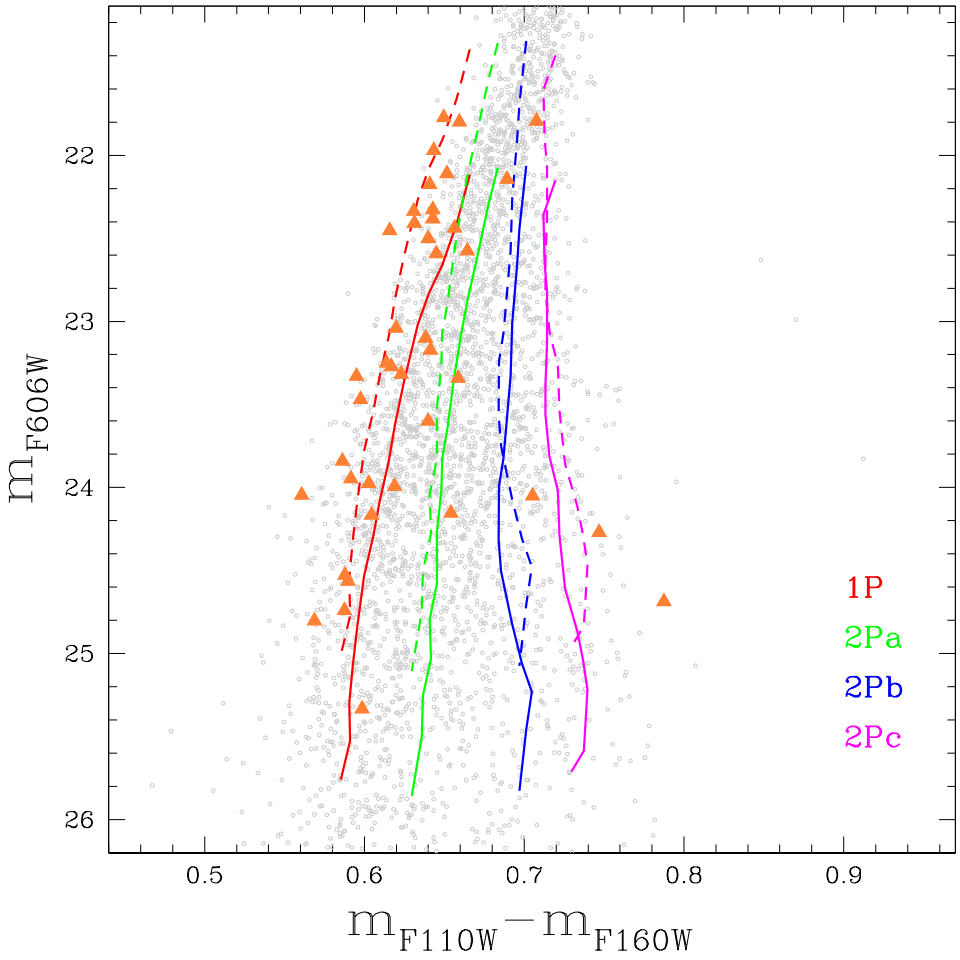

Figure 4.10: Same as in Figure 4.8 and 4.9, with the additional superposition of the sampled binaries, marked with orange triangles.

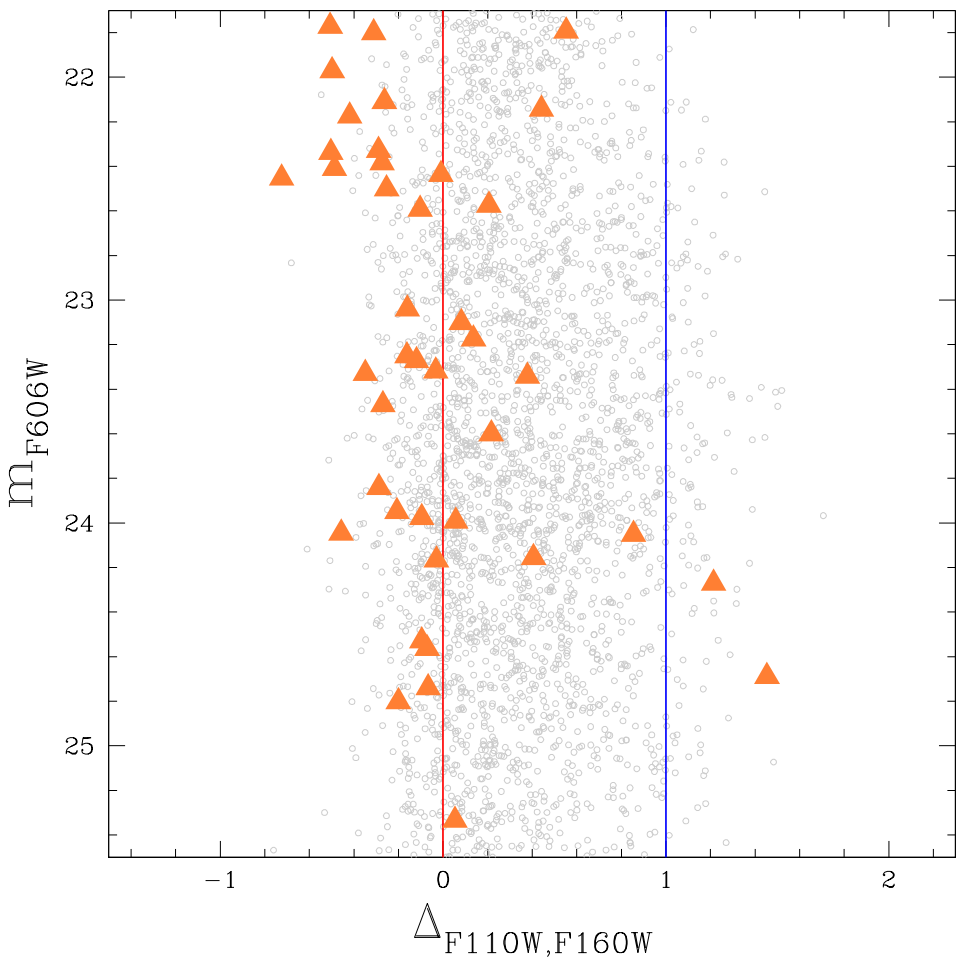

Figure 4.11: The m_{F606W} vs $\Delta_{F110W,F160W}$ verticalized CMD of 47 Tuc. The orange triangles are the selected sample of binaries, the vertical lines are the fiducial lines for 1P and 2Pc populations.

is applied utilizing the same computer programs and procedure employed for the observed stars and described in Chapter 2.

In essence, it is generated a catalog of 10,000 ASs, assuming the same luminosity distribution as for the sample of real stars. Their m_{F606W} magnitude is calculated from the colors of the fiducial lines of each of the four populations, obtained from the observational CMD of Figure 4.8.

One remark should be made on this aspect: it was necessary an extrapolation on the border of each of the fiducial lines, by hand. It was selected one point above and one point below the extremes of the four fiducial lines. In fact, by having let the program extrapolate automatically, we would have lost many stars. The error associated to the manual extrapolation is instead much smaller, and it is not expected to affect the results. It is interesting, for example, how the magenta solid line for 2Pc curves toward the left, below $m_{F606W}\sim$25.4 mag. This is a numerical error and not a physical one, therefore, selecting by hand an additional part of the line helps correcting the problem rather than contributing to it.

The ASs' binaries are then formed taking into account couples of stars belonging

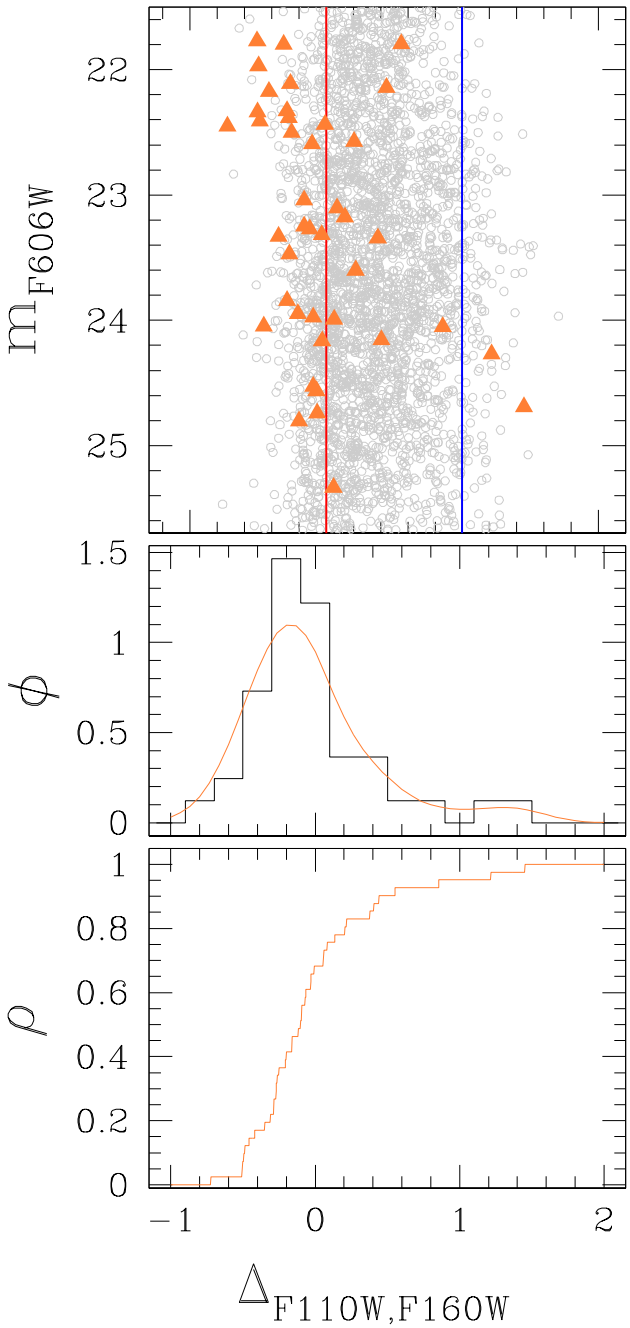

Figure 4.12: The figure presents the m_{F606W} vs $\Delta_{F110W,F160W}$ verticalized diagram (as in Figure 4.11) for the selected binaries (top), the corresponding $\Delta_{F110W,F160W}$ kernel distribution ϕ (middle), and the cumulative distribution ρ (bottom). Details are given in Section 4.3.4.

to the same population, such as 1P-1P binaries or 2Pa-2Pa binaries. No mixed binaries are included.

4.4.2 Simulations

In this subsection, I describe the procedure to estimate the fraction of 1P-1P binaries with respect to the total number of binaries. The first step consists in comparing the observational result with the results obtained from grids of simulated diagrams that virtually comprise all combinations of MPs' binaries. Then, I accounted for the fraction of 1P stars of the cluster (from Marino et al., 2024), in order to derive the probability that a binary star belongs to 1P, rather than 2P.

To establish a comparison with the observations, I defined a grid of values corresponding to the number of stars selected within each population, namely for n_{bin}^{1P-1P}, $n_{bin}^{2Pa-2Pa}$, $n_{bin}^{2Pb-2Pb}$ and $n_{bin}^{2Pc-2Pc}$. I assumed that the number of artificial stars ranges from 0 to 10,000, and I proceeded through steps of 500 stars, such that adding 500 units to one population would imply subtracting the same amount from one of the remaining three populations. I calculated the quantity of $\Delta_{\rm F110W,F160W}$ and the corresponding cumulative distribution for the simulated binaries, analogously with the procedure applied to real stars. The comparison of simulated and observational cumulative distributions is done by means of the χ^2, defined as:

$$\chi^2 = \sum (\rho_{AS} - \rho_{obs})^2, \tag{4.1}$$

where the terms ρ_{AS} and ρ_{obs} refer respectively to the cumulative associated to ASs and to observations. The best-fit combination of ASs should have the smallest χ^2 parameter, indicative of the simulation which best represents the observational result.

Some examples are shown in Figure 4.13 and 4.14: it is illustrated the simulated $m_{\rm F606W}$ vs $\Delta_{\rm F110W,F160W}$ pseudo-CMD of each of the four extreme distributions of binaries, focusing entirely on one-population-binaries in each panel. Figure 4.13 depicts the outcome of simulations where n_{bin}^{1P-1P}= 10,000 or $n_{bin}^{2Pa-2Pa}$= 10,000. Instead, Figure 4.14 presents the cases where I simulated either $n_{bin}^{2Pb-2Pb}$= 10,000 or $n_{bin}^{2Pc-2Pc}$= 10,000. In every simulated verticalized diagram, the observed binaries are depicted with orange triangles, and they are all provided with the relative cumulative distribution, compared with the observed one (displayed with the orange and the black line, respectively). Clearly, neither of those four simulations represents the best-fit case, moreover, the χ^2 parameter is too high.

To pinpoint the simulation that best reproduces the observations, I adopted the following reasoning. A huge amount of simulations were made, accounting for all the possible combinations of binaries. However, there are only a few of them which provide a small χ^2. The case presented hereafter corresponds to the best match of the observational finding, for the minimum χ^2.

The resulting best-fit $m_{\rm F606W}$ vs $\Delta_{\rm F110W,F160W}$ verticalized diagram, with the panel for the comparison of simulated and observed cumulative distribution, is plotted in Figure 4.15. I determined the occurrence of binary systems associated with 1P, expressing the observed fraction $f_{bin,o}^{1P-1P}$ in relation to the total, as well as the fraction of the remaining 2P binaries ($f_{bin,o}^{2P-2P}$). The fraction of stars in each population that has been instrumental for finding the best-fit with observations, gives $f_{bin,o}^{1P-1P} \backsimeq 80\%$ and $f_{bin,o}^{2P-2P} \backsimeq 20\%$.

In terms of the χ^2, similar low level is obtained by changing the number of binaries belonging to a first population (n_{bin}^{1P-1P}, and also the resulting fraction

Simulation	$f_{bin,o}^{1P-1P}$	$f_{bin,o}^{2P-2P}$
a	0.80	0.20
b	0.70	0.30
c	0.65	0.35
d	0.75	0.25

Table 4.1: Four of the simulations which provide a small χ^2. Test (a) corresponds to the best-fit.

$f_{bin,o}^{1P-1P}$) by ∼10%. A few examples are provided in Table 4.1. Even though these alternative cases (the case (b), (c), and (d) in the table) are not analyzed further, they are comparable with each others, and they are in agreement with the best-fit result. In fact, even through a slight change of the parameters, apart from a negligible variation, they all definitely indicate a predominance of 1P binaries.

To determine the frequency of 1P and 2P binaries (i.e. the fraction of binaries within each population in the ideal case of a GC with the same number of 1P and 2P stars), it is necessary to account for the observed population ratio within 47 Tuc. I assumed that 1P and 2P stars comprise 38.1±1.2% and ∼61.9% of the total number of stars, respectively (Marino et al., 2024). The following approach takes into account the population ratio $R_{MS} = \frac{N_{MS,2P}}{N_{MS,1P}} = 1.62$, derived from these percentages of 1P and 2P stars.

By combining the information on the fraction of observed binaries in 1P, and the cluster ratio 2P/1P, I calculate the probability of finding 1P binaries ($\widehat{f}_{bin}^{1P-1P}$), through the following formula:

$$\widehat{f}_{bin}^{1P-1P} = \left(\frac{n_{bin}^{1P-1P} \cdot R_{MS}}{(n_{bin}^{1P-1P} \cdot R_{MS}) + n_{bin}^{2P-2P}} \right), \tag{4.2}$$

where n_{bin}^{1P-1P} and n_{bin}^{2P-2P} respectively indicate the number of binaries selected within 1P and 2P, while R_{MS} corresponds to the ratio of 2P over 1P MS stars.

From this method, I obtain the frequency $\widehat{f}_{bin}^{1P-1P} \backsimeq 0.87$ and the corresponding complementary frequency $\widehat{f}_{bin}^{2P-2P} \backsimeq 0.13$.

4.4.3 Uncertainties

To estimate the uncertainties on the probability of finding 1P or 2P binaries, I performed an analysis based on bootstrap simulations. According to the *Bootstrap* procedure, first of all I generated a catalog of 41,000 simulated binaries. Those consist of 1,000 samples, in which I replaced the original 41 observed binary systems through random sampling. Then, it was randomly extracted one sample of 41 binaries at a time, evaluating the fraction of 1P and 2P, adopting the same procedure described above for the real stars. This step is repeated, applying the technique 1,000 times.

The random mean scatter obtained from the simulated 1,000 determinations of the values of f_{bin}^{1P-1P} and f_{bin}^{2P-2P} provides the corresponding uncertainty on the result

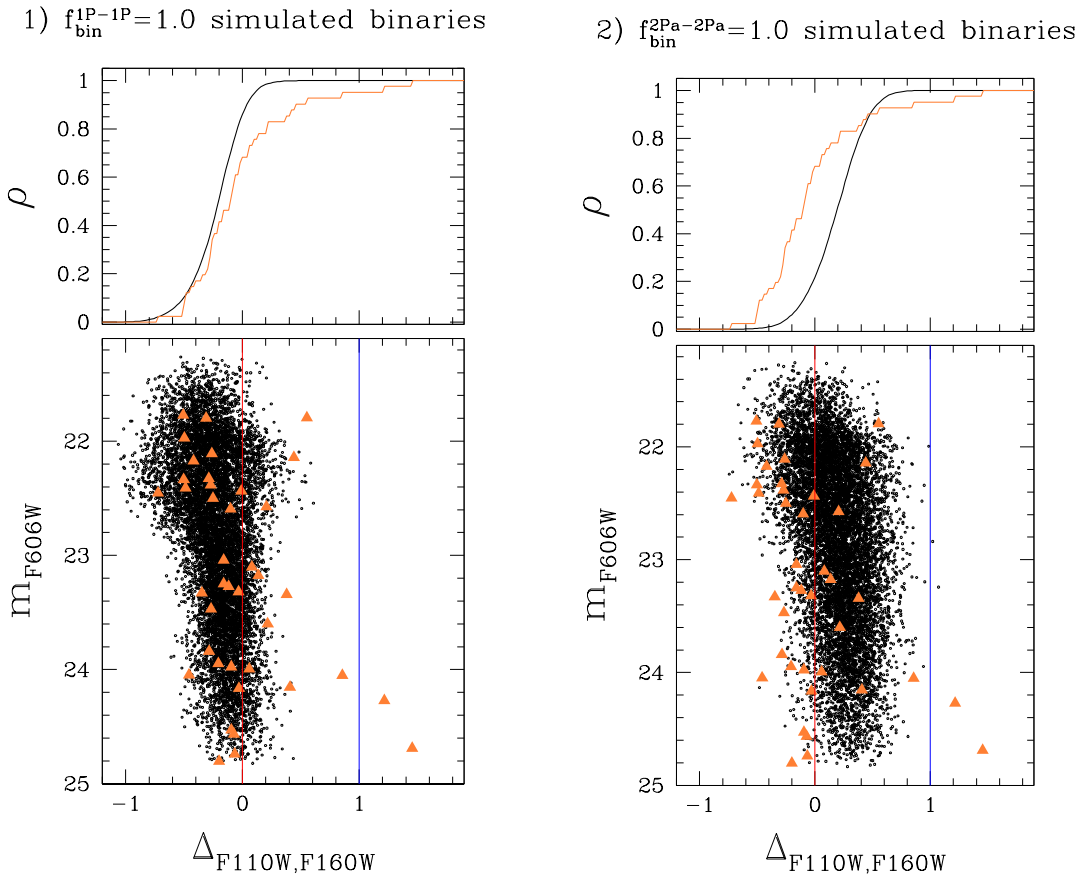

Figure 4.13: *Left panel*: simulation including 1P-1P binaries alone. *Right panel*: the total of binaries in the simulation belongs to population 2Pa.

of my observations. The uncertainty is computed for the four stellar populations and it corresponds to the estimates provided in Table 4.2.

The error associated with the frequency of 1P and 2P binaries is estimated through formula 4.2 by means of error propagation. I find that the frequencies of 1P and 2P binaries correspond to 87±13% and 13±13%, respectively.

47 TUC	$f_{bin,o}^{1P-1P}$	$f_{bin,o}^{2Pa-2Pa}$	$f_{bin,o}^{2Pb-2Pb}$	$f_{bin,o}^{2Pc-2Pc}$
Observed values	0.80 ± 0.12	0.00 ± 0.03	0.15 ± 0.07	0.05 ± 0.04

Table 4.2: The table summarizes the observational result: the binaries' fractions and the associated uncertainties, computed through the bootstrap procedure.

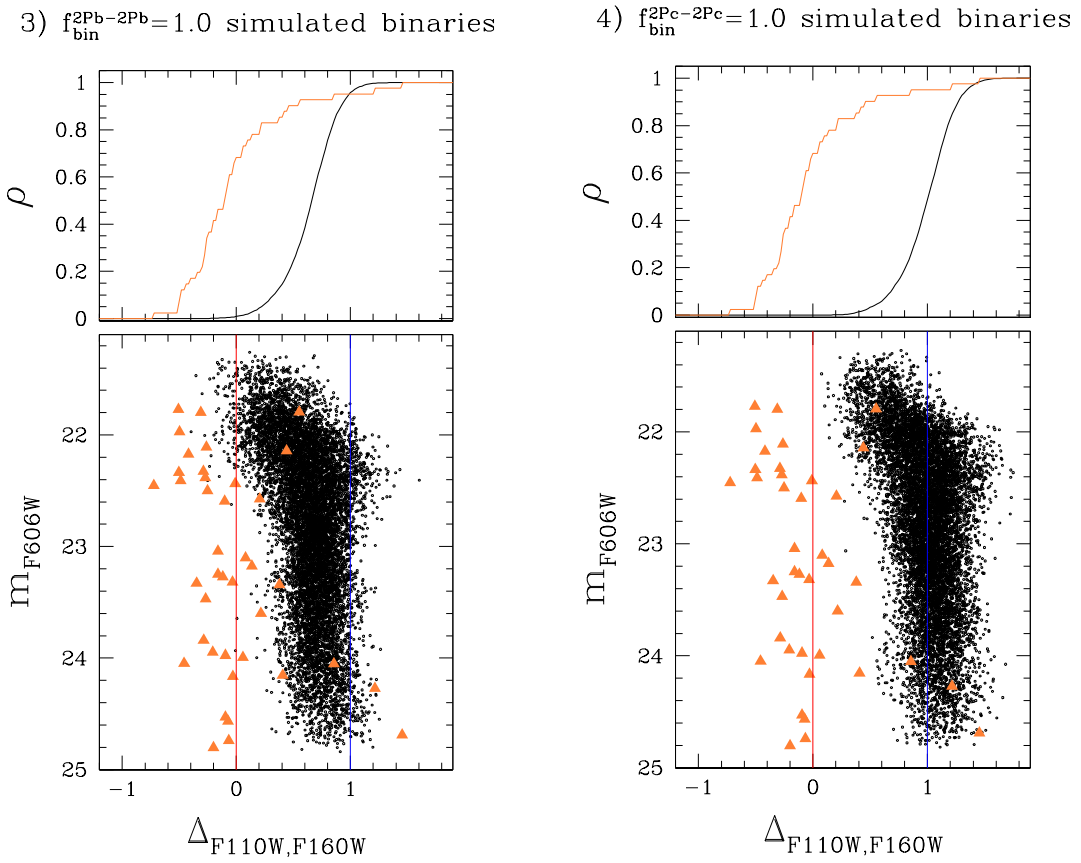

Figure 4.14: *Left panel*: simulated diagrams for a population entirely made up by 2Pb binaries. *Right panel*: simulation of artificial binaries belonging to 2Pc alone.

47 TUC	f_{bin}^{1P-1P}	f_{bin}^{2P-2P}
Final probabilities	$87 \pm 13\%$	$13 \pm 13\%$

Table 4.3: I present the computed probabilities of finding binaries within each population.

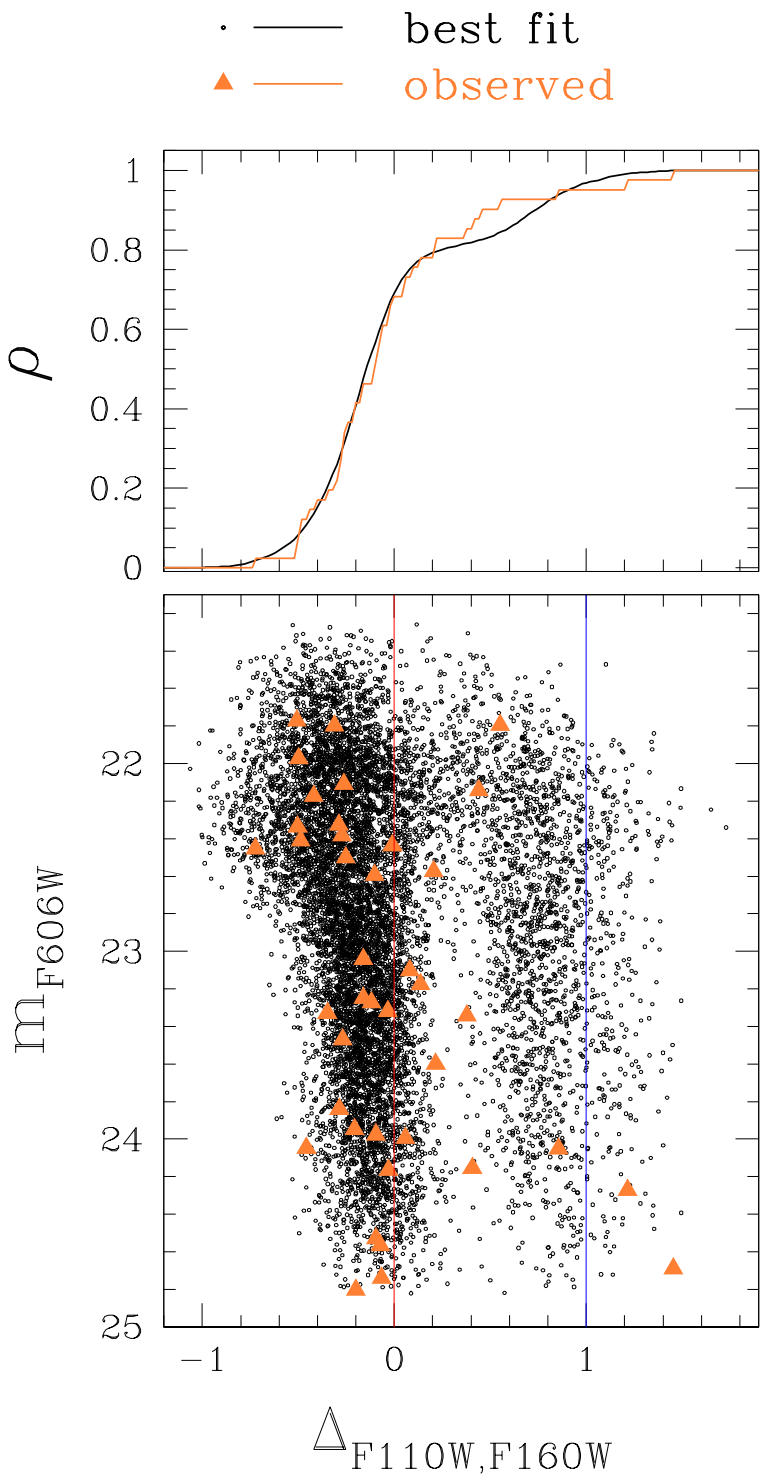

Figure 4.15: It is presented the best-fit case discussed in the text. The distribution of observed binaries is marked in orange in the panels for the cumulative distribution and in the pseudo-CMD, while I highlight the simulation in black. Notice that the distribution of ASs does not corresponds either to the extreme tests in Figure 4.13 or in 4.14.

Chapter 5

Summary and conclusion

In the paste two decades extensive investigation is being dedicated to the theoretical and observational study of MPs detected inside GCs. The recent discoveries and the characterization of this phenomenon raised several questions concerning the formation and the dynamical history of these systems. A large number of hydrodynamical and N-body simulations (e.g. D'Ercole et al., 2008), propose that 2P stars form from material polluted by the ejecta of more-massive 1P stars. Such simulations predict that the young 2P stars generate a compact subsystem in the inner regions of the more diffuse 1P cluster. According to the prediction, through its dynamical evolution, the cluster evolves toward a configuration where the two populations tend to mix and the typical structure imprinted by the process of 2P formation is smoothed out. Several observational studies indicate that the 2P stars of some GCs are more spatially concentrated than 1P members (e.g. Sollima et al., 2007b; Cordero et al., 2014). On the contrary, the 1P and 2P stars of dynamically old GCs are typically mixed (e.g. Dondoglio et al., 2021).

In this context, the present-day binary fraction of 1P and 2P stars may serve as a dynamical fingerprint of the processes which determined the current cluster structure. Binary stars play an essential role in the dynamical evolution of globular clusters. Based on the combination of analytic calculations and simulations, it is expected that the binaries' survival rate (also indicative of disruption, hardening and ejection) is actively affected by the environment they were born in. Until the different populations are completely mixed, 2P binaries evolve in a much denser environment where disruption events are expected at a higher rate than for 1P. The calculations employed by Vesperini et al. (2011) show that indeed the 2P disruption rate can be significantly larger than that of 1P. Considering hypothetical binary-binary and binary-single stars interactions, both for moderately hard and compact binaries, Hong et al. (2015, 2016) found a qualitatively similar result, indicating that disruption and ejection phenomena are more efficient in the higher-density regions. Initially, in this region 2P binaries are presumably the dominant population and therefore the one that is affected the most. Early observational constraints on the incidence of binaries among 1P and 2P stars of GCs rely on spectroscopy. D'Orazi et al. (2010) detected five Barium-rich stars in five GCs and noticed that four of them have content of sodium and oxygen consistent with 1P stars, whereas one star alone belongs to the 2P. The large barium abundance observed in these Ba-stars is linked to unseen evolved companions that transferred processed material to the visible star during their AGB phase. Consequently, the findings by D'Orazi and

collaborators suggest a prevalence of binaries among 1P stars.

Similar conclusions come from works based on spectroscopy of binary stars identified by means of radial-velocity variations. Building on a study involving 21 radial-velocity binaries across ten GCs, Lucatello et al. (2015) concluded that the fraction of binaries among 1P stars is 4.1±1.7 times higher than the fraction observed among 2P stars. This conclusion aligns with research by Dalessandro et al. (2018), who determined that out of 12 radial-velocity binaries in NGC 6362, only one belongs to the 2P.

The recent investigation of binaries in the cluster centers was obtained through multi-band HST photometry of bright MS stars. The results indicate that, in the core of M 4, the 1P binary incidence is about three times higher than the 2P incidence, in broad agreement with the conclusion from spectroscopy of a prevalence of 1P binaries. In contrast, NGC 288, NGC 6352, and NGC 6362 exhibit similar binary incidence rates in their central $\sim 2.7 \times 2.7$ square-arcmin regions (Milone et al., 2020b).

5.1 Binaries among multiple stellar populations in 47 Tucanae

In this research, I analyzed deep multi-band HST photometry for stars in the globular cluster 47 Tucanae.

The studied HST field is located at the distance of ∼7 arcmin, corresponding to ∼2 half-light radii, westward from the cluster center. The dataset comprises both high-precision photometry and astrometry that I derived for this project from ACS/WFC images in the F475W band, and the catalogues by Marino et al. (2024). This exquisite dataset allowed me to derive, the first time, the incidence of binaries among very low-mass MS stars.

I first derived the pseudo-color diagram called chromosome map and I used it to disentangle the distinct stellar populations among VLM stars. Specifically, I identify a group of 1P stars and three distinct groups of 2P stars with different oxygen abundances, namely 2Pa, 2Pb, and 2Pc.

Then, I introduced the $m_{\rm F606W}$ vs $[({\rm F606W}-{\rm F160W})-0.25({\rm F606W}-{\rm F814W})]$ pseudo-CMD, in which the different sequences are properly superimposed, and I used this new photometric diagram to select a sample of binaries. Finally, I analysed the distribution of the selected binaries in the ($m_{\rm F606W}$ vs $m_{\rm F110W}-m_{\rm F160W}$) CMD, which is very sensitive to stellar population with different oxygen abundances. Subsequently, it was compared, for the first time, the color distribution of the observed binaries with the corresponding distribution on a large grid of simulated diagrams characterized by all the possible combinations of stellar populations. This method allowed me to measure the incidence of binary systems among 1P and 2P stars in the still unexplored regime of VLM stars.

I find that the observed fractions of binaries belonging to first- and second-population stars are, respectively, $\sim 80\%$ and $\sim 20\%$. Since 1P stars comprise about 2/5 of the total number of VLM stars within the magnitude interval of interest, I conclude that the relative frequency of binaries among 1P stars is 87±13%.

The evidence for a prevalence of binaries among 1P M-dwarfs is quantitatively

consistent with the conclusions from spectroscopy of RGB stars (D'Orazi et al., 2014; Lucatello et al., 2015; Dalessandro et al., 2018). These results differ from the findings by Milone et al. (2020b) of a similar incidence of binaries among 1P and 2P stars, based on HST photometry.

Noticeably, the binaries analyzed in this work as well as most of the stars studied spectroscopically are located in the external cluster regions. In contrast, the results by Milone and collaborators rely on binaries in the cluster centers.

The observed differences are consistent with the predictions from N-body simulations of binary systems in GCs. These simulations show that the processes of binary evolution, disruption and the evolution of the spatial distribution of single and binary stars belonging to 1P and 2P are deeply interlinked. Together, they are responsible for the radial variation of 1P and 2P binary incidences, which is a relevant ingredient in the interpretation of the observational data probing a specific range of distances from the cluster's center. As the cluster evolves, the 2P global binary fraction decreases faster than that of 1P binaries. However, there are distinct local expectations: local binary fraction in the innermost cluster regions could be larger for 2P, whereas the outskirts may be mostly populated by 1P binaries.

For the first time among VLM stars, my result supports scenarios where a second generation of stars and its binary population form and evolve in the cluster center. My results on 47 Tuc, together with the methods that I have introduced in this thesis, provide exciting perspectives for the investigation of multiple populations and binaries in GCs. Supplementary numerical and observational studies are required in order to investigate, for example, the presence of mixed binaries, which are likely to result through the frequent encounters in a high density environment such as a cluster. Furthermore, the analysis could be extended to different fields located at the same distance from the center of 47 Tuc, as well as different distances, addressing the same stellar mass range. The promising instruments and filters onboard JWST could also provide new powerful color combinations to exploit focusing on 47 Tuc and other GCs, allowing to extend this scientific research and improve the statistics.

Appendix A

Collection of CMDs in F475W

Here I collect and present some additional photometric diagrams which were obtained for 47 Tuc, combining the available HST filters F475W, F606W, F814W, F110W, F140W and F160W.

Analogously to the procedure applied to the whole thesis, also these ones are explored within the magnitude range of interest, given by stars below the MS knee, focusing on M-dwarfs, eventually getting closer to the H-burning limit.

Beside the fact that they are fascinating, presenting each one a peculiar distribution of the analyzed stars, it would be interesting to investigate them further, and produce other original CMDs that exploit unusual color combinations.

Indeed, it could be studied a color combination which maximizes the separation into distinct stellar populations even more.

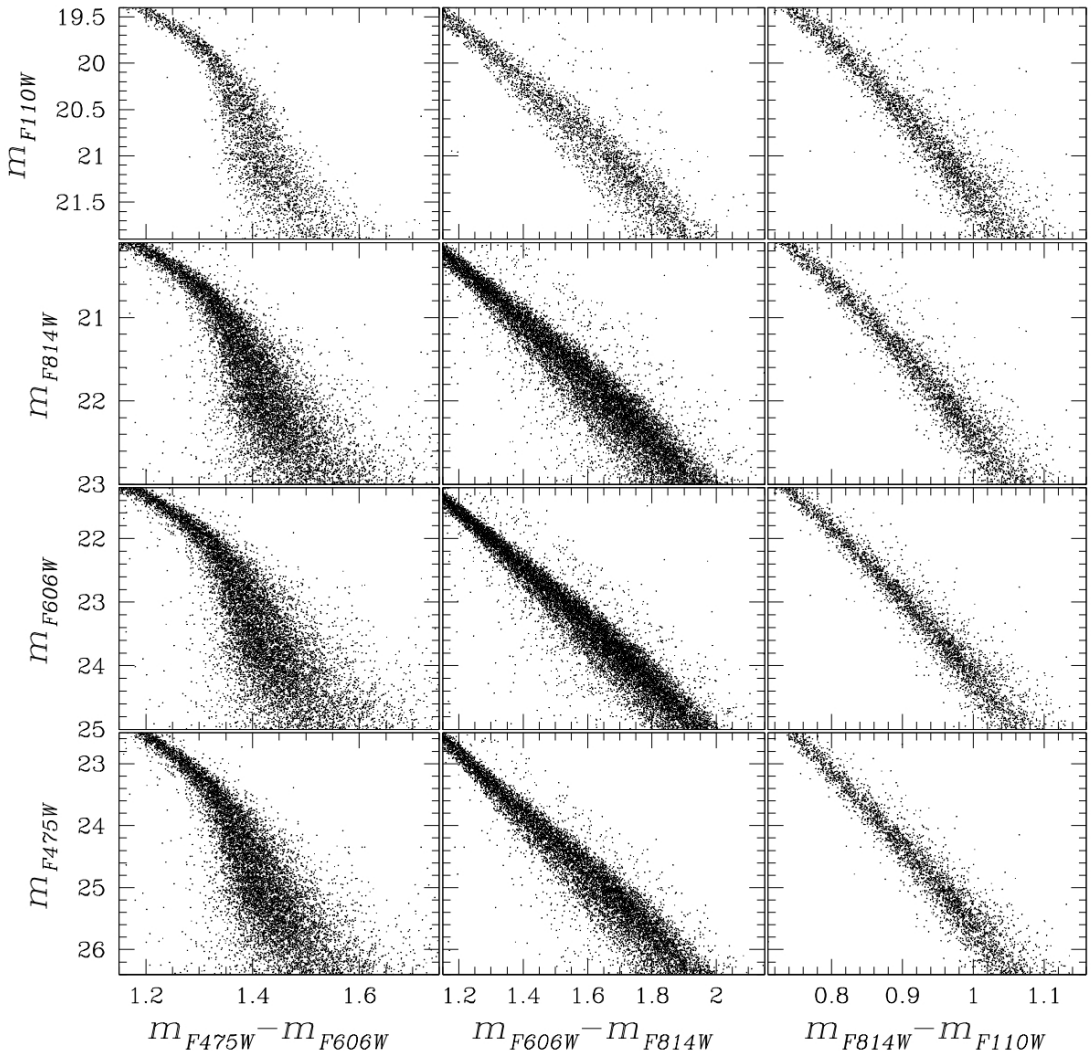

Figure A.1: CMDs of 47 Tuc in the filters F475W, F606W, F814W and F110W. It is shown the distribution of the VLM stars without a distinction into the different MPs. However, the figure allows to compare the broadening produced by these color combinations.

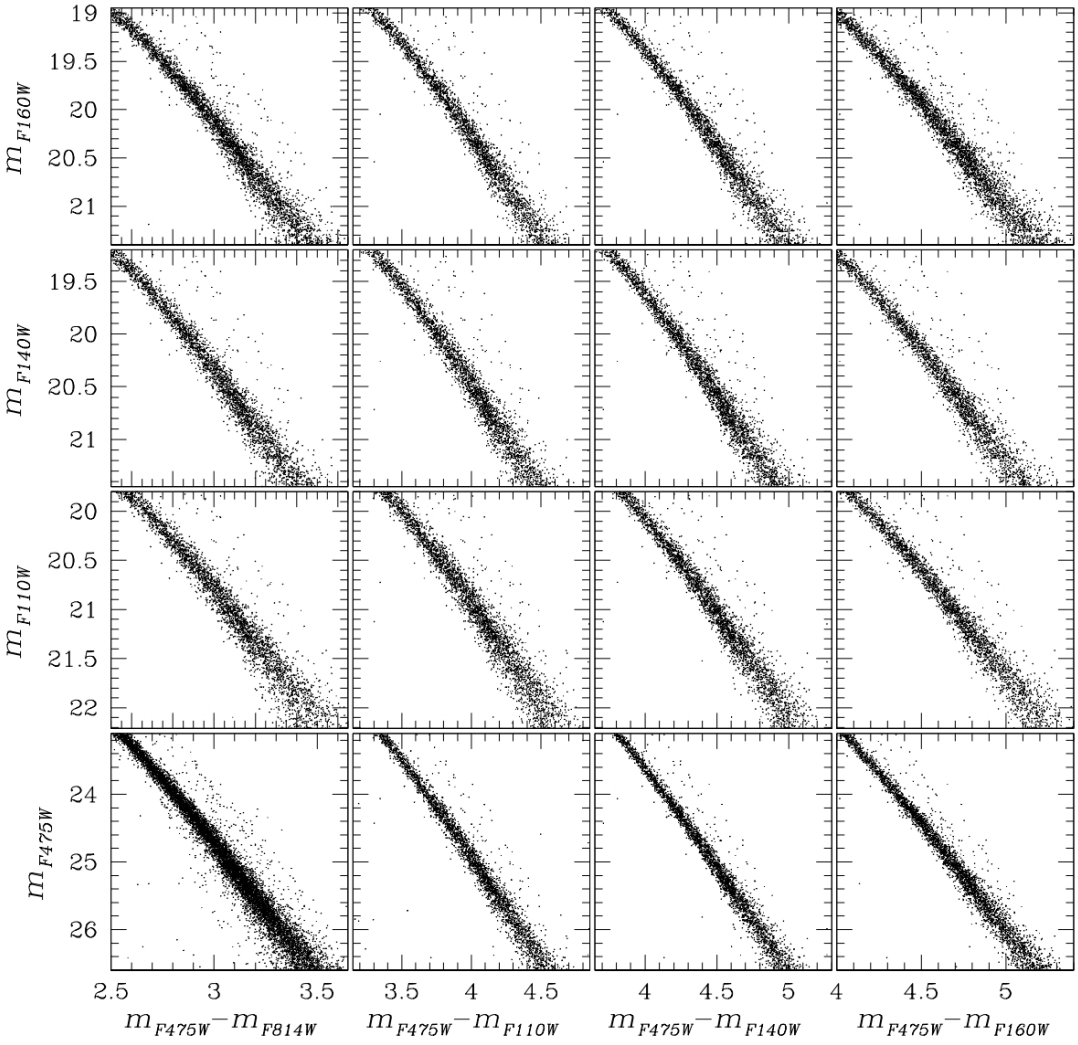

Figure A.2: Similarly to the previous Figure A.1, but here are shown CMDs in which the color always includes the filter F475W.

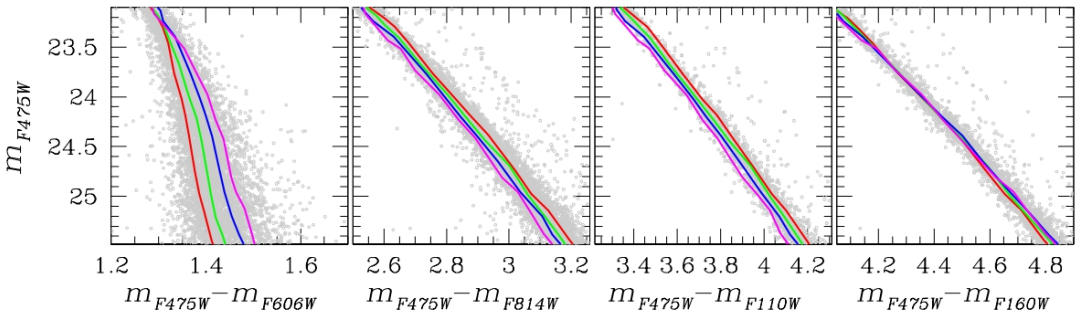

Figure A.3: These CMDs analyze much deeper some of the previous diagrams for 47 Tuc. All the color combinations are considered against the same magnitude, i.e. $m_{\rm F475W}$. On top of the distribution of the VLM stars (in gray) are overimposed the four fiducial lines of the populations selected in Chapter 4. Also in this case, the associated colors are: red to 1P, green to 2Pa, blue to 2Pb, and magenta to 2Pc. This way it is resolved the difference in each population distribution, more in details, highlighting broader sequences (the first plot on the left) or thinner ones (the last on the right).

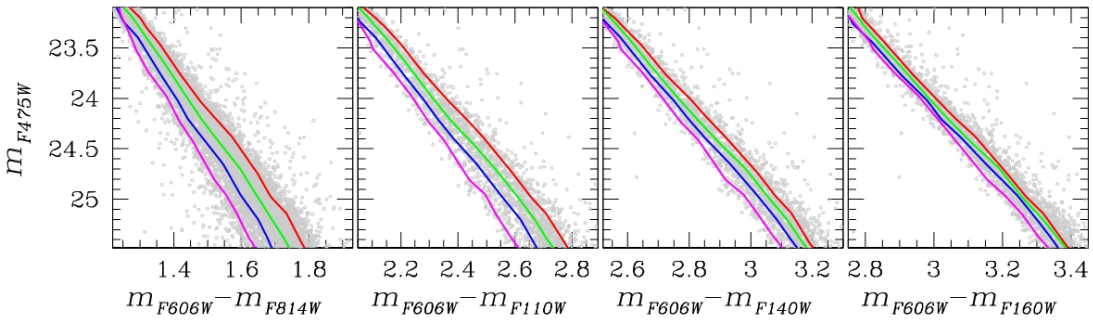

Figure A.4: Same format as in Figure A.3, for different color combinations.

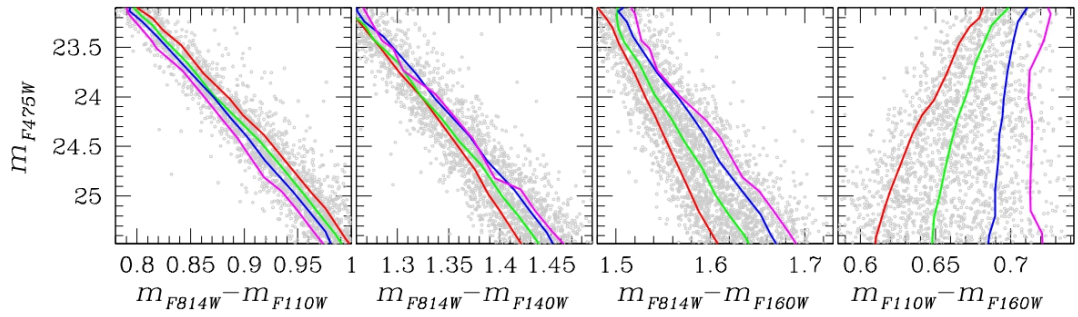

Figure A.5: Same format as in Figure A.3, for different color combinations. Noticeable is the fourth diagram on the right: due to the chosen color base it is visible a wider distribution for the MPs detected.

Bibliography

Anderson J., Bedin L., 2010, *An Empirical Pixel-Based Correction for Imperfect CTE. I. HST's Advanced Camera for Surveys*, PASP, 122, 1035

Anderson J., King I., 2000, *Toward High-Precision Astrometry with WFPC2. I. Deriving an Accurate Point-Spread Function*, PASP, 112, 1360

Anderson J., King I., 2006, *PSFs, Photometry and Astronomy for the ACS/WFC*, Instrument Science Report ACS 2006-01, p. 34

Anderson J., et al., 2008, *The ACS Survey of Globular Clusters. V. Generating a Comprehensive Star Catalog for each Cluster*, ApJ, 135

Anderson J., Piotto G., King I., Bedin L., Guhathakurta P., 2009, *Mixed Populations in Globular Clusters: Et Tu, 47 Tuc?*, ApJ, 697, L58

Bastian N., Lardo C., 2018, *Multiple Stellar Populations in Globular Clusters*, ARA&A, 56, 83

Bastian N., Lamers H., De Mink S., Longmore S., Goodwin S., Gieles M., 2013, *Early disc accretion as the origin of abundance anomalies in globular clusters*, MNRAS, 436, 2398

Baumgardt H., Hilker M., 2018, *A catalogue of masses, structural parameters, and velocity dispersion profiles of 112 Milky Way globular clusters*, MNRAS, 478, 1520

Bedin L., Salaris M., Piotto G., Cassisi S., Milone A., Anderson J., King I., 2008, *The Puzzling White Dwarf Cooling Sequence in NGC 6791: A Simple Solution*, ApJL, 679, L29

Bell R., Hesser J., Cannon R., 1983, *Spectroscopic analysis of dwarf and subgiant stars in 47 Tucanae*, ApJ, 269, 580

Bellini A., Piotto G., Bedin L., King I., Anderson J., Milone A., Momany Y., 2009, *Radial distribution of the multiple stellar populations in ω Centauri*, A&A, 507, 1393

Bellini A., Milone A., Anderson J., Marino A., Piotto G., van der Marel R., Bedin L., King I., 2017, *The State-of-the-art HST Astro-photometric Analysis of the Core of ω Centauri. III. The Main Sequence's Multiple Populations Galore*, A&AS, 844

Bellini A., et al., 2018, *The HST large 47 programme on ω Centauri. II. Internal Kinematics*, ApJ, 853, 19

Bondi H., Hoyle F., 1944, *On the Mechanism of Accretion by Stars*, MNRAS, 104, 273

Bragaglia A., Sneden C., Carretta E., Gratton R., Lucatello S., Bernath P., Brooke J., Ram R., 2014, *Searching for chemical signatures of multiple stellar populations in the old, massive open cluster NGC 6791*, ApJ, 796

Briley M., Hesser J., Bell R., 1991, *C and N Abundances among 47 Tucanae Main-Sequence Stars*, ApJ, 373, 482

Brown J., Wallerstein G., Oke J., 1990, *High-Resolution CCD Spectra of Stars in Globular Clusters V: Carbon, Nitrogen, and Oxygen Abundances in Stars in 47 Tuc, M4, and M22*, AJ, 100, 1561

Cadelano M., et al., 2023, *JWST uncovers helium and water abundance variations in the bulge globular cluster NGC 6440*, A&A, 679, 7

Carlos M., et al., 2023, *The chemical composition of multiple stellar populations in the globular cluster NGC 2808*, MNRAS, 519, 1695

Carretta E., 2015, *Five Groups of Red Giants with Distinct Chemical Composition in the Globular Cluster NGC 2808*, ApJ, 810, 17

Carretta E., Bragaglia A., Gratton R., Lucatello S., 2009, *Na-O anticorrelation and HB. VIII. Proton-capture elements and metallicities in 17 globular clusters from UVES spectra*, A&A, 505, 139

Carretta E., Gratton R., Bragaglia A., D'Orazi V., Lucatello S., 2013a, *An aluminum tool for multiple stellar generations in the globular clusters 47 Tucanae and M4*, A&A, 550, 15

Carretta E., Bragaglia A., Gratton R., Lucatello S., D'Orazi V., et al., 2013b, *NGC 362: another globular cluster with a split red giant branch*, A&A, 557, 15

Carretta E., Bragaglia A., Lucatello S., Gratton R., D'Orazi V., Sollima A., 2018, *Aluminium abundances in five discrete stellar populations of the globular cluster NGC 2808*, A&A, 615, 13

Cordero M., Pilachowski C., Johnson C., McDonald I., Zijlstra A., Simmerer J., 2014, *Detailed Abundances for a Large Sample of Giant Stars in the Globular Cluster 47 Tucanae (NGC 104)*, ApJ, 780, 14

Cordoni G., Milone A., Mastrobuono-Battisti A., Marino A., Lagioia E., Tailo M., Baumgardt H., Hilker M., 2020, *Three-component Kinematics of Multiple Stellar Populations in Globular Clusters with Gaia and VLT*, ApJ, 889, 18

Cottrell P., Da Costa G., 1981, *Correlated cyanogen and sodium anomalies in the globular clusters 47 TUC and NGC 6752*, ApJ, 245, L79

D'Antona F., Gratton R., Chieffi A., 1983, *CNO self-pollution in globular clusters; a model and its possible observational tests*, MemSAIt, 54, 173

D'Antona F., Ventura P., Decressin T., Vesperini E., D'Ercole A., 2014, *Pre-main-sequence accretion and the formation of multiple populations in globular clusters*, MNRAS, 443, 3302

D'Orazi V., Gratton R., Lucatello S., Carretta E., Bragaglia A., Marino A., 2010, *Ba Stars and Other Binaries in First and Second Generation Stars in Globular Clusters*, ApJL, 719, L213

D'Orazi V., Angelou G., Gratton R., Lattanzio J., Bragaglia A., Carretta E., Lucatello S., Momany Y., 2014, *Lithium Abundances in Globular Cluster Giants: NGC 6218 (M12) and NGC 5904 (M5)*, ApJ, 791, 13

Dalessandro E., Lapenna E., Mucciarelli A., Origlia L., Ferraro F., Lanzoni B., 2016, *Multiple Populations in the Old and Massive Small Magellanic Cloud Globular Cluster NGC 121*, ApJ, 829

Dalessandro E., et al., 2018, *The Unexpected Kinematics of Multiple Populations in NGC 6362: Do Binaries Play a Role?*, ApJ, 864, 9

De Mink S., Pols O., Langer N., Izzard R., 2009, *Massive binaries as the source of abundance anomalies in globular clusters*, A&A, 507, L1

Decressin T., Meynet G., Charbonnel C., Prantzos N., Ekström S., 2007a, *Fast rotating massive stars and the origin of the abundance patterns in galactic globular clusters*, A&A, 464, 1029

Decressin T., Charbonnel C., Meynet G., 2007b, *Origin of the abundance patterns in Galactic globular clusters: constraints on dynamical and chemical properties of globular clusters*, A&A, 475, 859

Denissenkov P., Hartwick F., 2014, *Supermassive stars as a source of abundance anomalies of proton-capture elements in globular clusters*, MNRAS, 437, L21

Di Criscienzo M., Ventura P., D'Antona F., Milone A., Piotto G., 2010, *The helium spread in the globular cluster 47 Tuc*, MNRAS, 408, 999

Dickens R., Bell R., Gustafsson B., 1979, *Carbon and nitrogen abundances in red giant stars in the globular cluster 47 Tucanae*, ApJ, 232, 428

Dobrovolskas V., Kucinskas A., Bonifacio P., Korotin S., Steffen M., Sbordone L., et al., 2014, *Abundances of lithium, oxygen, and sodium in the turn-off stars of Galactic globular cluster 47 Tucanae*, A&A, 565, 24

Dondoglio E., Milone A., Lagioia E., Marino A., Tailo M., Cordoni G., Jang S., Carlos M., 2021, *Multiple Stellar Populations along the Red Horizontal Branch and Red Clump of Globular Clusters*, ApJ, 906

Dondoglio E., et al., 2022, *Survey of Multiple Populations in Globular Clusters among Very-low-mass Stars*, ApJ, 927, 18

Dotter A., et al., 2010, *The ACS Survey of Galactic Globular Clusters. IX. Horizontal Branch Morphology and the Second Parameter Phenomenon*, ApJ, 708, 698

D'Antona F., Vesperini E., D'Ercole A., Ventura P., Milone A., Marino A., Tailo M., 2016, *A single model for the variety of multiple-population formation(s) in globular clusters: a temporal sequence*, MNRAS, 458, 2122

D'Ercole A., Vesperini E., D'Antona F., McMillan S., Recchi S., 2008, *Formation and dynamical evolution of multiple stellar generations in globular clusters*, MNRAS, 391, 825

D'Ercole A., D'Antona F., Ventura P., Vesperini E., McMillan S., 2010, *Abundance patterns of multiple populations in globular clusters: a chemical evolution model based on yields from AGB ejecta*, MNRAS, 407, 854

Forbes D., Bridges T., 2010, *Accreted versus in situ Milky Way globular clusters*, MNRAS, 404, 1203

Fregeau J., Gurkan M., Joshi K., Rasio F., 2003, *Monte Carlo Simulations of Globular Cluster Evolution. III. Primordial Binary Interactions*, ApJ, 593, 772

Fregeau J., Ivanova N., Rasio F., 2009, *Evolution of the Binary Fraction in Dense Stellar Systems*, ApJ, 707, 1533

Gieles M., et al., 2018, *Concurrent formation of supermassive stars and globular clusters: implications for early self-enrichment*, MNRAS, 478, 2461

Gratton R., Sneden C., Carretta E., 2004, *Abundance Variations Within Globular Clusters*, ARA&A, 42, 385

Gratton R., Bragaglia A., Carretta E., D'Orazi V., Lucatello S., Sollima A., 2019, *What is a globular cluster? An observational perspective*, A&AR, 27, 136

Heggie D., 1975, *Binary Evolution in STellar Dynamics*, MNRAS, 173, 729

Heggie D., Hut P., 2003, *The Gravitational Million-Body Problem: A Multidisciplinary Approach to Star Cluster Dynamics*. Cambridge University Press

Hong J., Vesperini E., Sollima A., McMillan S., D'Antona F., D'Ercole A., 2015, *Evolution of binary stars in multiple-population globular clusters*, MNRAS, 449, 629

Hong J., Vesperini E., Sollima A., McMillan S., D'Antona F., D'Ercole A., 2016, *Evolution of binary stars in multiple-population globular clusters. II. Compact binaries*, MNRAS, 457, 4507

Hong J., Patel S., Vesperini E., Webb J., Dalessandro E., 2019, *Spatial mixing of biary stars in multiple-population globular clusters*, MNRAS, 483, 2592

Ivanova N., Belczynski K., Fregeau J., Rasio F., 2005, *The evolution of binary fractions in globular clusters*, MNRAS, 358, 572

Jang S., et al., 2022, *Chromosome maps of globular clusters from wide-field ground-based photometry*, MNRAS, 517, 5687

Kraft R. P., 1994, *Abundance Differences among Globular Cluster Giants: Primordial vs. Evolutionary Scenarios*, PASP, 106

Krause M., Charbonnel C., Decressin T., Meynet G., Prantzos N., 2013, *Superbubble dynamics in globular cluster infancy. II. Consequences for secondary star formation in the context of self-enrichment via fast-rotating massive stars*, A&A, 552, 14

Kroupa P., 1995a, *The dynamical properties of stellar systems in the Galactic disc*, MNRAS, 277, 1507

Kroupa P., 1995b, *Star cluster evolution, dynamical age estimation and the kinematica signature of star formation*, MNRAS, 277, 1522

Kızıltan B., Baumgardt H., Loeb A., 2017, *An intermediate-mass black hole in the center of the globular cluster 47 Tucanae*, Nature, 542, 203

Lagioia E., Milone A., Marino A., Dotter A., 2019, *Helium Variation in Four Small Magellanic Cloud Globular Clusters*, ApJ, 871

Lagioia E., et al., 2021, *Multiple Stellar Populations in Asymptotic Giant Branch Stars of Galactic Globular Clusters*, ApJ, 910

Larsen S., Brodie J., Grundahl F., Strader J., 2014, *Nitrogen Abundances and Multiple Stellar Populations in the Globular Clusters of the Fornax dSph*, ApJ, 797

Lee J., 2019, *Multiple Stellar Populations of Globular Clusters from Homogeneous Ca-CN Photometry. IV. Toward Precision Populational Tagging*, ApJ, 872, 8

Lee J., 2022, *Multiple Stellar Populations of Globular Clusters from Homogeneous Ca-CN-CH-NH Photometry. VII. Metal-poor Populations in 47 Tucanae (NGC 104)*, ApJS, 263

Legnardi M., et al., 2022, *Constraining the original composition of the gas forming first-generation stars in globular clusters*, MNRAS, 513, 735

Lucatello S., Sollima A., Gratton R., Vesperini E., D'Orazi V., Carretta E., Bragaglia A., 2015, *The incidence of binaries in globular cluster stellar populations*, A&A, 584, 8

Marino A., Villanova S., Piotto G., Milone A., Momany Y., Bedin L., Medling A., 2008, *Spectroscopic and photometric evidence of two stellar populations in the Galactic globular cluster NGC 6121 (M 4)*, ApJ, 490, 625

Marino A., et al., 2016, *Chemical abundances in the multiple sub-giant branch of 47 Tucanae: insights on its faint sub-giant branch component*, MNRAS, 459, 610

Marino A., et al., 2018, *Metallicity Variations in the Type II Globular Cluster NGC 6934*, ApJ, 859

Marino A., et al., 2019, *The Hubble Space Telescope UV Legacy Survey of Galactic Globular Clusters. XIX. A chemical tagging of the multiple stellar populations over the chromosome maps*, MNRAS, 487, 3815

Marino A., et al., 2024, *A JWST project on 47 Tucanae. Overview, photometry and early spectroscopic results of M dwarfs, and observation of brown dwarfs*, Submitted to ApJ

Marks M., Kroupa P., Oh S., 2011, *An analytical description of the evolution of binary orbital-parameter distributions in N-body computations of star clusters*, MNRAS, 417, 1684

Mayor M., Duquennoy A., Halbwachs J.-L., Mermilliod J.-C., 1992, *CORAVEL Surveys to Study Binaries of Different Masses and Ages*

Milone A., Marino A., 2022, *Multiple Populations in Star Clusters*, Universe, 8

Milone A., Bedin L., Piotto G., Anderson J., 2009, *Multiple stellar populations in Magellanic Cloud clusters. I. An ordinary feature for intermediate age globulars in the LMC?*, A&A, 497, 755

Milone A., et al., 2010, *Multiple Stellar Populations in the Galactic Globular Cluster NGC 6752*, ApJ, 709, 1183

Milone A., Piotto G., Bedin L., Cassisi S., Anderson J., Marino A., Pietrinferni A., Aparicio A., 2012a, *Luminosity and mass functions of the three main sequences of the globular cluster NGC 2808*, A&A

Milone A., et al., 2012b, *The ACS survey of Galactic globular clusters. XII. Photometric binaries along the main sequence*, A&A, 540, 41

Milone A., et al., 2012c, *Multiple Stellar Populations in 47 Tucanae*, ApJ, 744

Milone A., Marino A., Piotto G., Bedin L., Anderson J., Aparicio A., et al., 2012d, *A Double Main Sequence in the Globular Cluster NGC 6397*, ApJ, 745

Milone A. P., et al., 2012e, *The Infrared Eye of the Wide-Field Camera 3 on the Hubble Space Telescope Reveals Multiple Main Sequences of Very Low Mass Stars in NGC 2808*, ApJ, 754

Milone A., et al., 2013, *A WFC3/HST View of the Three Stellar Populations in the Globular Cluster NGC 6752*, ApJ, 767

Milone A., et al., 2014, *The M4 Core Project with HST. II. Multiple stellar populations at the bottom of the main sequence*, MNRAS, 439, 1588

Milone A., et al., 2015, *The Hubble Space Telescope UV Legacy Survey of galactic globular clusters-II. The seven stellar populations of NGC 7089 (M2)*, MNRAS, 447, 927

Milone A., et al., 2017a, *The Hubble Space Telescope UV Legacy Survey of Galactic globular clusters. IX. The Atlas of multiple stellar populations*, MNRAS, 464, 3636

Milone A., et al., 2017b, *The HST large programme on ω Centauri-I. Multiple stellar populations at the bottom of the main sequence probed in NIR-Optical*, MNRAS, 496, 800

Milone A., Marino A., Mastrobuono-Battisti A., Lagioia E., 2018a, *Gaia unveils the kinematics of multiple stellar populations in 47 Tucanae*, MNRAS, 479, 5005

Milone A., et al., 2018b, *The Hubble Space Telescope UV legacy survey of galactic globular clusters. XVI. The helium abundance of multiple populations*, MNRAS, 481, 5098

Milone A., et al., 2019, *The HST Large Programme on NGC 6752. II. Multiple populations at the bottom of the main sequence probed in NIR*, MNRAS, 484, 4046

Milone A., et al., 2020a, *Multiple populations in globular clusters and their parent galaxies*, MNRAS, 491, 515

Milone A., et al., 2020b, *The Hubble Space Telescope UV Legacy Survey of Galactic globular clusters. XXI. Binaries among multiple stellar populations*, MNRAS, 492, 5457

Milone A., et al., 2023a, *Multiple Stellar Populations in Globular Clusters with JWST: a NIRCam view of 47 Tucanae*, MNRAS

Milone A. P., et al., 2023b, *Hubble Space Telescope survey of Magellanic Cloud star clusters. Photometry and astrometry of 113 clusters and early results*, A&A, 672, 34

Mucciarelli A., Origlia L., Ferraro F., Pancino E., 2009, *Looking Outside the Galaxy: The Discovery of Chemical Anomalies in Three Old Large Magellanic Cloud Clusters*, ApJL, 695, L134

Nardiello D., Milone A., Piotto G., Marino A., Bellini A., Cassisi S., 2015, *Observing multiple stellar populations with VLT/FORS2. Main sequence photometry in outer regions of NGC 6752, NGC 6397, and NGC 6121 (M4)*, A&A, 573, 16

Nardiello D., Piotto G., Milone A., Rich R., Cassisi S., Bedin L., Bellini A., Renzini A., 2019, *Hubble Space Telescope analysis of stellar populations within the globular cluster G1 (Mayall II) in M 31*, MNRAS, 485, 3076

Renzini A., 2013, *Rethinking globular clusters formation*, MemSAIt, 84, 162

Renzini A., 2017, *Finding forming globular clusters at high redshifts*, MNRAS, 469, L63

Renzini A., Buzzoni A., 1986, *Global properties of stellar populations and the spectral evolution of galaxies*, Spectral Evolution of Galaxies, 122, 195

Renzini A., et al., 2015, *The Hubble Space Telescope UV Legacy Survey of Galactic Globular Clusters. V. Constraints on formation scenarios*, MNRAS, 454, 4197

Richer H., et al., 2008, *Deep Advanced Camera for Surveys Imaging in the Globular Cluster NGC 6397: the cluster Color-Magnitude Diagram and Luminosity Function*, A&AS, 135, 2141

Richer H., Heyl J., Anderson J., Kalirai J., Shara M., Dotter A., Fahlman G., Rich R., 2013, *A Dynamical Signature of Multiple Stellar Populations in 47 Tucanae*, ApJL, 771, 5

Salaris M., Cassisi S., 2014, *Lithium and oxygen in globular cluster dwarfs and the early disc accretion scenario*, A&A, 566, 8

Salaris M., Held E., Ortolani S., Gullieuszik M., Momany Y., 2007, *Deep near-infrared photometry of the globular cluster 47 Tucanae. Reconciling theory and observations*, A&A, 476, 243

Silverman B., 1986, *Density estimation for statistics and data analysis*. Monographs on Statistics and Applied Probability

Sollima A., 2008, *The evolution of the binary population in globular clusters: a full analytical computatioin*, MNRAS, 388, 307

Sollima A., Beccari G., F.R. F., Fusi Pecci F., A. S., 2007a, *The fraction of binary systems in the core of 13 low-density Galactic globular clusters*, MNRAS, 380, 781

Sollima A., Ferraro F., Bellazzini M., Origlia L., Straniero O., Pancino E., 2007b, *Deep FORS1 Observations of the Double Main Sequence of ω Centauri*, ApJ, 654, 915

Sollima A., Carballo-Bello J., Beccari G., Ferraro F., Fusi Pecci F., Lanzoni B., 2009, *The fraction of binary systems in the core of five Galactic open clusters*, MNRAS, 401, 577

Tailo M., et al., 2020, *Mass-loss along the red giant branch in 46 globular clusters and their multiple populations*, MNRAS, 498, 5745

Ventura P., D'Antona F., Mazzitelli I., Gratton R., 2001, *Predictions for Self-Pollution in Globular Cluster Stars*, ApJ, 550, L65

Ventura P., Di Criscienzo M., Carino R., D'Antona F., 2013, *Yields of AGB and SAGB models with chemistry of low and high-metallicity globular clusters*, MNRAS, 431, 3642

Vesperini E., McMillan S., D'Antona F., D'Ercole A., 2011, *Binary star disruption in globular clusters with multiple stellar populations.*, MNRAS, 416, 355

Villanova S., Geisler D., Carraro G., Moni Bidin C.; Muñoz C., 2013, *Ruprecht 106: The First Single Population Globular Cluster?*, ApJ, 778

Yan L., Reid I., 1996, *Discovery of six short-period eclipsing binaries in the globular cluster M5*, MNRAS, 279, 751

Zennaro M., Milone A., Marino A., Cordoni G., Lagioia E., Tailo M., 2019, *Four stellar populations and extreme helium variation in the massive outer-halo globular cluster NGC 2419*, MNRAS, 487, 3239

Ziliotto T., et al., 2023, *Multiple Stellar Populations in Metal-poor Globular Clusters with JWST: A NIRCam View of M92*, ApJ, 953, 12